Effects of the lattice distortion on the magnetic order in rare-earth nickelates

by

Stepan Olegovich Fomichev

B.Sc., The University of Toronto, 2012

A THESIS SUBMITTED IN PARTIAL FULFILLMENT OF
THE REQUIREMENTS FOR THE DEGREE OF

MASTER OF SCIENCE

in

The Faculty of Graduate and Postdoctoral Studies

(Physics)

THE UNIVERSITY OF BRITISH COLUMBIA

(Vancouver)

August 2019

The following individuals certify that they have read, and recommend to the Faculty of Graduate and Postdoctoral Studies for acceptance, the thesis entitled:

Effects of the lattice distortion on the magnetic order in rare-earth nickelates

submitted by **Stepan Olegovich Fomichev** in partial fulfillment of the requirements for the degree of **Master of Science** in Physics.

Examining Committee:

Mona Berciu, Physics and Astronomy
Supervisor

George Sawatzky, Physics and Astronomy
Examining Committee Member

Abstract

The low-temperature magnetic order in the rare-earth nickelates is a subject of vigorous debate in the literature. Recent work emphasized the primary role of the electron-phonon coupling for the metal-insulator transition in the nickelates, and suggested that lattice distortions are the driver of the transition, leading to the observed charge order. However, to our knowledge there has been little work on the impact of lattice distortions on the magnetic order, in particular whether distortions favour some orders over others. In this thesis, we study the magnetic order in the nickelates at zero temperature, and investigate whether the breathing-mode lattice distortions select a preferred ground state. An effective two-band Hubbard model for the nickelates is constructed and coupled to the lattice distortions with an on-site Holstein-like term. The distortions are treated semiclassically. Using the Hartree-Fock approximation, we obtain the magnetic phase diagram, then turn on the coupling to the lattice to observe its impact on the various phases. Our model reproduces the earlier work showing the stronger charge disproportionation and insulating behaviour in the phase space due to increased coupling to the lattice. Furthermore, we find numerous 4-site magnetic orders that are self-consistent within the model, including all of the main suggestions in the literature (states such as $\uparrow\uparrow\downarrow\downarrow$, $\uparrow\rightarrow\downarrow\leftarrow$ and $\Uparrow\ 0\ \Downarrow\ 0$). However, in this model a magnetic order can only couple to the lattice distortions if there is nonzero charge disproportionation. As a result, we find that coupling to the lattice distortions broadly favours the $\Uparrow\ 0\ \Downarrow\ 0$ order in large sectors of the parameter space. Finally, we considered the impact of longer range hopping on the magnetic order: we find that the shape of the density of states, rather than overall bandwidth, primarily determines the magnetic ground state. A van Hove singularity arises even for small 2nd-nearest hopping amplitudes, which results in robust ferromagnetism across most of the phase diagram in a Stoner-like fashion. On the contrary, even small 4th-nearest amplitudes decrease the Fermi level density of states, resulting in ballooning of the metallic phase despite a barely renormalized bandwidth.

Lay Summary

While the study of magnetism began as a hobby for philosophers, it has since led to deep insights about our physical world. Aside from the obvious utility of fridge magnets, understanding the atomic origin of magnetism has given humanity many useful tools: MRI machines, loudspeakers, hard drives. Magnetism originates with an electronic property – spin: electrons are essentially tiny bar magnets. In most magnets, electrons align in one direction, producing strong magnetism on the macroscopic scale. But rare-earth nickelates – at low temperature – become a peculiar kind of a magnet. Instead of aligning, the electrons exhibit an unknown pattern repeating every four lattice sites, potentially $\uparrow\uparrow\downarrow\downarrow$ or $\uparrow\rightarrow\downarrow\leftarrow$. In this thesis, we construct a quantum-mechanical model for the nickelates to study their magnetism. Using the magnetic pattern of this material to encode bits of information is just one potential technological byproduct that could become available as our understanding of the material grows.

Preface

- I wrote this thesis in its entirety. The literature review and summary in Chapter 1 arise from my own reading and analysis. The model for the nickelates suggested in Chapter 2 is due to my supervisor for the project, Mona Berciu, and our collaborator Giniyat Khaliullin from the Max Planck Institute at Stuttgart. The analytical calculations pertaining to the model, including the Hartree-Fock calculations, in Chapter 3 have been carried out originally by Mona Berciu and subsequently repeated by me. I envisioned and constructed the numerical implementation of the Hartree-Fock equations as described in Chapter 4, including all of the additional techniques beyond the textbook approach, such as Pulay mixing. All the results in Chapter 5 have been obtained by me using the program described in Chapter 4. Finally, the analysis in Chapters 5 and 6 was conducted by me, in consultation with Mona Berciu.

- A version of the work discussed in Chapters 2, 3, 4, 5 is to be submitted for publication under the authorship of *Stepan Fomichev, Giniyat Khaliullin*, and *Mona Berciu*, with the manuscript presently in preparation.

- UBC Research Ethics Board approval was not required for this work.

Table of Contents

List of Figures

Acknowledgments

Conducting research and writing a thesis has been a massive undertaking, and I am extremely grateful to Mona Berciu for guiding me through it. From suggesting the problem (together with Giniyat Khaliullin), to slowly showing me the ropes of being a theoretical physicist, and to supporting me at conferences, seminars, and group meetings, Mona has been exceptionally kind, attentive, and encouraging.

And the tightly-knit, warm and welcoming environment she nurtured within her group was indispensable to all of our academic pursuits, and to our sense of well-being. I am really grateful for all the discussions, hikes, ice-cream breaks, and escape room pursuits that helped me to get to know better so many wonderful physicists, including Nathan Cheng, Mirko Möller, and John Sous. Without their peer-to-peer guidance, sharp questions and helpful answers, I would be hard pressed to learn as much as I did: and without the coffee breaks and the jokes, it would have been hard to keep going.

I would especially like to thank my long-time friend Kyle Wamer, who has valiantly endured two years of sitting across from me and debating the very foundations of condensed matter, by asking some silly questions ("so, what are phonons, anyway?"); and who has single-handedly introduced me to Vancouver – the city, the people, and the mountains.

There are many wonderful people at UBC that have made this an unforgettable journey, both in and outside the classroom. I am thankful to Ali, Jordan, Christian, Connor, Adam, Tarun, Victor, Ian and Khoi, for the conferences, hikes, classes, ski hills, exams, lake-side cabins, boiler rooms, and coffee shops we enjoyed together.

Lastly, I would like to thank Evgenia, for her loving support and cheerful company, which made every moment of this journey exciting and memorable.

To my mother, without whose selfless sacrifices I would never be where I am today. And to my father, whose endless patience for my endless questions nurtured my love of physics.

Chapter 1

Introduction: Experiments and Calculations on the Nickelates

> The ultimate court of appeal is observation and experiment... not authority.
>
> Thomas Huxley (1875)

Rare-earth nickelates (chemical formula $R\mathrm{NiO}_3$, with R any rare-earth element from La to Lu) are a fascinating perovskite transition-metal oxide [10] material series that have not only generated much excitement in the condensed matter community as a matter of fundamental interest [3, 4], but are also now inspiring more and more potential applications, specifically in the memory domain [11–13]. Obtained for the first time in 1971 by Demazeau *et al.* [14], they were largely ignored until the general surge of interest in perovskite materials in the 90s, generated by the discovery in one of them – the cuprates – of high-temperature superconductivity in the late 80s [15].

In terms of basic science, the nickelates exhibit a variety of phase transitions and emergent orders. All nickelates except LaNiO_3 undergo – in fact are considered the prime examples of – a sharp metal-to-insulator (MIT) transition [16] (see Fig. 1.1 for a phase diagram), which is generally understood to be a consequence of charge order (although the exact mechanism is still disputed [17–22]). The transition is concurrent with a breathing-mode, rock-salt pattern lattice distortion [23], as shown in Fig. 1.2. In addition, for all nickelates except LaNiO_3[1], at still lower temperatures (and for Pr and Nd, at the same temperature as the MIT) there is an additional, *magnetic* phase transition, resulting in an as-yet poorly-understood magnetic order, with various competing proposals [4, 25–28]. While the phases themselves

[1] although this has recently been challenged [24].

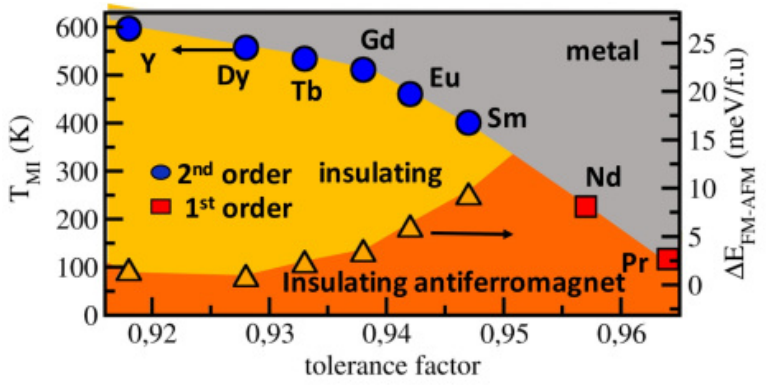

Figure 1.1: A temperature vs. type of rare-earth ion phase diagram of the rare-earth nickelates, adapted from Ref. [1].

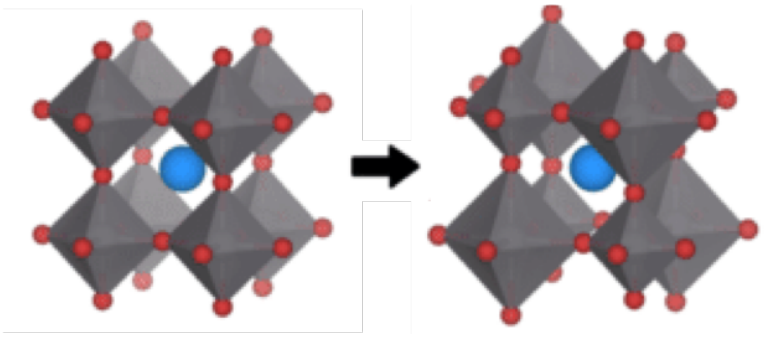

Figure 1.2: A graphic of the rocksalt breathing-mode distortion in the rare-earth nickelates. Adapted from Ref. [2].

are reasonably well-understood and characterized (with the exception of the low-temperature magnetism, which is largely due to the difficulty of synthesizing large enough single crystal samples), the precise mechanisms of the charge and magnetic phase transitions are not yet entirely clear. Moreover, almost all of these transitions can be tuned with the type of rare-earth ion (as in Fig. 1.1), pressure [29], in heterostructures [30], and even swapping out the oxygen for its isotopes [31].

One of the thorniest questions in the field in recent years has been the nature and origin of the magnetic order that obtains in this material series at low temperatures. Specifically, while neutron diffraction measurements have firmly established the ordering wavevector of the magnetic phase as $\mathbf{Q}_m = \frac{2\pi}{a}[\frac{1}{4}, \frac{1}{4}, \frac{1}{4}]_{\text{pseudocubic}}$[2], the community is still debating the origin and precise alignment of the local magnetic moments. Some of the magnetic orders potentially consistent with the above ordering wavevector include $\Uparrow 0 \Downarrow 0$ [25], as well as $\Uparrow\uparrow\Downarrow\downarrow$ [26] and even the non-collinear option $\Uparrow\rightarrow\Downarrow\leftarrow$ (throughout this thesis we use fat arrows to indicate larger spin magnitudes). In light of recent work demonstrating that the lattice breathing-mode distortion helps stabilize charge order in the nickelates [32], it seemed reasonable to suggest that the lattice distortion could also preferentially favour one or the other kind of magnetic orders suggested in the literature. In this thesis, we address the magnetic order question by constructing an effective two-band Hubbard Hamiltonian for the nickelates, and coupling it through an on-site interaction to the lattice distortion, which we treat semiclassically. We then search for the magnetic ground state in the Hartree-Fock approximation, and consider how the presence of coupling to the lattice distortion affects the magnetic phases that arise.

This thesis is structured as follows: in the rest of this chapter we begin by describing, at the appropriate level of detail, the phenomenology of this Ni material series, including structural, charge and magnetic properties – as gleaned from experiment. In Chapter 2, we construct in detail the microscopic model used for the nickelates in our study. In Chapters 3 and 4, we apply and numerically implement the Hartree-Fock approximation for the model. In Chapter 5, we present our results and answer the main research questions of the thesis, as well as comment on any unexpected discoveries. Our conclusions and outlook are summarized in Chapter 6.

[2] $\frac{2\pi}{a}[\frac{1}{2}, 0, \frac{1}{2}]$ in perovskite notation.

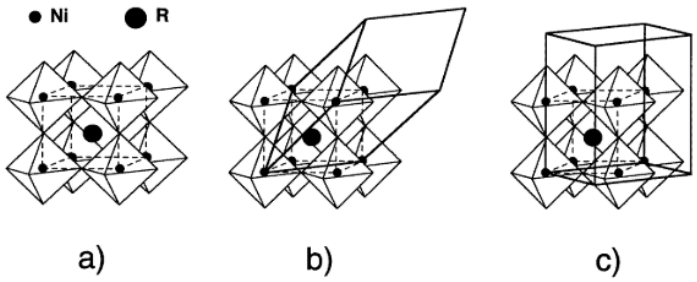

Figure 1.3: From Medarde's excellent 1997 review, Ref. [3]. (a) Ideal perovskite structure; (b) Rhombohedral distortion twists about the [111] direction for $t \sim 1$ ($R\bar{3}c$ point group symmetry class) (c) Orthorhombic distortion twists about the [110] direction – the case for most of the nickelates (dominant mode at smaller t).

1.1 Crystal structure

At room temperature, most nickelates – whether found in nature or synthesized in the laboratory – consist of the usual columns of oxygen octahedra engulfing the nickel atoms, with the rare-earth ions sitting in-between them (see Fig. 1.3a for a diagram of the crystal structure). For all the nickelates, the structure actually is strictly speaking not an ideal perovskite lattice: it has a slight deviation from perfect cubic lattice symmetry due to "twists" of the octahedra, caused by the too-*small*-to-fit rare-earth ions (many of the lattice parameters are tabulated in [33]; for more general information about the crystal structure, see [3]). In practice, these deviations – characterized by the Goldschmidt tolerance factor t [34], defined as

$$t = \frac{d_{\text{R-O}}}{\sqrt{2} d_{\text{Ni-O}}}, \tag{1.1}$$

where d are the bond lengths of R-O and Ni-O, respectively, – are rather small and often either entirely ignored [26], or incorporated phenomenologically (*e.g.* through modifying the hopping rates in a tight-binding model). The range of variation of t is fairly small – from $t = 0.932$ for $LuNiO_3$ to $t = 0.986$ for $LaNiO_3$. As an aside, sometimes also the Ni-O-Ni bond angle is used in place of the tolerance factor to characterize the distortion: it is marked in Fig. 1.4.

The most stark phase change in the nickelate phase diagram is between the high-temperature metallic phase, and the low temperature insulating

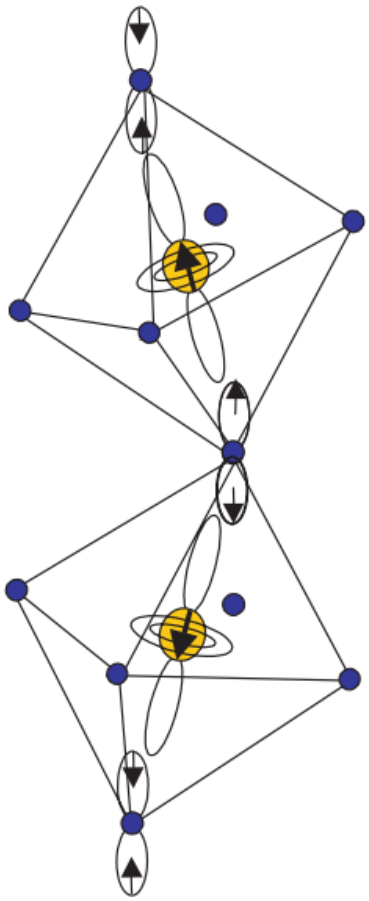

Figure 1.4: Ni-O-Ni bond angle in the rare-earth nickelates is a measure of the perosvkite distortion, equivalent to the tolerance factor. Figure from Ref. [4].

phase. (The only element in the series that stays metallic at all temperatures is the La based compound.) Before we discuss this metal-to-insulator transition (MIT), which is still at times a source of controversy in the literature, we first consider the structural changes that occur in the nickelates across that same phase boundary, as the former is widely thought to be heavily influenced, if not outright triggered, by the latter.

1.2 Structural Transition

As the temperature is lowered, all nickelates (except $LaNiO_3$) undergo a symmetry reducing lattice distortion, which changes their point group class from the orthorhombic $Pbnm$ to monoclinic $P2_1/n$ [5, 9, 35–37]. In addition, there is a slight volume reduction [23]. As was just mentioned, the structural deformations may be rather complex, combining twists and tilts about various crystal axes [3, 4, 23, 27, 38]: however, it is of prime importance to determine exactly the kind of distortion type (or symmetry class) that dominates the overall structural evolution, as different types would support qualitatively different explanations for the MIT (see Secs. 1.3,1.4). This can be accomplished through the use of symmetry-mode based decomposition analysis (in this section we follow Refs. [5, 39]; for a general review of the method in crystallography, see Ref. [40]). In short, the atomic positions in a distorted crystal, labelled $\mathbf{r}_i^{\text{dist}}$, are written in terms of the coordinates of the undistorted, high-symmetry crystal $\mathbf{r}_i^0$ and a linear combination of particular distortion modes with unit displacement vectors $\mathbf{d}_{im}$ and distortion mode amplitudes A_m

$$\mathbf{r}_i^{\text{dist}} = \mathbf{r}_i^0 + \sum_m A_m \mathbf{d}_{im}. \tag{1.2}$$

The modes $\mathbf{d}_{im}$ are defined based on symmetry considerations, which makes them independent from each other and allows for the decomposition. This approach helps process experimental data, which often comes as various Ni-O bond lengths, Ni-O-Ni angles, and other crystallographic parameters, in a transparent way and quickly identify the dominant distortion modes from change in the amplitudes A_m across a phase line. Balachandran and Rondinelli [5] have carried out a careful symmetry-mode based decomposition analysis for the nickelates: they noted that, while there is significant distortion of types R_4^+ (an out-of-phase rotation, see Fig. 1.5f), M_3^+ (an in-phase twist, see Fig. 1.5c), and X_5^+ (in-phase tilting, see Fig. 1.5h) already

present in the nickelates at high temperatures, the biggest change across the MIT phase line is in the sudden appearance from zero of the breathing-mode type distortion R_1^+ (already depicted above in Fig. 1.2). Meanwhile the various Jahn-Teller like modes (see Sec. 1.4.2 for a discussion of why they were thought to be important) are negligibly small.

Some of the earlier structural analysis [41] seemed to suggest that Jahn-Teller distortions were present, but the conclusions were drawn based on a more rudimentary technique – that of calculating the distortion parameter $\Delta_d = (1/6)\sum_{n=1,...6}[(d_n - \langle d\rangle)/\langle d\rangle^2]^2$, where $\langle d\rangle$ is the average Ni-O bond length and d_n are the various Ni-O bond lengths measured in neutron-scattering studies. Moreover, in the analysis the change of this parameter with temperature for a fixed R member of the nickelate series was never considered. Rather, the distortion parameter was calculated for the nickelate series and correlated with the transition temperatures T_{MIT}: but it is the changes across the MIT phase line that are most significant, and a cross-sectional view of the nickelate series cannot conclusively establish what distortions are relevant across it. In light of the more sophisticated treatment via eq. 1.2, it is clear that the earlier approach (a) could not easily differentiate between the various contributions to the distortions in the Ni-O bonds and thus risked mis-attributing the distortion to the wrong mode, and (b) it is the changes across the MIT phase line that determine the dominant distortion mode, which were not considered.

The conclusion to take away from this discussion is that while the nickelates may be octahedrally twisted and otherwise distorted in a number of ways, the primary change across the MIT phase boundary results from a rocksalt, breathing-mode lattice distortion of type R_1^+, wherein alternating Ni octahedra expand and collapse isotropically and roughly by an equal measure, and that furthermore there are no Jahn-Teller distortions observed (once again, see Sec. 1.4.2 to see why the Jahn-Teller modes generated so much controversy).

1.3 Metal-Insulator Transition: Introduction

The "smoking gun" kind of evidence for an MIT in the nickelates is the standard measurement of electrical resistance: this first-order phase transition is clearly indicated by the resistance curves, which shoot straight up once critical temperature is reached (see the measurements for several of the compounds in Fig. 1.6, from [6]). While the presence of the MIT is firmly established by measurements from several groups over the past

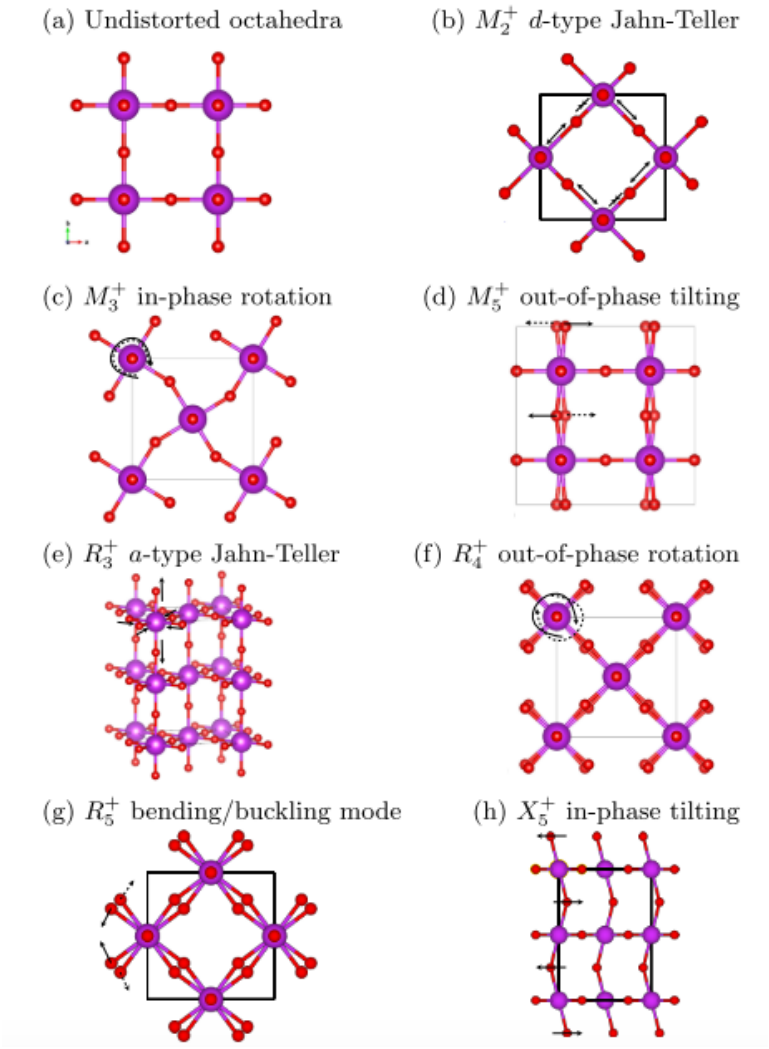

Figure 1.5: Various distortion modes available to the nickelates. Figure from Ref. [5].

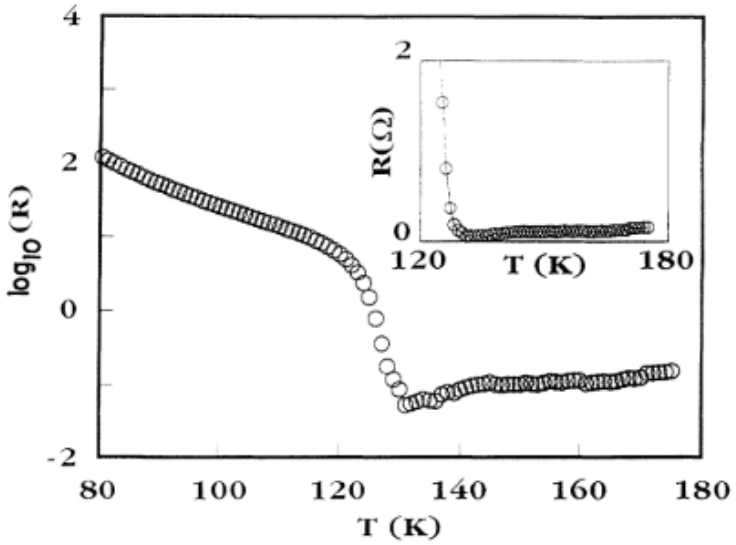

Figure 1.6: Electrical resistivity of $PrNiO_3$ as a function of temperature: the metal-insulator transition is clearly visible. Data and figure from Ref. [6].

decades [35, 42, 43], its nature and origin are not immediately obvious from these measurements alone. Before we launch into a discuss of the various possibilities, let us consider the basic electronic structure of the nickelates.

1.3.1 Formal Valence rules

When it comes to transition metal oxides and determining the formal[3] oxidation state[4] of the various components, for instance in a perovskite with the chemical formula ABX_3, it is customary to do the following. Given that the unit cell ought to be electrically neutral – otherwise the material would not be electrically stable – the valences of all the components must add up to zero. Furthermore, due to extremely high electronegativity of chalcogens (O, S, Se) and halides (F, Cl, Br, I), assume their outer shells are closed: they have stolen enough electrons to satisfy their outer shells. One can make a similar assumption about the alkali metals like Li, alkaline earth elements in the Be column, and those in the column under Sc: their low electronegativity leads them to give up their electrons in most situations. Once these

[3] *i.e.* nominal, not physically true but a useful starting point.

[4] that is, how many electrons an outer electronic subshell is gaining/losing.

are fixed, the remaining valences are determined by setting the sum total to zero: this condition can typically be satisfied because the transition metals often have a variety of diverse stable oxidation states (*e.g.* for vanadium the oxidation state can range from +2 all the way to +5). In the case of the rare-earth nickelates $R\mathrm{NiO}_3$ we can assign formal valences as follows: R, being the in Sc column, has +3. In a formula unit of $R\mathrm{NiO}_3$ there is 1 Ni and 3 O: if we insist on O^{-2}, and R is +3, that forces Ni^{+3}, or, in terms of shell structure, Ni = [Ar] $3d^7$.

Knowing the number of electrons residing in the outer shell of the Ni ions, one can, in order to describe the nickelate behaviour, attempt to construct a Hubbard-like model for the nickelates. The simplest approach is to forget about the rare-earth ions and the O bands, assuming they are far away from the Fermi level and the Ni bands, and to focus purely on the Ni conduction electrons. A Ni atom in a spherically symmetric vacuum possesses the standard hydrogen-like electronic orbitals: in fact, according to the hydrogen atom solution, all the orbitals in the Ni $n = 3$ subshell (where n is the principal quantum number[5]) have the same energy (assuming the electron-electron interactions are neglected!) and thus would all have to be included in a Hubbard model. However, the Ni atoms are not really in a vacuum, nor are they in a spherically-symmetric environment: they are surrounded by a periodic array of O and R and other Ni. In particular, each Ni atom is encased in an octahedral cage of oxygen atoms: this breaking of full rotational symmetry down to the octahedral group lifts the orbital degeneracy and significantly simplifies the model, reducing the number of states that need to be included. The effects of the surrounding O on the electronic structure of Ni are obtained within **crystal field theory**.

1.3.2 Crystal field splitting of $R\mathrm{NiO}_3$

There are excellent books available detailing the crystal field calculations for various geometries and point group symmetries, as well as the group theory involved [7, 44]. Here we will only provide a qualitative description of the calculation, omitting some of the calculation details.

Consider the total electric potential $V(\mathbf{r})$ on the electron in the outer shell of an ion of interest – say, Ni (positioned at $\mathbf{R}_0$). Treating all other

[5] which is a consequence of conservation of energy in the hydrogen atom problem. Other quantum numbers to remember are the angular quantum number l from rotational symmetry ($l = 0$ is the s orbital, $l = 1$ the p orbital, $l = 3$ the d orbital, $l = 4$ the f orbital, ...), the angular projection number m_z, and the spin projection quantum number s_z.

ions (oxygens) as point electric charges of magnitude q_a for the moment, one can write

$$V(\mathbf{r}) = \sum_a \frac{q_a}{|\mathbf{R}_a - \mathbf{r}|} = \frac{q_0}{|\mathbf{R}_0 - \mathbf{r}|} + \sum_{\substack{a \\ \text{nearest} \\ \text{neighbours}}} \frac{q_a}{|\mathbf{R}_a - \mathbf{r}|} + \sum_{\substack{a \text{ non} \\ \text{nearest} \\ \text{neighbours}}} \frac{q_a}{|\mathbf{R}_a - \mathbf{r}|} = \tag{1.3}$$

$$= V_0(\mathbf{r}) + V_{\text{lig}}(\mathbf{r}) + V_{\text{cr/lig}}(\mathbf{r}). \tag{1.4}$$

The first term is simply the spherically symmetric potential from the electron's own core ion. The second is the so-called *ligand field*, produced by the *ligands* or atoms that are immediately surrounding (bonding to) the original Ni ion. The second and the last term together comprise the *crystal field*.

It is reasonable to assume that the nearest neighbours exert the strongest influence on the electron of the ion at $\mathbf{R}_0$. Specializing to the case of a Ni ion in an octahedral cage of O, we have point charges q_O at positions $(\pm a, 0, 0)$, $(0, \pm a, 0)$ and $(0, 0, \pm a)$ (the assumption of perfect octahedra with all equal primary axes can be relaxed, but it does not change the results qualitatively). The ligand field on the electron is

$$\begin{aligned} V_{\text{lig}}(\mathbf{r}) = &\frac{q_O}{\sqrt{(x-a)^2+y^2+z^2}} + \frac{q_O}{\sqrt{(x+a)^2+y^2+z^2}} + \\ &+ \frac{q_O}{\sqrt{x^2+(y-a)^2+z^2}} + \frac{q_O}{\sqrt{x^2+(y+a)^2+z^2}} + \\ &+ \frac{q_O}{\sqrt{x^2+y^2+(z-a)^2}} + \frac{q_O}{\sqrt{x^2+y^2+(z+a)^2}}. \end{aligned} \tag{1.5}$$

Taylor expanding about $\mathbf{r} = 0$ to first order gives

$$V_{\text{lig}}(\mathbf{r}) \approx \frac{35}{4}\frac{q_O}{a^5}\left(x^4 + y^4 + z^4 - \frac{3}{5}r^4\right) = D\left(x^4 + y^4 + z^4 - \frac{3}{5}r^4\right). \tag{1.6}$$

This term manifestly breaks spherical symmetry by virtue of the x^4, y^4, z^4 factors: the hydrogen atom problem thus acquires a perturbation to the spherical Coulomb potential $1/r$ and the large degeneracy between the different subshell orbitals is lifted. One clever way to figure out how the degeneracy is lifted is using representation theory: however, the exact derivation is lengthy and interested readers are directed to Ref. [7].

To calculate the actual energy splittings and the make-up of the states in terms of the original atomic orbitals $|n, l, m_z, s_z\rangle$ it is necessary to do degenerate perturbation theory on the ligand potential $V_{\text{lig}}(\mathbf{r})$ and diagonalize

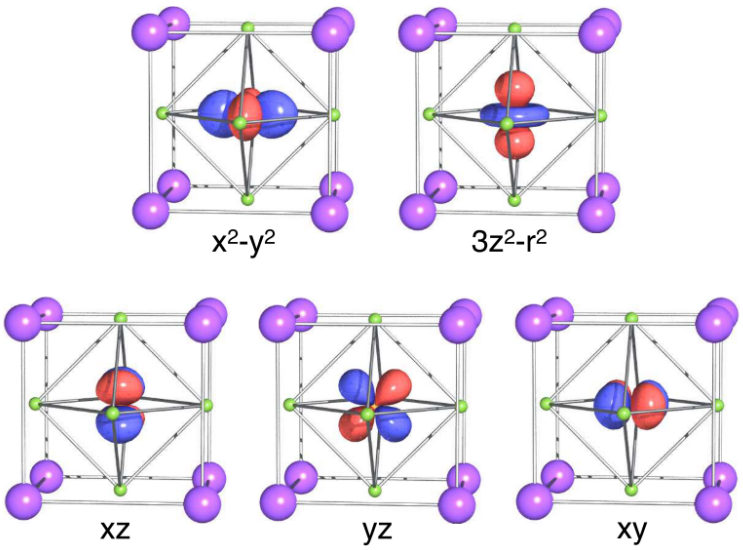

Figure 1.7: The e_g and t_{2g} manifolds resulting from crystal field splitting. Figure from Ref. [7].

the resulting crystal-field matrix to obtain the splittings. Without going in the details of the diagonalization (see Ref. [7]), we simply quote the results. After taking into account the crystal field, the degenerate d orbitals of the Ni ion split into two manifolds: a higher energy manifold called e_g (for group-theoretic reasons), which encompasses the orbitals $d_{3z^2-r^2}, d_{x^2-y^2}$; and t_{2g} with the orbitals d_{xy}, d_{yz}, d_{zx}. Intuitively, the e_g orbitals end up being higher in energy because they are oriented towards the negatively charged O ions, whereas the t_{2g} are largely in interstitial space (see Fig. 1.7).

Combining this knowledge of the new d orbitals with the previous insight about the Ni valency of $3d^7$, we conclude that the lower-lying t_{2g} triplet is completely filled, while the e_g doublet remains degenerate, with a single electron splitting its time between the two orbitals – and two possible spin projections $s_z = \pm 1/2$ – resulting in **quarter-filling** at zero temperature. This is often written as $d^7 = t_{2g}^6 e_g^1$. Thus the tight-binding model, if constructed, ought to include two bands, $|z\rangle \equiv d_{3z^2-r^2}, |\bar{z}\rangle \equiv d_{x^2-y^2}$.

While the $e_g - t_{2g}$ splitting is an adequate starting place for understanding the impact of the ligand O on the electronic properties of Ni, the simple point charge approximation leaves out important band effects. To take those into account, it is necessary to take stock of the charge-transfer energy gap between the Ni and O bands, which we discuss next within the

Zaanen-Sawatzky-Allen framework [45].

1.3.3 Zaanen-Sawatzky-Allen scheme

In this discussion we draw on an excellent reference by George Sawatzky and Robert Green [8]. Standard band theory, motivated by the tight-binding model, assigns only one criterion for judging whether a material is a metal or an insulator: the parity of the number of electrons per unit cell. If the number is odd, then the outermost band is only partially occupied and the material is a metal. Conversely, an even number of electrons means the band is fully occupied, and in the presence of a finite band gap between the occupied (valence) band and the next higher, unoccupied (conduction) band, the material is insulating (this is well-described in many solid-state textbooks). The success of this model was astounding, but brief: it was quickly realized that there were a variety of materials, most notably transition-metal oxides, which were insulating despite formally having an odd number of electrons in the unit cell.

To address this discrepancy, Mott and Hubbard pointed out that interactions between electrons must be taken into account [46, 47]. The Mott-Hubbard model, which incorporates the electron-electron interactions only between electrons at a given site, was already a significant improvement: it was able to show exactly how electron-electron interactions were forcing the localization of electrons, thus rendering the materials insulating. Without interactions the Fermi level would sit in the middle of the outer electron band: the system would have many states which could potentially respond to an applied current (which is what conduction *is*). Instead, the electrons' mutual Coulomb repulsion (whose strength is characterized in the model by the value U) opened a gap in the density of states at the Fermi level, splitting the band in two, and eliminating any states that were once accessible for conduction, effectively confining the electrons to their "home cell" (see Fig. 1.8 for a useful graphic).

However, soon this was also revealed not to be the whole story. Transition metal oxides nominally incorporate both transition metal $3d$ bands and oxygen $2p$ bands in their bandstructure. Typically it is assumed that the oxygen bands are valence and are way below the transition-metallic bands: however, in many oxides that is not the case. In fact the bandstructure can be such that the lowest energy excitations actually involve the an electron hopping from the oxygen band to the transition-metal band, or yet more exotic possibilities. This was the chief insight of Zaanen, Sawatzky and Allen [45], who in 1985 classified the possibilities for such compounds

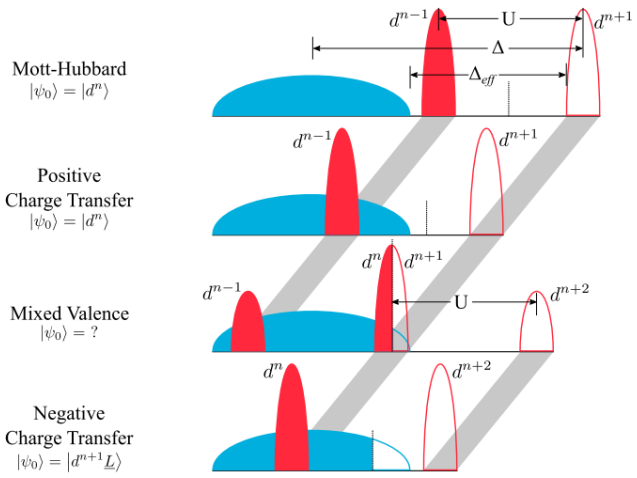

Figure 1.8: A graphic depicting the Zaanen-Sawatzky-Allen classification scheme, using featureless densities of electronic states without hybridization. Figure from Ref. [8].

in terms of the Hubbard U and the charge-transfer energy Δ: this latter energy scale characterizes the energy cost of the electron hopping from the transition-metal atom to the ligand oxygen.

The different possibilities coming from the interrelationship of U and Δ are depicted in Fig. 1.8. They range from a full-on Mott-Hubbard situation, where the oxygen band indeed plays no role; to a positive charge transfer case where the lowest-order excitations are of $d^n\underline{L}^0 \rightarrow d^{n+1}\underline{L}^1$ type ($\underline{L}$ indicates a hole state on the ligand oxygen); to a mixed valence state that is somewhat difficult to understand and we will not discuss much here; and, finally, negative charge transfer insulators, which is what the nickelates $R\mathrm{NiO}_3$ are believed to be in the ZSA scheme. The idea behind the negative charge transfer insulator is that $\Delta < 0$ and it is thus energetically favourable for the oxygen $2p$ electron to migrate toward the Ni : this situation is sometimes called **self-doping**. The structure of the lowest order excitations in the various scenarios is depicted in Fig. 1.9.

The crucial takeaway from the ZSA analysis is that, unlike in the formal valence counting in Sec. 1.3.1, the correct starting point for constructing a Hubbard model for the Ni should be the $d^8\underline{L}^1$ state, not d^7. This has serious implications for the picture of the charge order and the metal-insulator transition, as we will see shortly.

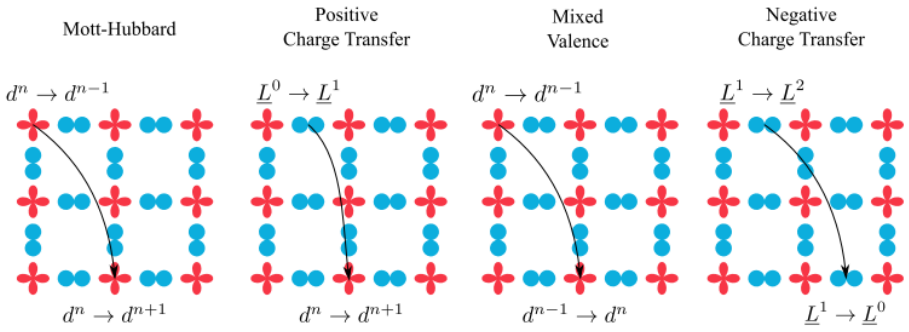

Figure 1.9: The lowest order excitations within the Zaanen-Sawatzky-Allen classification scheme. Figure from Ref. [8].

1.4 Metal-Insulator Transition: Mechanisms

Armed with the understanding of the basic facts about the Ni valency, orbitals and bandstructure, we can now start addressing the question of the metal-insulator transition and the various mechanisms that have been proposed.

1.4.1 Mechanism: Charge-transfer gap

In the simplest and one of the earliest pictures, as the temperature is lowered, a charge-transfer gap appears in the band structure of the nickelates, leading to insulating behaviour [16]. However, this does not readily account in any way for the structural lattice distortions which are present in this material and thus is not considered an adequate theory at this point.

1.4.2 Mechanism: Jahn-Teller effect

A good rule of thumb when it comes to electronic systems is that "nature abhors an orbital degeneracy"[48]. Whenever there is a possibility of lifting a degeneracy, it is generally done, unless the degeneracy is protected by symmetry. So it should come as no surprise that the remaining degenerate e_g doublet could have a natural way of resolving its degeneracy: in the case of a perovskite lattice, one such possibility is known as the Jahn-Teller effect. In short, it comes from the interaction between the electronic orbitals and lattice vibrational modes. The interaction produces a "cooperative distortion" of the lattice, elongating the O octahedra preferentially along one axis. This

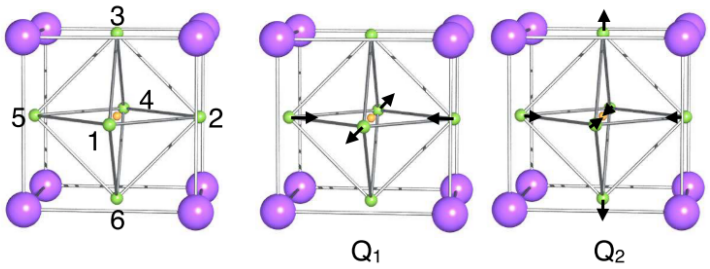

Figure 1.10: The unit cell of $KCuF_3$ and the associated JahnTeller distortion modes. Figure from Ref. [7].

splits the e_g doublet and produces a kind of orbital order. A derivation of the Jahn-Teller effect from a Theory-of-Everything Hamitlonian is beyond the scope of this thesis: an excellent introduction is given in Ref. [7].

A typical example of a Jahn-Teller system is $KCuF_3$, another perovskite: see the two possible distortion modes in Fig. 1.10. Intuitively, the Q_2 mode brings the negatively charged O closer to the branches of $d_{x^2-y^2}$ and so raises its energy, while pushing other O away from $d_{3z^2-r^2}$ and lowering its energy – and in so doing, lifts the degeneracy.

In light of this well-studied phenomenon, and given that with the open outer subshell structure $t_{2g}^6 e_g^1$ the nickelates are expected to be Jahn-Teller active [38] (due to the unpaired electron in a degenerate pair of orbitals), it was reasonable to suggest that a Jahn-Teller distortion is what resolves the electronic degeneracy and results in insulating behaviour below a certain temperature [31, 49]. At high temperatures, itinerant[6] electrons possess large kinetic energy (the bandwidth W is large) that dominates the Jahn-Teller distortion and suppresses it, so the (electric) conduction is largely unaffected.

Many in the literature assert that, despite decades of research, no discernible Jahn-Teller like (orthorhombic) distortion was found [27, 35, 39, 42, 50, 51] – even though they might cite papers that explicitly say that Jahn-Teller distortions are present (such as in [41]). Moreover, some researchers suggest that neutron diffraction studies show that the change of the point group across the MIT phase line would not even be consistent with a Jahn-Teller distortion: the change is such that the unit cell appears to double, resulting in two inequivalent Ni sites – whereas a Jahn-Teller dis-

[6] *i.e.* not localized – typical Bloch states in metals that are distributed over almost the entire sample.

tortion would operate in the same way within all octahedral O cages [52]. However, others are suggesting that a Jahn-Teller distortion is indeed observed [4, 41, 49, 53]: they point to an increase in the distortion parameter $\Delta_d = (1/6)\sum_{n=1,...6}[(d_n - \langle d\rangle)/\langle d\rangle^2]^2$ as one follows the nickelate series from La to Lu, at room temperature. However, as we already discussed above in Sec. 1.2 on the structural transition in the nickelates, a variety of different types of distortion could potentially occur in the nickelates. Any of them could affect this very general parameter Δ_d, without necessarily serving as evidence for Jahn-Teller distortions. The more recent studies already mentioned that apply a sophisticated symmetry based mode decomposition analysis for the distortions seem to concur that a breathing-mode distortion, rather than a Jahn-Teller one, is the main contribution to the lattice distortion of the nickelates across the MIT. Ref. [54] explains nicely how the same data (*e.g.* Ni-O bonds lengths) could have been interpreted in favour of different theories by different researchers.

In summary, with some degree or certainty one could conclude that Jahn-Teller distortions are not responsible for charge order, as there are no Jahn-Teller distortions observed: although a possibility of a dynamic Jahn-Teller effect, which would not be readily picked up by the various X-ray and neutron diffraction experiments (as they time-average the measurements), has not yet been conclusively ruled out [41].

1.4.3 Mechanism: Charge disproportionation

An alternative proposed microscopic explanation accounting for the MIT is the effect of charge disproportionation (CD). Neighbouring Ni ions, nominally each being of d^7 valency, spontaneously form pairs with alternating valence $d^{7-\delta}d^{7+\delta}$ (equivalently this is often written $\mathrm{Ni3} - \delta\mathrm{Ni}^{3+\delta}$), where δ is the magnitude of the charge disproportionation [4, 35–37, 42, 48, 50, 55]. This happens to lift the e_g degeneracy without requiring Jahn-Teller distortion, and would preferentially couple to breathing-mode type distortions[7], as opposed to Jahn-Teller like distortions [54]. The breathing mode distortion makes sense in light of the changes of ionic radii with the introduction of a non-zero δ. This charge density wave then impedes conduction in the usual Mott-Hubbard insulator sense, opening a gap at the Fermi surface. However, there are some issues with this approach. Firstly, a charge density wave can only occur for Hund's coupling J[8] large enough to compensate

[7] *i.e.* ones where alternating O octahedra expand and contract.

[8] Hund's coupling J is the strength of the exchange interaction in an electronic system: typically smaller than U, it prefers to arrange the electrons into a state that maximizes

for the prohibitive cost of double occupancy U [48]: this indeed seems to be the case in the nickelates [32]. But that kind of ratio between U and J would make it energetically favourable to transfer the electron away from O and onto Ni (alternatively, a hole from Ni to O), thus making a $3d^7$ configuration an inappropriate starting point (as discussed in terms of the ZSA framework in Sec. 1.3.3). Second, on more experimental grounds, it appears to directly contradict resonant soft-x-ray diffraction measurements probing the Ni d orbital occupation [56].

1.4.4 Mechanism: Negative charge-transfer theory

An alternative view, motivated by the Zaanen-Sawatzky-Allen framework [45], holds that the nickelates are a negative-charge transfer insulator: that is, the energy cost Δ (the charge-transfer energy) of occupying a Ni d orbital versus an oxygen p orbital is such that $\Delta < U$ and in addition $\Delta < 0$ [18–22]. This forces a hole into the oxygen band (effectively *self-doping* the material), resulting in a $d^8\underline{L}$ Ni valency state ($\underline{L}$ denotes a ligand (oxygen) hole). Subsequently, electron-phonon coupling results in a breathing-mode distortion of the lattice, which couples to a charge order of the form $(d^8\underline{L})_i(d^8\underline{L})_j \rightarrow (d^8\underline{L}^2)_{S=0}(d^8)_{S=1}$. Since each hole on the oxygens is shared equally by both Ni that are bonded to it, there is no actual overall movement of charge: both O cages have the same average hole concentration [32]. But when two holes are present on a Ni (collapsed) octahedron, the phase of their wavefunctions is modified to acquire the symmetry of the Ni e_g orbitals. The pair of holes then locks into a singlet with the Ni electrons, resulting in an effectively $3d^6$ Ni configuration, which is not susceptible to Jahn-Teller distortions. Meanwhile the expanded Ni octahedron, left with no holes, orders as a triplet with $S = 1$, which allows the material to order magnetically (and acting in effect just like charge disproportionation would during most experimental probes).

These different mechanisms of how the MIT actually proceeds are not merely questions of interpretation of data: different modeling approaches, treating the electronic structure to varying degrees of sophistication, have to be implemented depending on which of the mechanisms one believes to be correct. We use many of the considerations laid out here (Ni valence counting, crystal-field splitting, the Zaanen-Sawatzky-Allen framework, absence (maybe?) of Jahn-Teller distortions and orbital order) when we construct our model in Ch. 2.

the local spin – justifying that old adage from chemistry, Hund's rule.

1.5 Magnetic Transition: Introduction

There are a few key experimental signatures that signal the onset of magnetic ordering, such as a divergence in magnetic susceptibility, or the sudden appearance of a nonzero atomic magnetic moment (picked up usually through neutron scattering). The first indications of magnetic behaviour in the nickelates were observed by the team Demazeau *et al.* that originally synthesized the material series in the early 70s [14]. It was not until the late 80s and early 90s that magnetic phenomena in the nickelates started to attract more widespread attention [38, 57–59]. An excellent plot of the Ni magnetic moment with temperature is depicted in Fig. 1.11: the spontaneous transition to a magnetically ordered state with temperature is clearly visible.

After a great deal of work it emerged that all of the members of the Ni family possess nontrivial, magnetically ordered ground states at low enough temperatures (except for $LaNiO_3$ which is assumed to stay paramagnetic down to the lowest temperatures – although there is very recent work that is calling this into question [24]). Two of the members of the family, Nd and Pr, experience the magnetic transition simultaneously with the MIT: the transition is first order [3]. Meanwhile the rest of the family up to Lu undergoes a second-order transition, with the transition temperature T_N trending upward as one approaches Lu. This is encapsulated in the canonical phase diagram showed in an earlier section 1.1.

Much work since those days has been devoted to characterizing this low-temperature magnetically ordered state, primarily though neutron diffraction measurements [9, 28, 38, 49, 56, 60, 61]. Due to the difficulty of producing large enough single crystal samples, the alignment of the local magnetic moments (both from the Ni and the rare-earth sublattices) remains a mystery: however, it has been conclusively established that whatever the alignment may be, it obeys the ordering wavevector $\mathbf{Q}_m = \frac{2\pi}{a}[\frac{1}{4}, \frac{1}{4}, \frac{1}{4}]$ ($\frac{2\pi}{a}[\frac{1}{2}, 0, \frac{1}{2}]$ in the perovskite lattice notation). This effectively means that the unit cell of the nickelate ought to include 4 separate, linearly coordinated Ni octahedral sites: only after the fourth site does the magnetic order repeat itself. The emergence of this ordering peak can be clearly seen in Fig. 1.12, where it is marked in the perovskite notation.

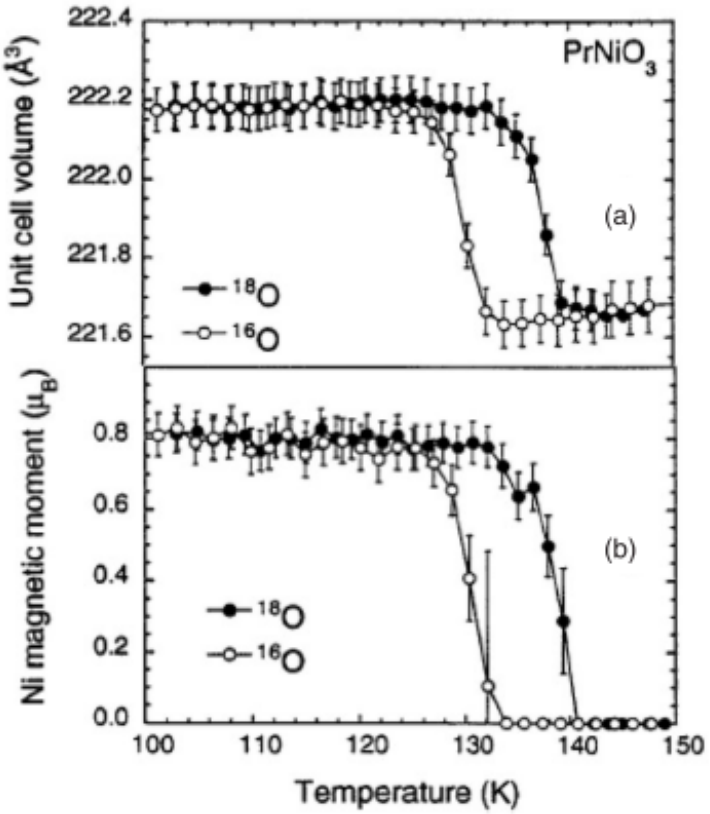

Figure 1.11: The Ni magnetic moment in $PrNiO_3$ as a function of temperature, with the onset of magnetism clearly visible. Figure from Ref. [4].

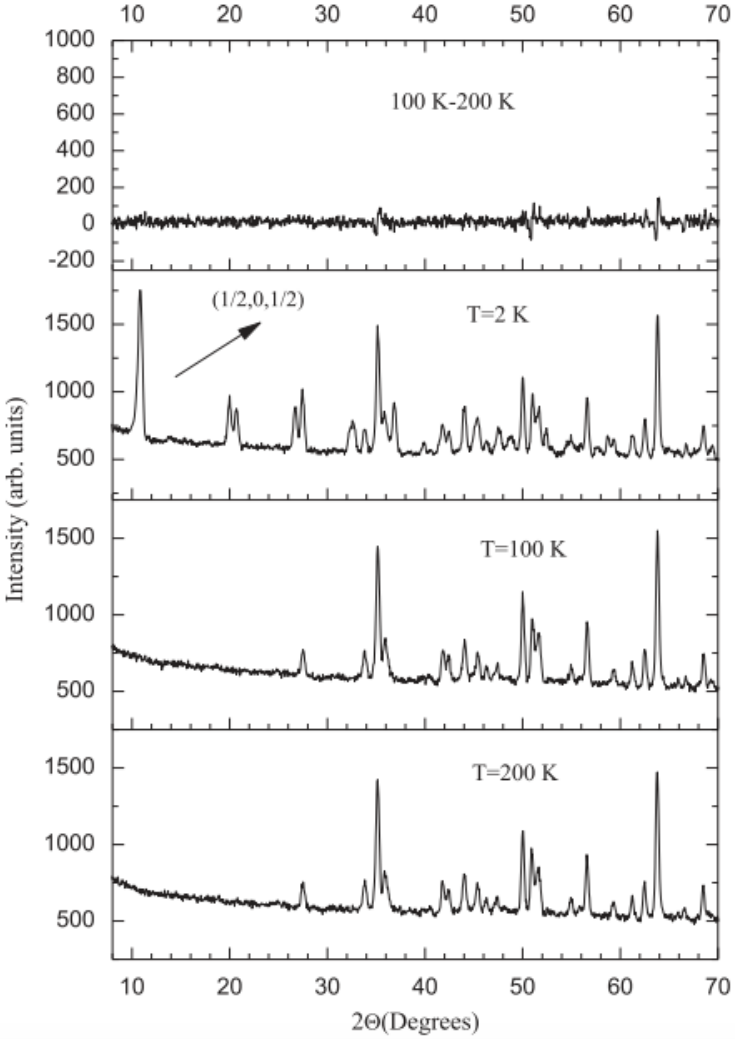

Figure 1.12: The appearance of a new ordering peak in neutron diffraction data for $DyNiO_3$ as the temperature is lowered past the magnetic transition temperature T_N. Figure from Ref. [9].

1.6 Magnetic Transition: Mechanisms

At present it is not known what the mechanism of magnetization is in the nickelates: nor is it known what the alignment of local magnetic moments is. This state of affairs fuels much of the current interest in the nickelates: it ranges from attempts to grow larger crystals[9] [24] to be able to get at the order experimentally – say through a scanning-tunneling microscopy (STM) experiment or inelastic neutron diffraction – to theoretical attempts to model the nickelates and thus make a prediction for the alignment using either effective band models, like in this thesis or as Lee *et al.* for in Ref. [26], or *ab initio* methods [1, 2, 19, 25, 39]. There are a variety of propositions as to how the magnetic order arises, which are separate from the propositions regarding what the order actually is.

One idea for the appearance of the order is that it is due to an orbital superlattice, triggered, in turn, by the orthorhombic distortions of the nickelates away from perfect perovskite lattice structure [62]. The presence of this distortion results, potentially, in (very weak) orbital order: but if the energy splitting introduced by it is comparable to the exchange coupling between the different orbitals on the same Ni site, a new energy-favourable configuration becomes available wherein two sublattices with different orbital occupancy emerge. Then, given a Ni site, if its neighbour has the same orbital occupancy, they are antiferromagnetically coupled through the oxygen $2p$ bands (superexchange); if it has the opposite orbital occupancy, then it is preferential for the spins to align ferromagnetically. This scenario would reproduce the experimentally observable wavevector $\mathbf{Q}_m$: locally, it would result in the magnetic order of type $\uparrow\uparrow\downarrow\downarrow$.

Another possibility is, once again, cooperative Jahn-Teller distortions. The mechanism here would be very similar: orbital order would couple with magnetic exchange interactions to spontaneously generate two inequivalent sublattices with AF coupling between same-orbital occupancy neighbours and FM coupling between opposite-orbital ones. The crucial distinction here is the origin of the orbital order: it would be assumed due to the elongation of the Ni octahedra. However, we again reiterate here that no Jahn-Teller like distortion has been observed for the nickelates.

It would appear that one could disentangle the order generated by the orbital versus the spin degrees of freedom by studying the neutron scattering peaks of Ni family members with $T_{\mathrm{MIT}} > T_{\mathrm{N}}$: one might hope that the

[9] The problem is that a variety of different orders, such as $\Uparrow 0 \Downarrow 0$ or $\Uparrow\Uparrow\Downarrow\Downarrow$ cannot be distinguished from one another during a neutron diffraction study on a powder.

precursors of orbital order exist already above T_N. However, a study with Sm placed very stringent bounds on the magnitude of these peaks, if they exist ($< 10^{-4}$ of the largest peak typically observed in the study).

Clearly, much more work needs to be done to fully understand the character of the magnetic order and the magnetic transition at low temperature: that is the main purpose of this thesis.

Chapter 2

Effective Two-Band Model for the Rare-Earth Nickelates

> All models are wrong, but some are useful.
>
> George Box (1987)

Now that we have extensively reviewed the status of experimental and theoretical work to date, especially when it comes to the metal-insulator transition and the magnetic order, the stage is set for constructing a phenomenological, microscopic tight-binding model for the nickelates. The considerations in the previous chapter should make clear as to what aspects of the physics ought to be included, and what can be neglected or treated phenomenologically as a renormalization to the model parameters.

Given that the octahedral twists do not appear to change drastically across the MIT or the magnetic phase line and thus apparently do not couple much to the electronic/magnetic degrees of freedom, for simplicity we take $R\mathrm{NiO}_3$ as having a perfect (pseudo)cubic perovskite lattice, with lattice constant a. In light of the crystal field and formal valence discussions, we will concentrate on two e_g "effective" Ni orbitals for the tight-binding model, $|z\rangle \equiv d_{3z^2-r^2}, |\overline{z}\rangle \equiv d_{x^2-y^2}$.

We call the orbitals effective, because we believe that in reality the point-charge model for the Ni orbital crystal field splitting is incomplete: it omits any mention of the O $2p$ bands, or of the holes on the O due to negative charge transfer. If one believes in the charge disproportionation mechanism of the MIT, the O bands are assumed inert and thus the simplistic crystal field treatment described above is essentially accurate: so the e_g bands in the model would really be the e_g bands of the Ni.

However, that is not quite so in the negative charge transfer picture. When considering a single Ni octahedron, the holes on the O are found to be those linear combinations of the p_σ O orbitals that exhibit e_g character [32]. This makes sense, as e_g-like O orbital combinations are the ones with max-

imum overlap with the Ni e_g doublet: they are most likely to hybridize and donate an electron to the Ni, leaving behind the ligand hole and producing the $3d^8\underline{L}$ state in the first place. Hence the ligand hole states can be thought of as "effective" e_g orbitals: the analogy does not fully bear out because such orbitals would not actually be orthogonal between nearest-neighbour sites and in fact need to be built up in the Wannier states manner from a variety of more extended Ni and O states. This could potentially strongly renormalize the hopping and interaction parameters as compared to their bare values. More than that, some recent results suggest that even the make-up of the bands – *i.e.* what e_g, t_{2g} and other bands are active in the model – could dynamically respond to things like site occupation and crystal lattice distortion [63]. We deal with this by letting the model parameters vary and seeing what states obtain within the larger parameter space.

Now that we settled what the lattice is and what orbitals to include, we can readily write down all the ingredients of a microscopic tight-binding model. We will work at zero temperature for simplicity, as we are interested mostly in the magnetic order that obtains at very low temperatures in the nickelates. At the same time, we can represent sweeping the nickelate series by adjustments in the model parameters. Roughly speaking, while swapping out the rare-earth ion affects the bond angles in the crystal and so significantly modulates the bandwidth (which is determined by various nearest-neighbour hopping amplitudes T_i in our model), it does little to change the on-site Coulomb repulsion. Thus changing the hopping rate can represent the effect of continuously sweeping through the entire nickelate series.

As the importance of the lattice has already been established [31, 32, 39, 51], we introduce the lattice semiclassically and couple it to the tight-binding model via an on-site coupling, with the goal of demonstrating explicitly the forcing of charge disproportionation by the lattice and to investigate the impact of the lattice on the ground state magnetic order. Finally, we treat the electron-electron interactions by employing the standard spherically symmetric Kanamori Hamiltonian for the case of two bands. Our Hamiltonian will thus have the general form

$$\hat{H} = \hat{T} + \hat{H}_{e-e} + \hat{H}_{latt} + \hat{H}_{e-latt}. \tag{2.1}$$

We use electronic creation and annihilation operators $d^\dagger_{ia\sigma}, d_{ia\sigma}$ to create and destroy electrons in an orbital a with spin σ on site i. In what follows, we build up the Hamiltonian 2.1 piece by piece.

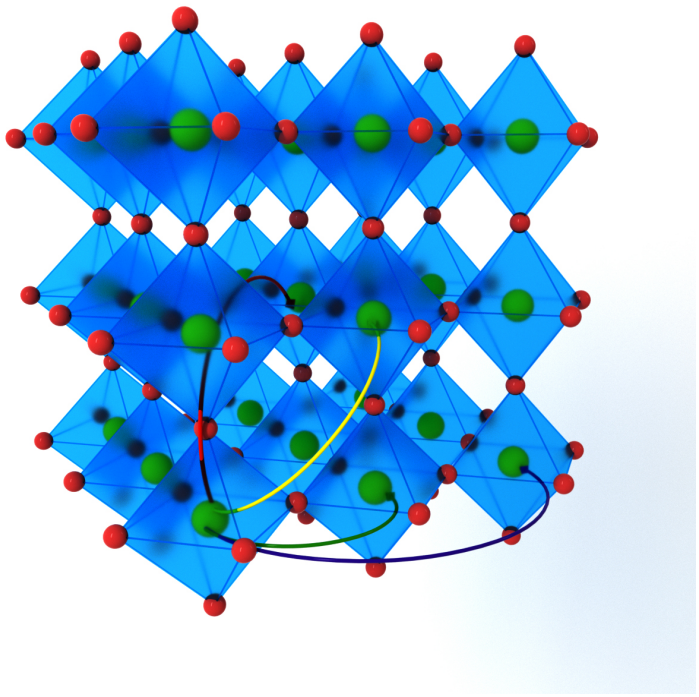

Figure 2.1: A schematic diagram of the various hoppings included in the nickelates two-band model. The green arrow corresponds to the first neighrest neighbour hopping; the yellow to second nearest neighbour hopping; third nearest neighbour hopping, represented by the red arrow, is not included due to minimal orbital overlap; and fourth nearest neighbour hopping is shown by the purple arrow.

2.1 Hopping

We know from neutron scattering measurements to expect a linearly coordinated 4-site magnetic order in the nickelates It is necessary then to include first nearest neighbour (with amplitude t_1), second-nearest neighbour (t_2) and fourth-nearest neighbour (t_4) hopping, where the "nearness" of the neighbours is indicated in Fig. 2.1 and is purely spatial. The hopping part of the Hamiltonian reads

$$\hat{T} = \hat{T}_1 + \hat{T}_2 + \hat{T}_4. \tag{2.2}$$

Let us work through these sequentially. We will explicitly write out

all the hoppings in the various directions: we will use notation like $d_{i+x,x\sigma}$ where the first x is a vector translating us one lattice constant length along x to the next Ni site (with respect to the original site, for which we use a condensed 3-dimensional label i), and the second x is the orbital $\left|3x^2 - r^2\right\rangle$, which is the equivalent of $|z\rangle = \left|3z^2 - r^2\right\rangle$ "polarized" along the x direction, which allows hopping along x. The reason we have states like $\left|3x^2 - r^2\right\rangle$ is because while we have only two true orbitals $|z\rangle$ and $|\bar{z}\rangle$, the choice of the z axis is arbitrary: we could have equally well have chosen x as the z axis and still would have had an e_g member "polarized" along that axis. We can always write all these orbitals in terms of $|z\rangle = \left|3z^2 - r^2\right\rangle, |\bar{z}\rangle = \left|x^2 - y^2\right\rangle$ by remembering what the decomposition of these orbitals is in terms of (real) spherical harmonics

$$|x\rangle \equiv \left|3x^2 - r^2\right\rangle = -\frac{1}{2}|z\rangle + \frac{\sqrt{3}}{2}|\bar{z}\rangle\,, \quad |y\rangle \equiv \left|3y^2 - r^2\right\rangle = -\frac{1}{2}|z\rangle - \frac{\sqrt{3}}{2}|\bar{z}\rangle\,. \tag{2.3}$$

2.1.1 1^{st} nearest neighbour hopping

With these orbitals, the nearest neighbour hopping contribution is

$$\hat{T}_1 = -t_1 \sum_{i\sigma} \Big[d^\dagger_{iz\sigma} \left(d_{i+z,z\sigma} + d_{i-z,z\sigma}\right) + d^\dagger_{ix\sigma} \left(d_{i+x,z\sigma} + d_{i-x,z\sigma}\right) + \\ + d^\dagger_{iy\sigma} \left(d_{i+y,z\sigma} + d_{i-y,z\sigma}\right) \Big]. \tag{2.4}$$

Of course, nearest neighbour hopping is not possible for the $|\bar{z}\rangle$ orbital along the z direction, because these orbitals have no overlap with the ligand O in that direction. The hopping is possible along the x and y directions, but we choose to consider the hopping through $|z\rangle$ (and $|z\rangle$-like orbitals polarized along different axes) as dominant and so neglect this fact.

This quadratic Hamiltonian can be readily brought to almost diagonal form (save for the orbital subspace) by Fourier transforming to $\mathbf{k}$ basis, using the prescription

$$d^\dagger_{\mathbf{k}a\sigma} = \sum_i \frac{e^{i\mathbf{k}\mathbf{R}_i}}{\sqrt{N}} d^\dagger_{ia\sigma}, \tag{2.5}$$

where $\mathbf{k}$ ranges over the full cubic Brillouin zone $-\frac{\pi}{a} < k_\eta < \frac{\pi}{a}$, $\eta = x, y, z$.

Using this gives (the details of the calculation are in Appendix A):

$$\hat{T}_1 = -t_1 \sum_{\mathbf{k}\sigma} \Big[t^1_{zz}(\mathbf{k}) d^\dagger_{\mathbf{k}z\sigma} d_{\mathbf{k}z\sigma} + t^1_{\bar{z}\bar{z}}(\mathbf{k}) d^\dagger_{\mathbf{k}z\sigma} d_{\mathbf{k}z\sigma} + \\ + t^1_{z\bar{z}}(\mathbf{k}) (d^\dagger_{\mathbf{k}z\sigma} d_{\mathbf{k}\bar{z}\sigma} + d^\dagger_{\mathbf{k}\bar{z}\sigma} d_{\mathbf{k}z\sigma}) \Big], \tag{2.6}$$

with

$$\begin{aligned} t^1_{zz}(\mathbf{k}) &= 2\cos(k_z a) + \frac{1}{2}[\cos(k_x a) + \cos(k_y a)], \\ t^1_{\bar{z}\bar{z}}(\mathbf{k}) &= \frac{3}{2}[\cos(k_x a) + \cos(k_y a)], \\ t^1_{z\bar{z}}(\mathbf{k}) &= -\frac{\sqrt{3}}{2}[\cos(k_x a) - \cos(k_y a)]. \end{aligned} \tag{2.7}$$

2.1.2 4st nearest neighbour hopping

With the $\hat{T}_1$ prescription in our pocket, we can immediately write down the $\hat{T}_4$ operator. Since the 4th neighbour hopping is through the same orbitals as the 1st neighbour hopping, the form of the operators is still the same, save for the displacement vector being $2a \cdot \hat{x}, \hat{y}, \hat{z}$. Hence the result ought to be the same as $\hat{T}_1$, except the cosines are now over twice the lattice constant, $\cos k_x a \to \cos 2k_x a$ and so on. Explicitly,

$$\hat{T}_4 = -t_4 \sum_{\mathbf{k}\sigma} \Big[t^4_{zz}(\mathbf{k}) d^\dagger_{\mathbf{k}z\sigma} d_{\mathbf{k}z\sigma} + t^4_{\bar{z}\bar{z}}(\mathbf{k}) d^\dagger_{\mathbf{k}z\sigma} d_{\mathbf{k}z\sigma} + \\ + t^4_{z\bar{z}}(\mathbf{k}) (d^\dagger_{\mathbf{k}z\sigma} d_{\mathbf{k}\bar{z}\sigma} + d^\dagger_{\mathbf{k}\bar{z}\sigma} d_{\mathbf{k}z\sigma}) \Big], \tag{2.8}$$

with

$$\begin{aligned} t^4_{zz}(\mathbf{k}) &= 2\cos(2k_z a) + \frac{1}{2}[\cos(2k_x a) + \cos(2k_y a)], \\ t^4_{\bar{z}\bar{z}}(\mathbf{k}) &= \frac{3}{2}[\cos(2k_x a) + \cos(2k_y a)], \\ t^4_{z\bar{z}}(\mathbf{k}) &= -\frac{\sqrt{3}}{2}[\cos(2k_x a) - \cos(2k_y a)]. \end{aligned} \tag{2.9}$$

2.1.3 2nd nearest neighbour hopping

This leaves the slightly more complicated 2nd neighbour hopping, where the hopping proceeds through mixed orbitals along multiple directions at once,

in one of the three planes xy, yz, zx. Only the origin and destination matter for the hopping: we catalog the hopping contributions in terms of them. There are 12 possible destinations, 4 in each of the principal planes. In general the hopping term will look like this

$$\hat{T}_2 = -t_2 \sum_{iab\sigma,\hat{\tau}\neq\hat{\mu}} d^\dagger_{i+\hat{\tau}+\hat{\mu},a\sigma} d_{ib\sigma} + \text{ h.c.}, \tag{2.10}$$

with $\hat{\tau}, \hat{\mu}$ ranging over $\pm a \cdot \hat{x}, \hat{y}, \hat{z}$. However, notice that during such a hop the electron always ends up in an orbital that is different from the one it started in. For instance, hopping $\hat{x} + \hat{y}$ forces the orbital to go either $x \to y$ or $y \to x$, depending on what orbital the electron started in (the orbital will change "virtually", while the electron hops through a virtual site, but the absence of any overlap between $|z\rangle$ and $|\overline{z}\rangle$ does not allow orbitals to change on real sites). Let us adopt the convention that in the site indices, order matters: in other words, if we have an index $i + \hat{x} + \hat{y}$, that means we first hop along $\hat{x}$ and then along $\hat{y}$. Then it is clear that the starting orbital index b will be the same as the first hop displacement $\hat{\tau}$ – after all, if an electron starts in the y orbital, it can only (initially!) hop along y. This allows us to set $b = \tau$ and $a = \mu$. After that, it is a matter of carefully Fourier transforming all the 12 hopping destinations. The final result is (the details are in Appendix A)

$$\hat{T}_2 = -2t_2 \sum_{\mathbf{k}\sigma} \Big[t^2_{zz}(\mathbf{k}) d^\dagger_{\mathbf{k}z\sigma} d_{\mathbf{k}z\sigma} + t^2_{\bar{z}\bar{z}}(\mathbf{k}) d^\dagger_{\mathbf{k}\bar{z}\sigma} d_{\mathbf{k}\bar{z}\sigma} + \\ + t^2_{z\bar{z}}(\mathbf{k}) (d^\dagger_{\mathbf{k}z\sigma} d_{\mathbf{k}\bar{z}\sigma} + d^\dagger_{\mathbf{k}\bar{z}\sigma} d_{\mathbf{k}z\sigma}) \Big], \tag{2.11}$$

with

$$\begin{aligned} t^2_{zz}(\mathbf{k}) &= 2\cos(k_x a)\cos(k_y a) - 2\cos(k_z a)(\cos(k_y a) + \cos(k_x a)), \\ t^2_{z\bar{z}}(\mathbf{k}) &= \sqrt{3}\cos(k_z a)(\cos(k_x a) - \cos(k_y a)), \\ t^2_{\bar{z}\bar{z}}(\mathbf{k}) &= -3\cos(k_x a)\cos(k_y a). \end{aligned} \tag{2.12}$$

All of the different hopping contributions can be combined to give the usual form for $\hat{T}$

$$\hat{T} = \sum_{\mathbf{k}ab\sigma} t_{ab}(\mathbf{k}) d^\dagger_{\mathbf{k}a\sigma} d_{\mathbf{k}b\sigma}, \tag{2.13}$$

The coefficients can be found at the end of Appendix A.

2.2 Lattice contributions

Let U_j be a distortion parameter characterizing the structural distortion at site j. At the semiclassical level, where in addition the phonon modes of the material are assumed to be incredibly heavy, the dynamical (momentum) contribution to the phonon energy can be neglected, and the lattice energy is primarily determined by the distortion parameter U_j. In accordance with experimental data described in an earlier section, it appears entirely justified to treat the main contribution to the lattice energy as that coming from an isotropic breathing-mode distortion mode R_1^+ (for a depiction of the mode see again Fig. 1.5). Specifically, the Ni octahedra are assumed to expand-contract in a checkerboard-like (also called breathing-mode like, also called rocksalt like) pattern, with the expansion/contraction isotropic and roughly equal in magnitude (opposite in sign). Thus the distortion parameter U_j is a simple scalar, and its energy can be written

$$H_{latt} = \sum_j \left(\frac{k}{2} U_j^2 + \frac{A}{4} U_j^4 \right). \tag{2.14}$$

where for greater generality the anharmonic terms U_j^4 have been included. For convenience, re-scale the distortion magnitude to extract the lattice coupling energy scale by non-dimensionalizing the lattice distortion parameter $u_j = kU_j/g$: this results in

$$H_{latt} = \epsilon_b \sum_j \left(\frac{1}{2} u_j^2 + \frac{\alpha}{4} u_j^4 \right), \quad \epsilon_b = g^2/2k, \quad \alpha = Ag^2/2k^3. \tag{2.15}$$

So long as the value of the distortion is known, the contribution to the energy can be readily evaluated with this expression.

2.3 Electron-electron interactions

As there are assumed to be two degenerate bands in the e_g manifold, there are markedly more options for electron-electron processes spurred on by the Coulomb interaction than there are in a single-band Hubbard model. Interaction models of this kind have been studied previously: the generalization to two bands is called the Kanamori [64–66] (sometimes Slater-Kanamori

[19]) Hamiltonian, with the general form

$$H_U = U \sum_{i\alpha} \hat{n}_{i\alpha\uparrow}\hat{n}_{i\alpha\downarrow} + U' \sum_{i\sigma} \hat{n}_{iz\sigma}\hat{n}_{i\bar{z}\bar{\sigma}} + \tag{2.16}$$

$$+ (U' - J) \sum_{i\sigma} \hat{n}_{iz\sigma}\hat{n}_{i\bar{z}\sigma} - J \sum_{i\sigma} d^\dagger_{iz\sigma} d_{iz\bar{\sigma}} d^\dagger_{i\bar{z}\bar{\sigma}} d_{i\bar{z}\sigma} + \tag{2.17}$$

$$+ J \sum_{ia} d^\dagger_{ia\uparrow} d_{i\bar{a}\uparrow} d^\dagger_{ia\downarrow} d_{i\bar{a}\downarrow}. \tag{2.18}$$

The derivation of this interaction is beyond the scope of this thesis: interested readers may be directed to [67]. Here we merely outline an intuitive understanding of its behaviour. The first two terms should be familiar: they are merely the usual Hubbard-like density-density interaction terms. The presence of J signifies Hund's exchange interaction that arises in the presence of more than one orbital, reflecting the varying cost of occupying the two orbitals with various spin orientations. A useful heuristic is Hund's rule, which states that in the absence of other energy splitting, Hund's J prefers to order the electrons by maximizing the total spin on the ion: thus in the case of two degenerate orbitals, the preferred configuration for two electrons would be the triplet, not the singlet. Hund's rule is a heuristic: if it was followed to the letter in this situation, it would actually "prefer" the configuration with truly maximum spin, namely $t_{2g}^5 e_g^2$, which has three unpaired spin up electrons and thus spin $S = \frac{3}{2}$. The magnitude of J essentially signifies how "strongly" the rule is followed: thus in this paper we do not consider very large values of J, as that would invalidate the two-band premise and we would have to include the full t_{2g} manifold into the calculation.

The last two terms are somewhat more exotic: they represent the simultaneous spin-flip and the pair hopping processes. Notice that we will make the spherically symmetric choice $U' = U - 2J$ and neglect the symmetry reduction due to crystal fields: this is standard procedure [60]. In this construction the values of U and J should still be thought of as phenomenological parameters, instead of the proper Coulomb atomic matrix elements.

2.4 Electron-lattice interaction

Now comes the crucial piece: an interaction between the electrons and the crystal lattice distortions. The collapsed or expanded octahedra should affect an electron's affinity to occupy a given site: coupling the electronic

density to the on-site distortion, we obtain the electron-phonon interaction term

$$\hat{H}_{e-latt} = -g \sum_i U_i \left(\hat{n}_i - 1\right). \tag{2.19}$$

Again applying the prescription $u_i = kU_i/g$, we obtain the final form

$$\hat{H}_{e-latt} = -2\epsilon_b \sum_i u_i(\hat{n}_i - 1). \tag{2.20}$$

Notice that in this picture the electron-lattice interactions are assumed the same for the two orbitals $|z\rangle, |\bar{z}\rangle$: this is because we assume that the only active lattice distortion mode is the breathing-mode, which interacts in the same way with both the orbitals. We thus implicitly assume that none of the other modes (like Jahn-Teller distortion) are active. We feel justified in this assumption given that there appears to be no experimental evidence of Jahn-Teller distortions, as discussed in the introduction in Ch. 1.

2.5 Final form of the Hamiltonian $\hat{H}$

Now that the stage is set and the model is fully defined, we have the following Hamiltonian for the rare-earth nickelates

$$\begin{aligned}\hat{H} = &\sum_{\mathbf{k}ab\sigma} t_{ab}(\mathbf{k}) d^\dagger_{\mathbf{k}a\sigma} d_{\mathbf{k}b\sigma} + \epsilon_b \sum_j \left(\frac{1}{2}u_j^2 + \frac{\alpha}{4}u_j^4\right) - 2\epsilon_b \sum_i u_i(\hat{n}_i - 1) + \\ &+ U \sum_{i\alpha} \hat{n}_{i\alpha\uparrow}\hat{n}_{i\alpha\downarrow} + U' \sum_{i\sigma} \hat{n}_{iz\sigma}\hat{n}_{i\bar{z}\bar{\sigma}} + (U' - J) \sum_{i\sigma} \hat{n}_{iz\sigma}\hat{n}_{i\bar{z}\sigma} - \\ &- J \sum_{i\sigma} d^\dagger_{iz\sigma} d_{iz\bar{\sigma}} d^\dagger_{i\bar{z}\bar{\sigma}} d_{i\bar{z}\sigma} + \gamma J \sum_{ia} d^\dagger_{ia\uparrow} d_{i\bar{a}\uparrow} d^\dagger_{ia\downarrow} d_{i\bar{a}\downarrow}.\end{aligned} \tag{2.21}$$

All in all there are 7 parameters characterizing this Hamiltonian: the three hoppings t_1, t_2, t_4, buried inside the coefficients $t_{ab}(\mathbf{k})$; the on-site Coulomb repulsion U and Hund's exchange J; the breathing-mode distortion energy ϵ_b and the dimensionless anharmonicity α.

Next, we perform a Hartree-Fock calculation on this Hamiltonian. One obvious difficulty we will face is that it is easiest to treat the hopping part in Fourier space, but it is simplest to treat the electron-electron (and electron-lattice) interactions in real space. Fortunately, there is a trick that can help us make use of both simplifications at once.

Chapter 3

Hartree-Fock Approximation for Rare-Earth Nickelates

> The most important part of doing physics is the skill to neglect.
>
> Lev Landau

We attack the Hamiltonian in 2.1 with the unrestricted Hartree-Fock approximation (*i.e.* the mean-field approach – in this thesis we will often use the terms interchangeably). It is unrestricted because we are allowing the spin occupancy to be independent of the orbital occupancy, and **not** demanding that for every occupied single-particle state that its spin-reversed partner is also occupied. The ground state wavefunction is assumed to split

$$|\Psi\rangle = |\Psi_e\rangle \otimes |\Phi_{latt}\{u\}\rangle\,, \tag{3.1}$$

with a Slater determinant $|\Psi_e\rangle$ for the electronic part and a semiclassical distortion $|\Phi_{latt}\{u\}\rangle$ for the lattice, which is a function of all the distortions $\{u_j\}$. The electronic part is complicated and will produce many mean-field parameters (*e.g.* charge disproportionation $\delta = \sum_{a\sigma}\langle n_{ia\sigma} - n_{i-1,a\sigma}\rangle$, orbital order $\sum_{\sigma}\langle n_{iz\sigma} - n_{i\bar{z}\sigma}\rangle$, spin density $\langle S_i\rangle$ and so on), while the lattice part only depends on the distortions u_j. To find the Hartree-Fock ground state, we will derive the self-consistency equations, obtained by minimizing the total energy

$$E = \langle\Psi|\,\hat{H}\,|\Psi\rangle\,, \tag{3.2}$$

with respect to the mean-field parameters.

3.1 Minimizing lattice contributions

First, we minimize the energy with respect to the lattice distortions u_i. In principle, a straightforward and foolproof approach is to compute the energy

as a function of u_i and do a simple (or not so simple) parameter sweep to find the lowest energy (and thus determine the ground state). However, this turns out to be an arduous and time-consuming process: luckily it is simplified significantly with the aid of the Hellmann-Feynman theorem [68, 69], which allows us to pass the derivative inside the expectation value during minimization

$$\frac{\partial}{\partial u_j} \langle \Phi_{latt}(u_i)| \langle \Psi_e| H |\Psi_e\rangle |\Phi_{latt}(u_i)\rangle = \tag{3.3}$$

$$= \langle \Phi_{latt}(u_i)| \langle \Psi_e| \frac{\partial H}{\partial u_j} |\Psi_e\rangle |\Phi_{latt}(u_i)\rangle , \tag{3.4}$$

despite the fact that $|\Psi_e\rangle |\Phi_{latt}(u_i)\rangle$ is generally not an eigenstate of $\hat{H}$ (as it needs to be for the usual proof [70] of the theorem to apply). In fact, there is a generalization of the theorem to any kind of variational state, not merely an eigenstate [71]. Consider the energy functional

$$E_T[\Psi\{u\}, \{u\}] = \langle \Psi\{u\}| \hat{H}\{u\} |\Psi\{u\}\rangle .$$

By definition, $|\Psi_e\rangle |\Phi_{latt}\{u\}\rangle$ is a stationary point of the functional with respect to a variation $\delta\Psi\{u\}$, i.e. $|\Psi_e\rangle |\Phi_{latt}\{u\}\rangle$ is the solution to

$$\frac{\delta E_T}{\delta \Psi\{u\}} = 0.$$

On the other hand, taking a total u derivative of E_T,

$$\frac{d}{du} E_T(\Psi\{u\}, \{u\}) = \frac{\partial E_T}{\partial\{u\}} + \frac{\delta E_T}{\delta\Psi\{u\}} \frac{\partial \Psi\{u\}}{\partial\{u\}} = \frac{\partial E_T}{\partial\{u\}},$$

we see that the Hellman-Feynman result still holds, thanks to the stationarity of the variational state. (In our calculation, we also checked this numerically, by comparing the results of Hellmann-Feynman calculation with explicit minimization with respect to u.)

Utilizing the Hellmann-Feynman theorem, we minimize with respect to u_i

$$\sum_i \langle \Psi_e| \langle \Phi| \frac{\partial}{\partial u_j} 2\epsilon_b \left(\frac{1}{2} u_i^2 + \frac{a}{4} u_i^4 - u_i (\hat{n}_i - 1) \right) |\Phi\rangle |\Psi_e\rangle =$$

$$= 2\epsilon_b [u_j + a u_j^3 - \langle \hat{n}_j \rangle_{\Psi_e} - 1] = 0,$$

where we defined $\langle\Psi_e|\,\hat{O}\,|\Psi_e\rangle \equiv \langle\hat{O}\rangle_{\Psi_e}$. This gives us our first self-consistency equation

$$u_j + au_j^3 + 1 = \langle n_j\rangle_{\Psi_e}. \tag{3.5}$$

Careful neutron scattering measurements from multiple groups suggest that the lattice distortions are isotropic, and alternate between the octahedra along all three crystallographic axes. Moreover, the collapse magnitude u of one octahedra is exactly equal to the expansion of another. Therefore we adopt the ansatz $u_j = ue^{i\mathbf{Q}_c\cdot\mathbf{R}_j}$, where $\mathbf{Q}_c = (2\pi/a)(\frac{1}{2},\frac{1}{2},\frac{1}{2})$ is the ordering wavevector corresponding to a breathing-mode distortion. Let us also choose to represent the charge disproportionation behaviour with a parameter δ, so that $\langle\hat{n}_j\rangle = 1 + \delta e^{i\mathbf{Q}_c\cdot\mathbf{R}_j}$ (charge disproportionation follows the same ordering wavevector as the lattice distortion — this will be discussed in much more detail in Sec. 3.3). The equation above then reduces to a depressed cubic equation

$$u + au^3 = \delta, \tag{3.6}$$

which, interestingly, admits a closed-form solution (see Appendix B for details):

$$u = \delta\frac{3}{2\beta^{\frac{1}{3}}}\left[(1+\sqrt{1+\frac{1}{\beta}})^{\frac{1}{3}} + (1-\sqrt{1+\frac{1}{\beta}})^{\frac{1}{3}}\right], \tag{3.7}$$

with $\beta = \frac{27}{4}a\delta^2$. In other words, in our model the lattice distortion is inherently linked to charge disproportionation, just as observed in experiments (of course, this was already clear in the general Eq. 3.5, before any assumptions about the specific type of lattice/charge order). This is helpful: it allows us to eliminate any u dependence in the Hartree-Fock equations, leaving only dependence on the electronic mean-fields and thus reducing the problem to a purely electronic one.

It is important to note that whilst the argument above establishes the validity of a Hellman-Feynman like result for any variational stationary state of the energy functional, in reality there can be small discrepancies arising due to round-off and other errors inherent to any numerical implementation of the calculation [71]. The "stationary state" thus obtained will not be exactly the true stationary state and thus in principle the theorem does not apply. However, assuming the errors can be made sufficiently small, the theorem should still apply within the error margins: and our calculations confirm this, showing that there is no difference (other than speed) between relying on this extended Hellmann-Feynman result and doing the foolproof parameter sweep.

3.2 Minimizing electronic contributions

We now derive the self-consistency equations for the electronic degrees of freedom. Assume, as usual in the unrestricted Hartree-Fock approximation [72], that the true ground state is a Slater determinant of some (so far unknown) states with creation operators $a_p^\dagger$

$$|\Psi_e\rangle = \prod_p a_p^\dagger |0\rangle , \tag{3.8}$$

with the new states being related to the original $d_{ia\sigma}^\dagger$ by a unitary transformation

$$d_{ia\sigma}^\dagger = \sum_n \phi_n^*(ia\sigma) a_n^\dagger. \tag{3.9}$$

This is the first assumption of mean-field (or Hartree-Fock) theory. The goal is to determine this unitary transformation, by calculating the energy in this state and subsequently minimizing it with respect to the variational (mean-field) parameters $\phi_n(ia\sigma)$ (equivalently, expectation values $\langle d_{ia\sigma}^\dagger d_{jb\tau}\rangle_{\Psi_e}$).

The H_{latt} term has no electron operators and vanishes during minimization. The electron-phonon term $\hat{H}_{e-latt}$ immediately yields

$$\begin{aligned}\langle\Psi_e|\, \hat{H}_{e-latt}\, |\Psi_e\rangle &= \langle\Psi_e| - 2\epsilon_b \sum_i u_i(\hat{n}_i - 1)\, |\Psi_e\rangle = \\ &= -2\epsilon_b \sum_i u_i \left[\sum_{pa\sigma} \phi_p^*(ia\sigma)\phi_p(ia\sigma) - 1\right].\end{aligned} \tag{3.10}$$

The hopping term $\hat{T}$ produces, in real space

$$\langle\hat{T}\rangle_{\Psi_e} = \sum_p \sum_{ijab\sigma} t_{ij}^{ab} \phi_p^*(ia\sigma)\phi_p(jb\sigma). \tag{3.11}$$

Finally, consider the Kanamori interaction operator $\hat{H}_e$. As this is a four-operator interaction and the state $|\Psi_e\rangle$ is a Slater determinant, to evaluate the expectation value we can use Wick's theorem [73]. In short, it says that whenever we have an expectation value with respect to a Slater determinant of an even number of creation/annihilation operators (say $\langle d_\uparrow^\dagger d_\uparrow d_\downarrow^\dagger d_\downarrow\rangle$), the result is a sum of products of all possible pairwise expectation values (called contractions), with the sign reflecting the number of permutations of the operators that are required to attain that given order (so

$\langle d^\dagger_\uparrow d_\uparrow d^\dagger_\downarrow d_\downarrow\rangle = \langle d^\dagger_\uparrow d_\uparrow\rangle\langle d^\dagger_\downarrow d_\downarrow\rangle - \langle d^\dagger_\uparrow d_\downarrow\rangle\langle d^\dagger_\downarrow d_\uparrow\rangle)$. In principle even contractions like $\langle d^\dagger_\uparrow d^\dagger_\downarrow\rangle$ could be allowed for a state more complex than a Slater determinant: this expectation value would be nonzero if the ground state against which this expectation value was taken would allow two-electron excitations (for example, this expectation value would be nonzero for the BCS state, if we were trying to construct a model for superconductivity [74]). In our case, since we assume a normal state for the electrons, we automatically drop such terms from the Wick expansion. Using this technique on the Kanamori Hamiltonian immediately leads to

$$\begin{aligned}\langle \hat{H}_e\rangle_{\Psi_e} =& U\sum_{ia}\left[\langle d^\dagger_{ia\uparrow}d_{ia\uparrow}\rangle\langle d^\dagger_{ia\downarrow}d_{ia\downarrow}\rangle - \langle d^\dagger_{ia\uparrow}d_{ia\downarrow}\rangle\langle d^\dagger_{ia\downarrow}d_{ia\uparrow}\rangle\rangle\right] + \\ &+ U'\sum_{i\sigma}\left[\langle d^\dagger_{iz\sigma}d_{iz\sigma}\rangle\langle d^\dagger_{i\bar{z}\bar{\sigma}}d_{i\bar{z}\bar{\sigma}}\rangle - \langle d^\dagger_{iz\sigma}d_{i\bar{z}\bar{\sigma}}\rangle\langle d^\dagger_{i\bar{z}\bar{\sigma}}d_{iz\sigma}\rangle\right] + \\ &+ (U'-J)\sum_{i\sigma}\left[\langle d^\dagger_{iz\sigma}d_{iz\sigma}\rangle\langle d^\dagger_{i\bar{z}\sigma}d_{i\bar{z}\sigma}\rangle - \langle d^\dagger_{iz\sigma}d_{i\bar{z}\sigma}\rangle\langle d^\dagger_{i\bar{z}\sigma}d_{iz\sigma}\rangle\right] - \\ &- J\sum_{i\sigma}\left[\langle d^\dagger_{iz\sigma}d_{iz\bar{\sigma}}\rangle\langle d^\dagger_{i\bar{z}\bar{\sigma}}d_{i\bar{z}\sigma}\rangle - \langle d^\dagger_{iz\sigma}d_{i\bar{z}\sigma}\rangle\langle d^\dagger_{i\bar{z}\bar{\sigma}}d_{iz\bar{\sigma}}\rangle\right] + \\ &+ \gamma J\sum_{ia}\left[\langle d^\dagger_{ia\uparrow}d_{i\bar{a}\uparrow}\rangle\langle d^\dagger_{ia\downarrow}d_{i\bar{a}\downarrow}\rangle - \langle d^\dagger_{ia\uparrow}d_{i\bar{a}\downarrow}\rangle\langle d^\dagger_{ia\downarrow}d_{i\bar{a}\uparrow}\rangle\right]. \end{aligned} \tag{3.12}$$

Since all interactions are on-site, there will be no matrix elements $\langle d^\dagger_{ia\sigma}d_{jb\tau}\rangle$ for $i \neq j$. With this, the full set of unrestricted Hartree-Fock equations may be obtained by varying the energy $E = \langle \hat{T} + \hat{H}_e + H_{latt} + \hat{H}_{e-latt}\rangle$ with respect to the amplitudes $\phi^*_p(ia\sigma)$, together with the constraint that the set $\phi_p(ia\sigma)$ are normalized amplitudes. Mathematically, that last part means $1 = \sum_{ia\sigma}\phi^*_p(ia\sigma)\phi_p(ia\sigma)$ for all p. This constraint can be accomplished by what is essentially a Lagrange multiplier technique: simply add the (constant) term $\sum_{lia\sigma} E_l\phi^*_l(ia\sigma)\phi_l(ia\sigma)$ to the Hamiltonian,

$$\tilde{H} = \hat{H} - \sum_{lia\sigma} E_l\phi^*_l(ia\sigma)\phi_l(ia\sigma), \tag{3.13}$$

where E_l is the Lagrange multiplier, one for every set of amplitudes ϕ_l (and, simultaneously, the Hartree-Fock energy of that state). The normalization condition of ϕ can be recovered from the total expression in the usual way – by differentiating with respect to the Lagrange multiplier and setting the result equal to zero

$$\frac{\partial}{\partial E_p}\tilde{H} = 1 - \sum_{ia\sigma}\phi^*_p(ia\sigma)\phi_p(ia\sigma) = 0.$$

At the same time, varying $\tilde{H}$ with respect to the amplitudes ϕ gives the equations which determine these amplitudes, subject to the constraint that they are normalized:

$$E_p\phi_p(ia\sigma) = \frac{\delta}{\delta\phi_p^*(ia\sigma)}\langle\hat{H}\rangle. \tag{3.14}$$

These are the celebrated Hartree-Fock equations. We derive them step by step.

First, noticing that $\langle d^\dagger_{ia\sigma}d_{jb\sigma'}\rangle = \sum_p \phi_p^*(ia\sigma)\phi_p(jb\sigma')$, a key identity may be obtained that simplifies the variation considerably (especially for the Kanamori term)

$$\frac{\delta}{\delta\phi_p^*(lc\tau)}\sum_{ijab\sigma\sigma'}\langle d^\dagger_{ia\sigma}d_{jb\sigma'}\rangle = \sum_{ijab\sigma\sigma'}\delta_{lc\tau,ia\sigma}\phi_p(jb\sigma'), \tag{3.15}$$

where $\delta_{lc\tau,ia\sigma}$ is the Kronecker delta function which is zero unless $l=i, c=a, \tau=\sigma$, in which case it is 1. Using this identity, we calculate the variation term by term. Varying the hopping term we immediately obtain

$$\frac{\delta}{\delta\phi_p^*(ia\sigma)}\Big(\sum_s\sum_{ljcb\tau}t_{lj}^{cb}\phi_s^*(lc\tau)\phi_s(jb\tau)\Big) = \sum_{jb}t_{ij}^{ab}\phi_p(jb\sigma). \tag{3.16}$$

Varying the E_{e-latt},

$$\frac{\delta}{\delta\phi_p^*(ia\sigma)}\Big(-2\epsilon_b\sum_j u_j\left[\sum_{lb\tau}\phi_l^*(jb\tau)\phi_l(jb\tau)-1\right]\Big) = -2\epsilon_b u_i\phi_p(ia\sigma). \tag{3.17}$$

Finally, tackle varying the Kanamori contribution, term by term, using the identity 3.15:

$$\begin{aligned}
&\text{first term of } \langle\hat{H}\rangle \to \frac{\delta}{\delta\phi_p^*(ia\sigma)}\Big(U\sum_{jb}\Big[\langle d^\dagger_{jb\uparrow}d_{jb\uparrow}\rangle\langle d^\dagger_{jb\downarrow}d_{jb\downarrow}\rangle - \langle d^\dagger_{jb\uparrow}d_{jb\downarrow}\rangle\times\\
&\times\langle d^\dagger_{jb\downarrow}d_{jb\uparrow}\rangle\Big]\Big) = U(\phi_p(ia\uparrow)\delta_{\sigma,\uparrow}\langle d^\dagger_{ia\downarrow}d_{ia\downarrow}\rangle + \phi_p(ia\downarrow)\delta_{\sigma,\downarrow}\langle d^\dagger_{ia\uparrow}d_{ia\uparrow}\rangle -\\
&-\phi_p(ia\downarrow)\delta_{\sigma,\uparrow}\langle d^\dagger_{ia\downarrow}d_{ia\uparrow}\rangle - \phi_p(ia\uparrow)\delta_{\sigma,\downarrow}\langle d^\dagger_{ia\uparrow}d_{ia\downarrow}\rangle) =\\
&= U(\phi_p(ia\sigma)\langle d^\dagger_{ia\bar{\sigma}}d_{ia\bar{\sigma}}\rangle - \phi_p(ia\bar{\sigma})\langle d^\dagger_{ia\bar{\sigma}}d_{ia\sigma}\rangle).
\end{aligned} \tag{3.18}$$

In the last line we made the replacements of the type $\phi_p(ia\uparrow)\delta_{\sigma,\uparrow}\langle d^\dagger_{ia\downarrow}d_{ia\downarrow}\rangle \to \phi_p(ia\sigma)\langle d^\dagger_{ia\bar{\sigma}}d_{ia\bar{\sigma}}\rangle$. These are valid because only one of every pair of terms

in the second line is nonzero for a given σ: and for that nonzero term, the spins can be deduced relative to the original spin σ.

Using the same tricks, the variations of the other terms can be evaluated:

$$\text{second term of } \langle\hat{H}\rangle \to \frac{\delta}{\delta\phi_p^*(ia\sigma)}\Big(U'\sum_{j\sigma'}\Big[\langle d^\dagger_{jz\sigma'}d_{jz\sigma'}\rangle\langle d^\dagger_{j\bar{z}\bar{\sigma}'}d_{j\bar{z}\bar{\sigma}'}\rangle - \\ - \langle d^\dagger_{jz\sigma'}d_{j\bar{z}\bar{\sigma}'}\rangle\langle d^\dagger_{j\bar{z}\bar{\sigma}'}d_{jz\sigma'}\rangle\Big]\Big) = U'(\phi_p(ia\sigma)\langle d^\dagger_{i\bar{a}\bar{\sigma}}d_{i\bar{a}\bar{\sigma}}\rangle - \phi_p(i\bar{a}\bar{\sigma})\langle d^\dagger_{i\bar{a}\bar{\sigma}}d_{ia\sigma}\rangle), \tag{3.19}$$

$$\text{third term of } \langle\hat{H}\rangle \to \frac{\delta}{\delta\phi_p^*(ia\sigma)}\Big((U'-J)\sum_{j\sigma'}\Big[\langle d^\dagger_{jz\sigma'}d_{jz\sigma'}\rangle\langle d^\dagger_{j\bar{z}\sigma'}d_{i\bar{z}\sigma}\rangle - \\ - \langle d^\dagger_{iz\sigma}d_{i\bar{z}\sigma}\rangle\langle d^\dagger_{j\bar{z}\sigma'}d_{jz\sigma'}\rangle\Big]\Big) = (U'-J)(\phi_p(ia\sigma)\langle d^\dagger_{i\bar{a}\sigma}d_{i\bar{a}\sigma}\rangle - \\ - \phi_p(i\bar{a}\sigma)\langle d^\dagger_{i\bar{a}\sigma}d_{ia\sigma}\rangle). \tag{3.20}$$

The simultaneous spin-flip term results in

$$\text{fourth term of } \langle\hat{H}\rangle \to \frac{\delta}{\delta\phi_p^*(ia\sigma)}\Big(-J\sum_{j\sigma'}\Big[\langle d^\dagger_{jz\sigma'}d_{jz\bar{\sigma}'}\rangle\langle d^\dagger_{j\bar{z}\bar{\sigma}'}d_{j\bar{z}\sigma'}\rangle - \\ - \langle d^\dagger_{jz\sigma'}d_{j\bar{z}\sigma'}\rangle\langle d^\dagger_{j\bar{z}\bar{\sigma}'}d_{jz\bar{\sigma}'}\rangle\Big]\Big) = -J(\phi_p(ia\bar{\sigma})\langle d^\dagger_{i\bar{a}\bar{\sigma}}d_{i\bar{a}\sigma}\rangle - \phi_p(i\bar{a}\sigma)\langle d^\dagger_{i\bar{a}\bar{\sigma}}d_{ia\bar{\sigma}}\rangle). \tag{3.21}$$

Finally, the pair-hopping process gives

$$\text{fifth term of } \langle\hat{H}\rangle \to \frac{\delta}{\delta\phi_p^*(ia\sigma)}\Big(\gamma J\sum_{jb}\Big[\langle d^\dagger_{jb\uparrow}d_{j\bar{b}\uparrow}\rangle\langle d^\dagger_{jb\downarrow}d_{j\bar{b}\downarrow}\rangle - \\ - \langle d^\dagger_{jb\uparrow}d_{j\bar{b}\downarrow}\rangle\langle d^\dagger_{jb\downarrow}d_{j\bar{b}\uparrow}\rangle\Big]\Big) = \gamma J(\phi_p(i\bar{a}\sigma)\langle d^\dagger_{ia\bar{\sigma}}d_{i\bar{a}\bar{\sigma}}\rangle - \phi_p(i\bar{a}\bar{\sigma})\langle d^\dagger_{ia\bar{\sigma}}d_{i\bar{a}\sigma}\rangle). \tag{3.22}$$

Combining these variations, we obtain the Hartree-Fock equations

$$\begin{aligned} E_p\phi_p(ia\sigma) = &\sum_{jb} t_{ij}^{ab}\phi_p(jb\sigma) + \Big[-2\epsilon_b u_i + U\langle d^\dagger_{ia\bar\sigma} d_{ia\bar\sigma}\rangle + U'\langle d^\dagger_{i\bar a\bar\sigma} d_{i\bar a\bar\sigma}\rangle + \\ &+ (U'-J)\langle d^\dagger_{i\bar a\sigma} d_{i\bar a\sigma}\rangle\Big]\phi_p(ia\sigma) + \Big[-U\langle d^\dagger_{ia\bar\sigma} d_{ia\sigma}\rangle - \\ &- J\langle d^\dagger_{i\bar a\bar\sigma} d_{i\bar a\sigma}\rangle\Big]\phi_p(ia\bar\sigma) + \Big[(U'-J)\langle d^\dagger_{i\bar a\sigma} d_{ia\sigma}\rangle + \\ &+ J\langle d^\dagger_{i\bar a\bar\sigma} d_{ia\bar\sigma}\rangle + \gamma J\langle d^\dagger_{ia\bar\sigma} d_{i\bar a\bar\sigma}\rangle\Big]\phi_p(i\bar a\sigma) + \\ &+ \Big[U'\langle d^\dagger_{i\bar a\bar\sigma} d_{ia\sigma}\rangle + \gamma J\langle d^\dagger_{ia\bar\sigma} d_{i\bar a\sigma}\rangle\Big]\phi_p(i\bar a\bar\sigma). \end{aligned} \tag{3.23}$$

This is clearly a nonlinear eigenvalue problem, as we have terms of order ϕ and of order ϕ^3 on the right-hand side of the equation. The easiest (and often only) way to solve it is by iteration. Given an initial guess for the mean-field parameters $\mathbf{w}^{(0)} = \{\langle d^\dagger_{ia\sigma} d_{ib\tau}\rangle\}$, this set of equations can be solved for the Hartree-Fock energies E_p and the amplitudes (eigenstates) $\phi_p(ia\sigma)$. In turn, the energies can be used to determine which "states" $\phi_p(ia\sigma)$ are occupied (remember that since our calculation is done at zero energy, there is a well-defined Fermi level). At zero energy this is determined by filling: in our case, there is one electron per Ni site, which corresponds to quarter-filling (2 orbitals and 2 spins per orbital = 4 states, 1 electron). The bottom quarter of all the states is then considered occupied: from these occupied states, the mean-field parameters $\mathbf{v}^{(0)} = \{\langle d^\dagger_{ia\sigma} d_{ib\tau}\rangle'\}$ can be re-calculated and compared to the initial guesses for these parameters. If the two do not agree (to within some pre-specified margin of error), the newly calculated parameters become guesses for the next iteration step, $\mathbf{w}^{(1)} = \mathbf{v}^0$. This process is then repeated until convergence.

3.3 Mean-Field Parameters

Of course, the (infinite-dimensional) set of mean-field parameters $\langle d^\dagger_{ia\sigma} d_{ib\tau}\rangle$ is too general and needs to be specialized to the problem at hand. This is where the second mean-field assumption comes in: we will assume that the set of relevant parameters can be truncated past a particular value of i. Specifically, we assume that only the parameters within a periodically repeating unit cell are non-trivial. The particular choice of this periodic structure is motivated by phase phenomena experimentally found in rare-earth nickelates: charge disproportionation, (potential for) orbital order,

and the various magnetic possibilities, from ferromagnetism to exotic non-collinear 4-site orders. Given the ordering wavevectors for these behaviours ($\mathbf{Q}_c$ and $\mathbf{Q}_m$, respectively), we conclude that (one choice for) the unit cell is a 4-site linearly-coordinated one. Thus only mean-field parameters from $i = (i, j, k)$ to $i + 4\hat{x} = (i + 4, j, k)$ should matter: the rest of the mean-field parameters can be obtained by translation of the unit cell by the primitive lattice vectors.

However, it is not clear *a priori* what starting guesses for the mean-field parameters $\langle d^\dagger_{ia\sigma} d_{ib\tau} \rangle$ are appropriate: we do not have any intuition as to what values of these matrix elements would correspond to particular kinds of actual charge/lattice/magnetic orders. Instead, it would be useful if we had some combinations of these mean-fields (let us call the combinations **order parameters**), which would readily signal the presence or absence of a particular order.

Consider, for example, the phenomenon of charge order, with a 3D checkerboard pattern represented by the ordering wavevector

$$\mathbf{Q}_c = \frac{2\pi}{a}\left(\frac{1}{2}, \frac{1}{2}, \frac{1}{2}\right).$$

The average charge at site i is $\langle \hat{n}_i \rangle = \sum_{a\sigma} \langle d^\dagger_{ia\sigma} d_{ia\sigma} \rangle$: suppose there is a difference δ between neighbouring sites in all three crystallographic directions, namely

$$\langle \hat{n}_{(i,j,k)} \rangle - \langle \hat{n}_{(i,j,k)+\eta} \rangle = \delta, \quad \eta \in \{\hat{x}, \hat{y}, \hat{z}\}. \tag{3.24}$$

A shorthand way of writing this is by using the ordering wavevector: set

$$\langle \hat{n}_i \rangle = 1 + \delta e^{i\mathbf{Q}_c \cdot \mathbf{R}_i} = 1 + \delta e^{i\pi(i+j+k)}, \quad \mathbf{Q}_c = \frac{2\pi}{a}\left(\frac{1}{2}, \frac{1}{2}, \frac{1}{2}\right). \tag{3.25}$$

It is clear from this expression that on each alternate site along the three crystallographic axes, the magnitude of the on-site charge will be either enhanced (if the integer in the exponent is even) or reduced (if it is odd) by the same factor of δ. Thus a $\delta \neq 0$ readily indicates the presence of (rocksalt-type) charge order. On the other hand, as we just said above, the on-site average electron density is the sum of the densities in the respective orbital and spin states

$$\langle \hat{n}_i \rangle = \sum_{a\sigma} \langle d^\dagger_{ia\sigma} d_{ia\sigma} \rangle. \tag{3.26}$$

So one order parameter δ wraps into itself a variety of different matrix elements $\langle d^\dagger_{ia\sigma} d_{ib\tau}\rangle$, while simultaneously being a signature of a given phase: it then appears more prudent to search for such order parameters than to randomly guess values for the

$$[\times 2(\text{orbitals})\times 2(\text{spins})](\text{states}) \text{ choose } 2 \text{ (each matrix element includes two states)} \to 6 \xrightarrow{\text{times 4, as there are 4 unique sites}} 24$$

different allowed matrix elements.

Given that no experimental signatures of orbital order have been observed to date in the nickelates, a reasonable assumption to make is that at least the average occupancy of the **original** orbitals $|z\rangle, |\bar{z}\rangle$ is the same,

$$\langle \hat{n}_{iz}\rangle = \langle \hat{n}_{i\bar{z}}\rangle. \tag{3.27}$$

This does not entirely preclude the possibility of orbital order, which could still occur due to nonzero cross-orbital matrix elements $\langle d^\dagger_{ia\sigma} d_{i\bar{a}\tau}\rangle$. (Much like the cross-spin matrix elements $\langle d^\dagger_{ia\sigma} d_{ib\bar{\sigma}}\rangle$ correspond to spin order off-the-axis, namely along the x or y axis instead of the z, cross-orbital matrix elements would result in orbital order across some combination of the orbital orbitals $|z\rangle, |\bar{z}\rangle$.) Combined with the expression that defined δ in eq: 3.26, the assumption of equal *a priori* orbital occupancy means

$$\langle d^\dagger_{ia\uparrow} d_{ia\uparrow}\rangle + \langle d^\dagger_{ia\downarrow} d_{ia\downarrow}\rangle = \frac{1}{2}\left[1 + \delta e^{i\mathbf{Q}_c\cdot\mathbf{R}_i}\right]. \tag{3.28}$$

To proceed further, we need to consider the average spin on site i, $\langle \mathbf{S}_i\rangle = \sum_{a\tau\tau'} \langle d^\dagger_{ia\tau} \frac{\boldsymbol{\sigma}_{\tau\tau'}}{2} d_{ia\tau'}\rangle$ ($\boldsymbol{\sigma}_{\tau\tau'}$ is the vector of Pauli matrices). Applying the same sort of thinking, we write down an ansatz for the average spin per site based on the possible magnetic orders

$$\langle \mathbf{S}_i\rangle = S_{\text{FM}}\hat{z} + S_{\text{AFM}} e^{i\mathbf{Q}_c\cdot\mathbf{R}_i}\hat{z} + \mathbf{S}_1\cos(\mathbf{Q}_m\cdot\mathbf{R}_i) + \mathbf{S}_2\sin(\mathbf{Q}_m\cdot\mathbf{R}_i). \tag{3.29}$$

The ferromagnetic and antiferromagnetic orders should be self-explanatory. The last two terms are the ones that produce the possibility of a 4-site magnetic order: this is because the "period" of the cosine or a sine with the wavevector $\mathbf{Q}_m$ is going to be 4 sites. For instance, a cosine will evaluate to 0, then 1, then 0, then -1: supposing that $\mathbf{S}_1 = (0, 0, S_{1z})$, the resulting magnetic pattern would be $\uparrow\ 0\ \downarrow\ 0$, precisely one of the contenders for the ground state suggested in the literature. The sine term, on the other hand, is offset by one lattice site: an equivalent setup for the sine term would

result in the magnetic pattern being $0 \uparrow 0 \downarrow$. Thus when put together, they can produce another candidate, $\uparrow\uparrow\downarrow\downarrow$. Finally, picking $\mathbf{S}_1 = (0, 0, S_{1z})$ and $\mathbf{S}_2 = (S_{2x}, 0, 0)$ would produce the non-collinear order $\uparrow\rightarrow\downarrow\leftarrow$.

Once again we will resort to experiment and assume equal orbital occupation of the original orbitals $|z\rangle, |\bar{z}\rangle$. We also assume that the magnetic order vectors $\mathbf{S}_{1/2} = (S_{1/2x}, 0, S_{1/2z})$ can only have nonzero x and z components, so that there are only two independent axes involved in the noncollinear order. Unpacking the expression for the average spin density in terms of Pauli matrices $\langle \mathbf{S}_i \rangle = \sum_{a\tau\tau'} \langle d^\dagger_{ia\tau} \frac{\boldsymbol{\sigma}_{\tau\tau'}}{2} d_{ia\tau'} \rangle$ for the particular axes we find

$$\frac{1}{2}\left[\langle d^\dagger_{ia\uparrow} d_{ia\uparrow}\rangle - \langle d^\dagger_{ia\downarrow} d_{ia\downarrow}\rangle\right] = \frac{1}{2}\Big[S_{\mathrm{FM}} + S_{\mathrm{AFM}} e^{i\mathbf{Q}_c\cdot\mathbf{R}_i} + \\ + S_{1z}\cos(\mathbf{Q}_m\cdot\mathbf{R}_i) + S_{2z}\sin(\mathbf{Q}_m\cdot\mathbf{R}_i)\Big], \tag{3.30}$$

$$\frac{1}{2}\left[\langle d^\dagger_{ia\uparrow} d_{ia\downarrow}\rangle + \langle d^\dagger_{ia\downarrow} d_{ia\uparrow}\rangle\right] = \frac{1}{2}\left[S_{1x}\cos(\mathbf{Q}_m\cdot\mathbf{R}_i) + S_{2x}\sin(\mathbf{Q}_m\cdot\mathbf{R}_i)\right]. \tag{3.31}$$

The y axis calculation yields an identity

$$-\frac{i}{2}\left[\langle d^\dagger_{ia\uparrow} d_{ia\downarrow}\rangle - \langle d^\dagger_{ia\downarrow} d_{ia\uparrow}\rangle\right] = 0, \tag{3.32}$$

due to our assumption of only 2 independent non-collinear axes. Thus $\langle d^\dagger_{ia\uparrow} d_{ia\downarrow}\rangle = \langle d^\dagger_{ia\downarrow} d_{ia\uparrow}\rangle$. Combining these results with the previous insights about δ, we can write a general form for the direct and cross-spin matrix elements $\langle d^\dagger_{ia\sigma} d_{ia\sigma}\rangle, \langle d^\dagger_{ia\sigma} d_{ia\bar{\sigma}}\rangle$, with both spin-dependent and spin-independent parts, as follows

$$\langle d^\dagger_{ia\sigma} d^\dagger_{ia\sigma}\rangle = \frac{1}{4}\left[1 + \delta e^{i\mathbf{Q}_c\cdot\mathbf{R}_i}\right] + \frac{\sigma}{2}\Big[S_{\mathrm{FM}} + S_{\mathrm{AFM}} e^{i\mathbf{Q}_c\cdot\mathbf{R}_i} + \\ + S_{1z}\cos(\mathbf{Q}_m\cdot\mathbf{R}_i) + S_{2z}\sin(\mathbf{Q}_m\cdot\mathbf{R}_i)\Big], \tag{3.33}$$

$$\langle d^\dagger_{ia\sigma} d^\dagger_{ia\bar{\sigma}}\rangle = \frac{1}{2}\left[S_{1x}\cos(\mathbf{Q}_m\cdot\mathbf{R}_i) + S_{2x}\sin(\mathbf{Q}_m\cdot\mathbf{R}_i)\right]. \tag{3.34}$$

In a very similar manner, directly by analogy we establish the mean-field order parameters for the orbital order, that arises from the cross-orbital

matrix elements $\langle d^\dagger_{ia\sigma} d^\dagger_{i\bar{a}\sigma}\rangle$. Altogether, we have the following definitions

$$\begin{aligned}
\langle d^\dagger_{ia\sigma} d^\dagger_{ia\sigma}\rangle =& \frac{1}{4}\left[1+\delta e^{i\mathbf{Q}_c\cdot\mathbf{R}_i}\right] + \frac{\sigma}{2}\Big[S_{\mathrm{FM}} + S_{\mathrm{AFM}} e^{i\mathbf{Q}_c\cdot\mathbf{R}_i} + \\
&+ S_{1\mathrm{z}}\cos(\mathbf{Q}_m\cdot\mathbf{R}_i) + S_{2\mathrm{z}}\sin(\mathbf{Q}_m\cdot\mathbf{R}_i)\Big], \\
\langle d^\dagger_{ia\sigma} d^\dagger_{ia\bar{\sigma}}\rangle =& \frac{1}{2}\left[S_{1\mathrm{x}}\cos(\mathbf{Q}_m\cdot\mathbf{R}_i) + S_{2\mathrm{x}}\sin(\mathbf{Q}_m\cdot\mathbf{R}_i)\right], \\
\langle d^\dagger_{ia\sigma} d^\dagger_{i\bar{a}\sigma}\rangle =& O_1 + O_2 e^{i\mathbf{Q}_c\cdot\mathbf{R}_i} + \sigma\Big[Z_1 + Z_2 e^{i\mathbf{Q}_c\cdot\mathbf{R}_i} + \\
&+ Z_3\cos(\mathbf{Q}_m\cdot\mathbf{R}_i) + Z_4\sin(\mathbf{Q}_m\cdot\mathbf{R}_i)\Big], \\
\langle d^\dagger_{ia\sigma} d^\dagger_{i\bar{a}\bar{\sigma}}\rangle =& X_1\cos(\mathbf{Q}_m\cdot\mathbf{R}_i) + X_2\sin(\mathbf{Q}_m\cdot\mathbf{R}_i).
\end{aligned} \tag{3.35}$$

The parameters thus defined transparently allow for the presence of different kinds of ordering. For instance, if $S_{\mathrm{AFM}} = 1$ and the other S are identically zero, that corresponds directly to antiferromagnetic ordering

$$\begin{aligned}
&\langle S^z_i\rangle = \sum_a \langle d^\dagger_{ia\uparrow} d_{ia\uparrow} - d^\dagger_{ia\downarrow} d_{ia\downarrow}\rangle = S_{\mathrm{FM}} + S_{\mathrm{AFM}} e^{i\mathbf{Q}_c\cdot\mathbf{R}_i} + \\
&+ S_{1\mathrm{z}}\cos(\mathbf{Q}_m\cdot\mathbf{R}_i) + S_{2\mathrm{z}}\sin(\mathbf{Q}_m\cdot\mathbf{R}_i) = S_{\mathrm{AFM}} e^{i\mathbf{Q}_c\cdot\mathbf{R}_i} \sim S_{\mathrm{AFM}}(\uparrow\downarrow\uparrow\downarrow).
\end{aligned}$$

In the last line, and throughout this thesis we frequently use this arrow notation to refer to the magnetic order that obtains in the lattice, by simply writing down the arrows for the spin alignment within a single 4-site linearly-coordinated unit cell. Notice that there are only 15 free parameters here (16 when counting the lattice distortion u, which however is fixed by δ), as opposed to the 24 matrix elements we started with: this is due to the assumptions we made when defining the possible order parameters based on what could be expected to be seen from experiment.

The various suggested guesses for the magnetic order can be obtained as follows: the $\Uparrow 0 \Downarrow 0$ obtains if $\delta > 0$ and $S_{1z} > 0$, while all others are zero. The sublattice-symmetric collinear order $\uparrow\uparrow\downarrow\downarrow$ obtains if $S_{1z} = S_{2z} \neq 0$. Finally, a non-collinear state $\uparrow\rightarrow\downarrow\leftarrow$ can be obtained if $S_{1z} = S_{2x} \neq 0$.

3.4 Energy of the Hartree-Fock ground state

In general, multiple solutions can be found to 3.23 for any given set of parameters t_1, t_2, t_4, U, J *etc.*. To identify the true ground state, it is necessary to calculate the total energy of each of the solutions, then pick the state with the lowest energy. As the Hartree-Fock approximation is a variational

approximation, such a solution will be an upper-bound on the true ground state energy of the model. The ground state energy per site of a trial state $|\Psi_e\rangle$ is given by

$$\frac{E_{GS}}{N} = \frac{1}{N} \langle \Psi_e | \hat{T} + \hat{H}_e + \hat{H}_{e-latt} + H_{latt} | \Psi_e \rangle . \tag{3.36}$$

It is immediately clear that there is a problem[10]. The definitions of the order parameters $\mathbf{w} = \delta, S_{\mathrm{FM}}, ...$ rely on the single-site (localized) matrix elements $\langle d^\dagger_{ia\sigma} d_{ib\tau} \rangle$: thus it is best to evaluate the interaction contribution to the energy $\langle \hat{H}_e + \hat{H}_{e-latt} \rangle$ in the localized, site-centered single-particle basis $|ia\sigma\rangle$. Meanwhile the hopping energy $\langle \hat{T} \rangle$ is best expressed in the extended Bloch state basis $|\mathbf{k}a\sigma\rangle = \sum_i \frac{e^{i\mathbf{k}\cdot\mathbf{R}_i}}{\sqrt{N}} |ia\sigma\rangle$. To circumvent the need to convert either of the energy contributions to a cumbersome representation, we resort to a trick that allows us to re-express the hopping average $\langle \hat{T} \rangle$ in terms of the Hartree-Fock energies E_p and thus eliminate it from the energy expression entirely. Multiplying on the left by $\phi^*_p(ia\sigma)$ in the Hartree-Fock equations 3.23 and summing over i, we find

$$\sum_p \phi^*_p(ia\sigma) \frac{\delta}{\delta \phi^*_p(ia\sigma)} \langle \hat{H} \rangle = \sum_p \phi^*_p(ia\sigma) E_p \phi_p(ia\sigma) = \sum_p E_p. \tag{3.37}$$

Generally speaking, in terms of the amplitudes $\phi_p(ia\sigma)$ any energy functional $E[\phi_p]$ with at most quartic interactions may be written

$$\begin{aligned} E = C + \sum_{pq} \sum_{ijab\sigma} t^{ab}_{ij} \phi^*_p(ia\sigma) \phi_q(jb\sigma) + \\ + \sum_{pqrs} \sum_{ijkl,abcd,\sigma\sigma'} g^{abcd}_{ijkl}(\sigma,\sigma') \phi^*_p(ia\sigma) \phi^*_q(jb\sigma) \phi_r(kc\sigma') \phi_s(ld\sigma'). \end{aligned} \tag{3.38}$$

Plugging this ansatz into Eq. 3.37, we notice that whatever the variational derivative extracts in terms of the ϕ_p amplitude factors, the subsequent multiplication puts right back in. So the left-hand side essentially yields the energy, except that each term in the average is multiplied by a prefactor based on the power of ϕ^*_p in that term (remember that in this variation ϕ and ϕ^* are treated as separate dynamical variables, as is standard in variational calculations involving complex variables). Thus the hopping term $\langle \hat{T} \rangle$ does

[10] one inherent to any Hubbard model type Hamiltonian, where a competition between the localized and itinerant behaviours is present.

not acquire a prefactor, but the electron-electron interaction $\langle \hat{H}_e \rangle$ picks up a factor of 2:

$$\sum_p E_p = \langle \hat{T} \rangle + 2\langle \hat{H}_e \rangle + \langle \hat{H}_{e-latt} \rangle.$$

Re-expressing the hopping contribution,

$$\langle \hat{T} \rangle = \sum_p E_p - 2\langle \hat{H}_e \rangle - \langle \hat{H}_{e-latt} \rangle,$$

it becomes possible to write the expression for the total energy per site without the $\hat{T}$ contribution

$$\frac{E_{GS}}{N} = \frac{1}{N}\Big(\sum_p E_p + E_{latt} - \langle \hat{H}_e \rangle \Big). \tag{3.39}$$

Using the definitions of the Hartree-Fock parameters 3.35 and the expression for $\langle \hat{H}_e \rangle$ from 3.12, we obtain a closed form expression for the mean-field energy in terms of the mean-field parameters only

$$\frac{E_{GS}}{N} = \frac{1}{N}\sum_p E_p + 2\epsilon_b \left(\frac{u^2}{2} + \frac{au^4}{4} \right) - \frac{1}{N}\langle \hat{H}_e \rangle, \tag{3.40}$$

where

$$\begin{aligned} \frac{1}{N}\langle \hat{H}_e \rangle =& \frac{3U-5J}{8}(1+\delta^2) - \frac{U+J}{2}\Big(S^2_{\mathrm{FM}} + S^2_{\mathrm{AFM}} + \\ &+ \frac{S^2_{1\mathrm{x}} + S^2_{1\mathrm{z}} + S^2_{2\mathrm{x}} + S^2_{2\mathrm{z}}}{2} \Big) - 2(U - J(4+\gamma))(O_1^2 + O_2^2) - \\ &- 2(U + (\gamma-2)J)\left(Z_1^2 + Z_2^2 + \frac{Z_3^2 + Z_4^2}{2} \right) - \\ &- (U + (\gamma-2)J)(X_1^2 + X_2^2). \end{aligned} \tag{3.41}$$

(The N comes from the fact that the sum over the sites i yields N identical terms, as per the mean-field assumption. See Appendix C for the complete calculation of $\langle \hat{H}_e \rangle$.) Once a self-consistent solution $\mathbf{w}$ is generated, its energy can be immediately evaluated using this expression.

While the order parameters $\mathbf{w}$ can be guessed initially, it is still not entirely clear how to re-calculate them – or how to find the energies E_p in the first place. In the next section we construct the Hartree-Fock Hamiltonian, which will address both those points.

3.5 Hartree-Fock Hamiltonian

Given the set of Hartree-Fock equations

$$\begin{aligned}E_p\phi_p(ia\sigma) = &\sum_{jb} t_{ij}^{ab}\phi_p(jb\sigma) + \Big[-2\epsilon_b u_i + U\langle d^\dagger_{ia\bar\sigma} d_{ia\bar\sigma}\rangle + U'\langle d^\dagger_{i\bar a\bar\sigma} d_{i\bar a\bar\sigma}\rangle + \\ &+ (U'-J)\langle d^\dagger_{i\bar a\sigma} d_{i\bar a\sigma}\rangle\Big]\phi_p(ia\sigma) + \Big[-U\langle d^\dagger_{ia\bar\sigma} d_{ia\sigma}\rangle - \\ &- J\langle d^\dagger_{i\bar a\bar\sigma} d_{i\bar a\sigma}\rangle\Big]\phi_p(ia\bar\sigma) + \Big[(U'-J)\langle d^\dagger_{i\bar a\sigma} d_{ia\sigma}\rangle + \\ &+ J\langle d^\dagger_{i\bar a\bar\sigma} d_{ia\bar\sigma}\rangle + \gamma J\langle d^\dagger_{ia\bar\sigma} d_{i\bar a\bar\sigma}\rangle\Big]\phi_p(i\bar a\sigma) + \\ &+ \Big[U'\langle d^\dagger_{i\bar a\bar\sigma} d_{ia\sigma}\rangle + \gamma J\langle d^\dagger_{ia\bar\sigma} d_{i\bar a\sigma}\rangle\Big]\phi_p(i\bar a\bar\sigma). \end{aligned} \tag{3.42}$$

or, having in mind the definitions of the various order parameters 3.35 and the spherical symmetry $U' = U - 2J$

$$\begin{aligned}E_p\phi_p(ia\sigma) = &\sum_{jb} t_{ij}^{ab}\phi_p(jb\sigma) + \Big\{\frac{3U-5J}{4} + \Big[\frac{3U-5J}{4}\delta - 2\epsilon_b u\Big] e^{i\mathbf{Q}_c\cdot\mathbf{R}_i} - \\ -\frac{\sigma}{2}(U+J)\Big[&S_{\mathrm{FM}} + S_{\mathrm{AFM}} e^{i\mathbf{Q}_c\cdot\mathbf{R}_i} + S_{1\mathrm{z}}\cos\mathbf{Q}_m\cdot\mathbf{R}_i + S_{2\mathrm{z}}\sin\mathbf{Q}_m\cdot\mathbf{R}_i\Big]\Big\}\phi_p(ia\sigma) - \\ &- \frac{U+J}{2}\left[S_{1\mathrm{x}}\cos\mathbf{Q}_m\cdot\mathbf{R}_i + S_{2\mathrm{x}}\sin\mathbf{Q}_m\cdot\mathbf{R}_i\right]\phi_p(ia\bar\sigma) - \\ &- (U + J(\gamma-2))\Big[X_1\cos\mathbf{Q}_m\cdot\mathbf{R}_i + X_2\sin\mathbf{Q}_m\cdot\mathbf{R}_i\Big]\phi_p(i\bar a\bar\sigma) + \\ + \Big\{(J(4+\gamma)-U)\Big[O_1 + O_2 e^{i\mathbf{Q}_c\cdot\mathbf{R}_i}\Big] - \sigma\Big[U + J(\gamma-2)\Big]\Big[&Z_1 + Z_2 e^{i\mathbf{Q}_c\cdot\mathbf{R}_i} + \\ &+ Z_3\cos\mathbf{Q}_m\cdot\mathbf{R}_i + Z_4\sin\mathbf{Q}_m\cdot\mathbf{R}_i\Big]\Big\}\phi_p(i\bar a\sigma), \end{aligned}$$

it is always reasonable to ask: what *quadratic* Hamiltonian could they have originated from? In other words, what is the Hamiltonian that results after one applies the Hartree-Fock approximation to the original, interacting Hamiltonian in Eq. 2.21? Such a Hamiltonian – now quadratic – and thus easily diagonalizable – is termed *factorized*: it is relatively easy to reconstruct it from the equations. Recalling that $\langle d^\dagger_{ia\sigma} d_{jb\tau}\rangle = \sum_p \phi_p^*(ia\sigma)\phi_p(jb\tau)$, we can visualize what the quadratic Hamiltonian "should have been" in order to produce the equations 3.23 after the expectation value with the trial state $|\Psi_e\rangle = \prod_p a_p^\dagger |0\rangle$ and the variation with respect to $\phi_p^*(ia\sigma)$. For each term, we need to recover the factor $\phi_p^*(ia\sigma)$: moreover, their sum over p ought to be replaced by the appropriate matrix element $\langle d^\dagger_{ia\sigma} d_{jb\tau}\rangle$ and then the expectation values stripped away, leaving the operators d. Following

this procedure, it is straightforward to reconstruct the appropriate quadratic Hamiltonian

$$\begin{aligned}
\hat{H}_{\mathrm{HF}} = \sum_{ijab\sigma} t_{ij}^{ab} d_{ia\sigma}^{\dagger} d_{jb\sigma} + \Big\{ \frac{3U-5J}{4} + \left[\frac{3U-5J}{4}\delta - 2\epsilon_b u \right] e^{i\mathbf{Q}_c\cdot\mathbf{R}_i} - \\
- \frac{\sigma}{2}(U+J)\Big[S_{\mathrm{FM}} + S_{\mathrm{AFM}} e^{i\mathbf{Q}_c\cdot\mathbf{R}_i} + S_{1\mathrm{z}} \cos\mathbf{Q}_m\cdot\mathbf{R}_i + S_{2\mathrm{z}} \sin\mathbf{Q}_m\cdot\mathbf{R}_i \Big] \Big\} d_{ia\sigma}^{\dagger} d_{ia\sigma} - \\
- \frac{U+J}{2} \left[S_{1\mathrm{x}} \cos\mathbf{Q}_m\cdot\mathbf{R}_i + S_{2\mathrm{x}} \sin\mathbf{Q}_m\cdot\mathbf{R}_i \right] d_{ia\sigma}^{\dagger} d_{ia\bar{\sigma}} - \\
- \left(U + J(\gamma-2)\right)\Big[X_1 \cos\mathbf{Q}_m\cdot\mathbf{R}_i + X_2 \sin\mathbf{Q}_m\cdot\mathbf{R}_i \Big] d_{ia\sigma}^{\dagger} d_{i\bar{a}\bar{\sigma}} + \\
+ \Big\{ \left(J(4+\gamma) - U\right)\Big[O_1 + O_2 e^{i\mathbf{Q}_c\cdot\mathbf{R}_i} \Big] \\
- \sigma\Big[U + J(\gamma-2) \Big] \Big[Z_1 + Z_2 e^{i\mathbf{Q}_c\cdot\mathbf{R}_i} + Z_3 \cos\mathbf{Q}_m\cdot\mathbf{R}_i + Z_4 \sin\mathbf{Q}_m\cdot\mathbf{R}_i \Big] \Big\} d_{ia\sigma}^{\dagger} d_{i\bar{a}\sigma}.
\end{aligned}$$

This quadratic Hamiltonian is equivalent, in its ground state and eigenfunctions/eigenvalues, to the original Hamiltonian under the Hartree-Fock approximation: it is the Hartree-Fock Hamiltonian. It has the advantage of being quadratic and thus can be diagonalized, obtaining said eigenvalues/eigenfunctions. Making use of Bloch's theorem is very advantageous here, as the Hamiltonian admits significant block-diagonalization with transforming to Fourier ($\mathbf{k}$) space (which was not the case for the original Hamiltonian because of the 4-operator terms). The details of this are carried out in Appendix D: the result, after some mundane substitutions of the usual Fourier transform

$$d_{\mathbf{k}a\sigma}^{\dagger} = \sum_i \frac{e^{i\mathbf{k}\cdot\mathbf{R}_i}}{\sqrt{N}} d_{ia\sigma}^{\dagger} \tag{3.43}$$

becomes

$$\begin{aligned}
\hat{H}_{\mathrm{HF}} = \sum_{\mathbf{k}ab\sigma} t_{ab}(\mathbf{k}) d^\dagger_{\mathbf{k}a\sigma} d_{\mathbf{k}b\sigma} + \sum_{\mathbf{k}a\sigma} \Big(\frac{3U-5J}{4} - \frac{\sigma}{2}(U+J) S_{\mathrm{FM}} \Big) d^\dagger_{\mathbf{k}a\sigma} d_{\mathbf{k}a\sigma} + \\
+ \Big(\frac{3U-5J}{4}\delta - 2\epsilon_b u - \frac{\sigma}{2}(U+J) S_{\mathrm{AFM}} \Big) d^\dagger_{\mathbf{k}+\mathbf{Q}_c,a\sigma} d_{\mathbf{k}a\sigma} - \\
- \frac{\sigma}{4}(U+J)\Big((S_{1\mathrm{z}} - iS_{2\mathrm{z}}) d^\dagger_{\mathbf{k}+\mathbf{Q}_m,a\sigma} d_{\mathbf{k}a\sigma} + (S_{1\mathrm{z}} + iS_{2\mathrm{z}}) d^\dagger_{\mathbf{k}-\mathbf{Q}_m,a\sigma} d_{\mathbf{k}a\sigma} \Big) - \\
- \frac{U+J}{4}\Big((S_{1\mathrm{x}} - iS_{2\mathrm{x}}) d^\dagger_{\mathbf{k}+\mathbf{Q}_m,a\sigma} d_{\mathbf{k}a\bar{\sigma}} + (S_{1\mathrm{x}} + iS_{2\mathrm{x}}) d^\dagger_{\mathbf{k}-\mathbf{Q}_m,a\sigma} d_{\mathbf{k}a\bar{\sigma}} \Big) \\
- \frac{U+J(\gamma-2)}{2}\Big((X_1 - iX_2) d^\dagger_{\mathbf{k}+\mathbf{Q}_m,a\sigma} d_{\mathbf{k}\bar{a}\bar{\sigma}} + (S_{1\mathrm{x}} + iS_{2\mathrm{x}}) d^\dagger_{\mathbf{k}-\mathbf{Q}_m,a\sigma} d_{\mathbf{k}\bar{a}\bar{\sigma}} \Big) + \\
+ \left[(J(4+\gamma) - U) O_1 - \sigma(U + J(\gamma-2)) Z_1 \right] d^\dagger_{\mathbf{k}a\sigma} d_{\mathbf{k}\bar{a}\sigma} + \\
+ \left[(J(4+\gamma) - U) O_2 - \sigma(U + J(\gamma-2)) Z_2 \right] d^\dagger_{\mathbf{k}+\mathbf{Q}_c,a\sigma} d_{\mathbf{k}\bar{a}\sigma} \\
- \frac{\sigma}{2}(U + J(\gamma-2)) \Big[(Z_3 - iZ_4) d^\dagger_{\mathbf{k}+\mathbf{Q}_m,a\sigma} d_{\mathbf{k}\bar{a}\sigma} + (Z_3 + iZ_4) d^\dagger_{\mathbf{k}-\mathbf{Q}_m,a\sigma} d_{\mathbf{k}\bar{a}\sigma} \Big] .
\end{aligned}$$

Notice that the different $\mathbf{Q}$ prefactors have resulted in the mixing of certain momenta within the Brillouin zone. Instead of folding the Brillouin zone and labeling the resulting states (a so-called reduced zone scheme treatment of the Brillouin zone), we continue to work in the original Brillouin zone (so-called extended scheme [75]).

At this point, the Hamiltonian is ready to be diagonalized: thanks to translational symmetry, it is already block-diagonal in $\mathbf{k}$ and can be written

$$\hat{H}_{\mathrm{HF}} = \sum_{\mathbf{k}} \psi^\dagger_{\mathbf{k}} h(\mathbf{k}) \psi_{\mathbf{k}}$$

where

$$\psi^\dagger_{\mathbf{k}} = (\psi^\dagger_{\mathbf{k}z\uparrow}, \psi^\dagger_{\mathbf{k}\bar{z}\uparrow}, \psi^\dagger_{\mathbf{k}z\downarrow}, \psi^\dagger_{\mathbf{k}\bar{z}\downarrow})$$

and

$$\psi^\dagger_{\mathbf{k}a\sigma} = (d^\dagger_{\mathbf{k}a\sigma}, d^\dagger_{\mathbf{k}+\mathbf{Q}_m,a\sigma}, d^\dagger_{\mathbf{k}+\mathbf{Q}_c,a\sigma}, d^\dagger_{\mathbf{k}-\mathbf{Q}_m,a\sigma}).$$

Hence only separate 16×16 subblocks need to be explicitly diagonalized – a process we implemented in Python and discuss in a subsequent chapter. Explicit expressions for the matrices are available in Appendix D. (Note that this matrix is, due to the properties of the Fourier transform, almost a Toeplitz matrix.)

Once the Hamiltonian is diagonalized, to complete the iteration it is necessary to re-calculate the order parameters $\mathbf{w}$ from the eigenvalues and

eigenfunctions of $\hat{H}_{\mathrm{HF}}$. First off, the eigenfunctions are ordered by their corresponding eigenvalues: according to our quarter-filling scheme, only the bottom quarter are selected to participate in the calculation of the order parameters. The Slater determinant (Hartree-Fock trial wavefunction) is

$$|\Psi_e\rangle = \prod_{\mathbf{k}a\sigma}{}' d^\dagger_{\mathbf{k}a\sigma} |0\rangle$$

where the prime indicates the product over the occupied single-particle states. The matrix elements $\langle\Psi_e| d^\dagger_{\mathbf{k}a\sigma} d_{\mathbf{k}b\tau} |\Psi_e\rangle$ need to be calculated and compared to the values that were guessed for them initially in order to complete the iterative process. The easiest way to proceed is by using the density matrix approach [72]. Define the density matrix associated to the Hartree-Fock ground state by

$$\rho_{\mathbf{k}}(\zeta b\tau, \eta a\sigma) = \langle\Psi_e| d^\dagger_{\mathbf{k}+\eta\mathbf{Q}_m,a\sigma} d_{\mathbf{k}+\zeta\mathbf{Q}_m,b\tau} |\Psi_e\rangle . \tag{3.44}$$

Insert the identity decomposition $1 = \sum_{\mathbf{k}a\sigma} |\mathbf{k}a\sigma\rangle \langle\mathbf{k}a\sigma|$ in between the creation/annihilation operators,

$$\rho_{\mathbf{k}}(\zeta b\tau, \eta a\sigma) = \sum_{pb\sigma'} \langle\Psi_e| d^\dagger_{\mathbf{k}+\eta\mathbf{Q}_m,a\sigma} \left|\mathbf{p}b\sigma'\right\rangle \left\langle\mathbf{p}b\sigma'\right| d_{\mathbf{k}+\zeta\mathbf{Q}_m,b\tau} |\Psi_e\rangle . \tag{3.45}$$

Each of the matrix elements can only be nonzero if the state $|\mathbf{p}b\sigma'\rangle$ is occupied, i.e. it is part of the ground state. So the sum is now primed – only over the occupied states. Moreover, since the expectation value is taken with respect to the ground state of the system, $\langle\Psi_e| d^\dagger_{\mathbf{k}+\eta\mathbf{Q}_m,a\sigma}$ and $d_{\mathbf{k}+\zeta\mathbf{Q}_m,b\tau} |\Psi_e\rangle$ should be considered as single-state excitations. This leads to

$$\rho_{\mathbf{k}}(\zeta b\tau, \eta a\sigma) = \langle\mathbf{k}+\eta\mathbf{Q}_m a\sigma| \left(\sum_{pb\sigma'}{}' \left|\mathbf{p}b\sigma'\right\rangle \left\langle\mathbf{p}b\sigma'\right| \right) |\mathbf{k}+\zeta\mathbf{Q}_m, b\tau\rangle . \tag{3.46}$$

This equation shows that the matrix elements $\langle\Psi_e| d^\dagger_{\mathbf{k}+\eta\mathbf{Q}_m,a\sigma} d_{\mathbf{k}+\zeta\mathbf{Q}_m,b\tau} |\Psi_e\rangle$ are the (reversed) matrix elements of the operator $\rho = \sum'_{pb\sigma'} |\mathbf{p}b\sigma'\rangle \langle\mathbf{p}b\sigma'|$, constructed out of occupied single-particle Hartree-Fock states.

The single-particle states themselves are 16-tuples $|\mathbf{k}a\sigma\rangle$ of numbers. They can be used to construct the density matrix, which can then be used to find the order parameters $\delta, S_{\mathrm{FM}}, ...$ via the Fourier transform rule. This is most easily understood when demonstrated on an explicit example. Recall

the definitions of the order parameters

$$\langle d^\dagger_{ia\sigma} d_{ia\sigma}\rangle = \frac{1}{4}\left[1+\delta e^{i\mathbf{Q}_c\cdot\mathbf{R}_i}\right] + \frac{\sigma}{2}\Big[S_{\mathrm{FM}} + S_{\mathrm{AFM}} e^{i\mathbf{Q}_c\cdot\mathbf{R}_i} + \\ + S_{1\mathrm{z}}\cos(\mathbf{Q}_m\cdot\mathbf{R}_i) + S_{2\mathrm{z}}\sin(\mathbf{Q}_m\cdot\mathbf{R}_i)\Big].$$

Re-arranging into a more convenient form, sorting by the order of the exponential

$$\langle d^\dagger_{ia\sigma} d_{ia\sigma}\rangle = \left[\frac{1}{4}+\frac{\sigma}{2}S_{\mathrm{FM}}\right] e^0 + \left[\frac{\delta}{4}+\frac{\sigma}{2}S_{\mathrm{AFM}}\right] e^{i\mathbf{Q}_c\cdot\mathbf{R}_i} + \\ + \frac{\sigma}{2}\left[\frac{S_{1\mathrm{z}}-iS_{2\mathrm{z}}}{2}\right] e^{i\mathbf{Q}_m\cdot\mathbf{R}_i} + \frac{\sigma}{2}\left[\frac{S_{1\mathrm{z}}+iS_{2\mathrm{z}}}{2}\right] e^{-i\mathbf{Q}_m\cdot\mathbf{R}_i}.$$

Notice that by hitting the matrix element with the appropriate exponential and summing over the sites, we can "project out" the quantities we are interested in: the terms which do not have the same exponential will sum to zero. For instance, simply summing over sites i and orbitals a leaves only the non-varying terms (other terms oscillate in sign and cancel out, a typical trick in condensed matter calculations – see [75] appendix for this shown explicitly) – the sum over a only contributes an overall factor of 2

$$\sum_{ia}\langle d^\dagger_{ia\sigma} d_{ia\sigma}\rangle = N\left[\frac{1}{2}+\sigma S_{\mathrm{FM}}\right].$$

Using the fact that the sign is different for the up and down spins, we can isolate for S_{FM} by multiplying by σ and summing over it

$$S_{\mathrm{FM}} = \frac{1}{2N}\sum_{ia\sigma}\sigma\langle d^\dagger_{ia\sigma} d_{ia\sigma}\rangle.$$

Finally, to make connection with the $|\mathbf{k}+\eta\mathbf{Q}_m, a\sigma\rangle = d^\dagger_{\mathbf{k}+\eta\mathbf{Q}_m,a\sigma}|0\rangle, \eta \in \{0,1,2,-1\}$ eigenfunctions that are actually found during diagonalization of the Hartree-Fock Hamiltonian, Fourier-transform the operators inside the expectation values. Since in this particular case only on-site operators are involved and there are no exponential prefactors, the Fourier transform is immediate and yields

$$S_{\mathrm{FM}} = \frac{1}{2N}\sum_{\mathbf{k}a\sigma}\sigma\langle d^\dagger_{\mathbf{k}a\sigma} d_{\mathbf{k}a\sigma}\rangle = \frac{1}{2N}\sum_{\mathbf{k}\eta a\sigma}\sigma\rho_{\mathbf{k}}(\eta a\sigma,\eta a\sigma). \tag{3.47}$$

The matrix element $\langle d^\dagger_{\mathbf{k}a\sigma} d_{\mathbf{k}a\sigma}\rangle$ is an expectation value of the number operator $\hat{n}_{\mathbf{k}a\sigma}$ in the Hartree-Fock ground state $|\Psi_e\rangle$. It is also simply an entry

of the density matrix 3.46. Let us explicitly illustrate how to evaluate such a sum relative to the 16×16 block density matrix at each value of momentum. In this case, the sum is over diagonal elements only: yet even for a single value of $\mathbf{k}a\sigma$, there are still four entries that need summing over, namely

$$\begin{aligned}S_{\mathrm{FM}} =&\frac{1}{2N}\sum_{\substack{\mathbf{k}\text{ in }[-\frac{\pi}{a},\frac{\pi}{a}]^3\\ \text{and }a\sigma}}\sigma\Big(\langle d^\dagger_{\mathbf{k}a\sigma}d_{\mathbf{k}a\sigma}\rangle+\langle d^\dagger_{\mathbf{k}+\mathbf{Q}_m,a\sigma}d_{\mathbf{k}+\mathbf{Q}_m,a\sigma}\rangle+\\ &+\langle d^\dagger_{\mathbf{k}+2\mathbf{Q}_m,a\sigma}d_{\mathbf{k}+2\mathbf{Q}_m,a\sigma}\rangle+\langle d^\dagger_{\mathbf{k}-\mathbf{Q}_m,a\sigma}d_{\mathbf{k}-\mathbf{Q}_m,a\sigma}\rangle\Big)=\\ &=\frac{1}{2N}\sum_{\substack{\mathbf{k}\text{ in }[-\frac{\pi}{a},\frac{\pi}{a}]^3\\ \text{and }\eta a\sigma}}\sigma\Big(\rho_{\mathbf{k}}(0a\sigma,0a\sigma)+\rho_{\mathbf{k}}(1a\sigma,1a\sigma)+\\ &+\rho_{\mathbf{k}}(2a\sigma,2a\sigma)+\rho_{\mathbf{k}}(-1a\sigma,-1a\sigma)\Big).\end{aligned}\tag{3.48}$$

Similar expressions can be obtained for the other order parameters. Note that for certain sums with displaced indices, it is necessary to sum over "looped" entries. For instance, consider obtaining the charge disproportionation order parameter: after the usual exponential multiplication and summation trick,

$$\sum_i e^{2i\mathbf{Q}_m\cdot\mathbf{R}_i}\langle d^\dagger_{ia\sigma}d_{ia\sigma}\rangle=N\left[\frac{\delta}{4}+\frac{\sigma}{2}S_{AFM}\right].$$

Fourier transforming on the left and summing over the spin and orbital degrees of freedom,

$$\delta=\frac{1}{N}\sum_{\mathbf{k}a\sigma}\langle d^\dagger_{\mathbf{k}+\mathbf{Q}_c,a\sigma}d_{\mathbf{k}a\sigma}\rangle.\tag{3.49}$$

Summing over all allowed values of $\mathbf{k}$, we inevitably stumble upon entries like $\langle d^\dagger_{\mathbf{k}+2\mathbf{Q}_c,a\sigma}d_{\mathbf{k}+\mathbf{Q}_c,a\sigma}\rangle=\langle d^\dagger_{\mathbf{k},a\sigma}d_{\mathbf{k}+\mathbf{Q}_c,a\sigma}\rangle$: such entries are from the upper triangle of the matrix subblock and need to be summed together with those from the lower triangle. Thus, the matrix 16×16 subblock can be thought of as having "bands" that correspond to particular momentum space separation between the column and row. In the example above, the separation is $\mathbf{Q}_c$: the matrix bands that correspond to that are of $(i,j+2)$ and $(i+2,j)$ type, that is, the second off-diagonals. In the case of S_{FM} there was zero separation (this corresponds to the true diagonal of the matrix subblock). For the curious case of $\mathbf{Q}_m$ separation, the bands consists of the nearest

off-diagonal and together with the opposite corner of the matrix. Interestingly, for the case of both δ and S_{AFM}, this sort of summation ensures they are both real without requiring the matrix entries themselves to be real (because the sum is over the two diagonals that are each other's Hermitian conjugates). Naturally, the reality of S_{FM} is ensured by the fact that it only includes diagonal entries. All of the order parameters are re-calculated and the expressions are cataloged in Appendix E.

One final point: since it is clear from the above that there is no momentum mixing (this is a feature of the Hartree-Fock approximation), from a computational perspective it is useful to first quickly calculate the total density matrix $\rho = \sum' |\mathbf{k}a\sigma\rangle \langle \mathbf{k}a\sigma|$, then merely extract the components one requires from it.

Chapter 4

Numerical implementation of the Hartree-Fock approximation

> Part of the inhumanity of the computer is that, once it is competently programmed and working smoothly, it is completely honest.
>
> Isaac Asimov (1981)

The equations have been derived, the expression for the total energy obtained: we have reached the extent of what can be done by hand. The next step is to implement the solution procedure (and, much more importantly, automated sweeping/analysis) on the computer. This is necessary not only because it is infeasible to diagonalize 16×16 matrices by hand (especially ones that involve complex expressions, such as the ansatzes for $\langle d^\dagger_{ia\sigma} d_{ib\tau} \rangle$ and the hopping coefficients $t_{ab}(\mathbf{k})$), but also because the number of mean-field order parameters $\mathbf{w}$ and adjustable parameters $U, J, ...$ is extremely large when compared to the typical mean-field model. Its thorough analysis demands a computerized approach, such that the true ground state in the multi-parameter $\mathbf{w}$ space is surely identified, and all the relationships between the different adjustable parameters and how they affect the ground state is duly cataloged and categorized. In this chapter we describe this process in detail.

4.1 The Hartree-Fock iterative algorithm

The task at hand is to find the ground state of the Hamiltonian $\hat{H}$ 2.21. As already mentioned, in this thesis this is accomplished within the Hartree-Fock approximation: this produces a properly factorized companion Hamil-

tonian $\hat{H}_{\mathrm{HF}}$. Even though the Hamiltonian thus obtained is quadratic and so nominally exactly solvable, its coefficients depend on its own eigenfunctions: the Hartree-Fock equations are nonlinear and thus must be solved iteratively. The Hamiltonian to diagonalize is

$$\hat{H}_{\mathrm{HF}} = \sum_{\mathbf{k}} \psi^{\dagger}_{\mathbf{k}} h(\mathbf{k}) \psi_{\mathbf{k}} \tag{4.1}$$

where

$$\psi^{\dagger}_{\mathbf{k}} = (\psi^{\dagger}_{\mathbf{k}z\uparrow}, \psi^{\dagger}_{\mathbf{k}\bar{z}\uparrow}, \psi^{\dagger}_{\mathbf{k}z\downarrow}, \psi^{\dagger}_{\mathbf{k}\bar{z}\downarrow}),\ \psi^{\dagger}_{\mathbf{k}a\sigma} = (d^{\dagger}_{\mathbf{k}a\sigma}, d^{\dagger}_{\mathbf{k}+\mathbf{Q}_m,a\sigma}, d^{\dagger}_{\mathbf{k}+\mathbf{Q}_c,a\sigma}, d^{\dagger}_{\mathbf{k}-\mathbf{Q}_m,a\sigma}),$$

and the matrix $h(\mathbf{k})$ is given in Appendix D. The energy can be evaluated with the help of the expression from Chapter 3

$$\frac{E_{GS}}{N} = \frac{1}{N}\sum_{p} E_p + 2\epsilon_b N \left(\frac{u^2}{2} + \frac{a u^4}{4} - \langle \hat{H}_e \rangle \right), \tag{4.2}$$

where

$$\begin{aligned} \frac{1}{N}\langle \hat{H}_e \rangle =& \frac{3U-5J}{8}(1+\delta^2) - \frac{U+J}{2}\Big(S^2_{\mathrm{FM}} + S^2_{\mathrm{AFM}} + \\ &+ \frac{S^2_{1\mathrm{x}} + S^2_{1\mathrm{z}} + S^2_{2\mathrm{x}} + S^2_{2\mathrm{z}}}{2} \Big) - 2(U - J(4+\gamma))(O_1^2 + O_2^2) - \\ &- 2(U + (\gamma-2)J)\left(Z_1^2 + Z_2^2 + \frac{Z_3^2 + Z_4^2}{2} \right) - \\ &- (U + (\gamma-2)J)(X_1^2 + X_2^2). \end{aligned} \tag{4.3}$$

Finally, the matrix elements that the Hartree-Fock Hamiltonian relies on can be re-calculated from the density matrix using the expressions in the Appendix E.

Let us sketch out the iterative solution process by which the ground state is found.

1. Choose parameter values $U, J, ...$ from the parameter regime of interest.

2. Create a pool of initial guess values for the mean-field parameters $\mathbf{w}^{(0)} = (\delta^{(0)}, S^{(0)}_{\mathrm{FM}}, S^{(0)}_{\mathrm{AFM}}, ...)$. Think physically about what they mean and what states/symmetries could be present in this parameter region. Without good guesswork, it is likely the iterative solution will not work.

(a) Pick one of the initial guesses and start the iterative solution sequence:

(b) i. Initialize the Hartree-Fock matrix $\hat{H}_{\mathrm{HF}}$ using the guessed order parameter values.

ii. Diagonalize the Hamiltonian, then build the ground state density matrix $\rho = \sum'_{\mathbf{k}a\sigma} |\mathbf{k}a\sigma\rangle \langle \mathbf{k}a\sigma|$ at quarter-filing. That is, order the eigenvectors obtained during minimization by their eigenvalues, then pick the bottom quarter.

iii. Re-compute the order parameters $\mathbf{v}^{(0)}$ using the expressions in the Appendix E: evaluate the residual $\epsilon^{(0)} = \left|\mathbf{w}^{(0)} - \mathbf{v}^{(0)}\right|^2$.

iv. Check if $\epsilon^{(0)} < \epsilon_0$, the pre-established convergence condition. If yes, output the eigenvectors $|\mathbf{k}a\sigma\rangle$ and eigenvalues $E_{\mathbf{k}a\sigma}$. If not, repeat this loop with the initial guess being the newly found solution, $\mathbf{w}^{(1)} = \mathbf{v}^{(0)}$ (or choose it in an more involved way – more on such techniques later). If the maximum allowed number of iterations n_{maxiter} is exceeded, quit.

(c) If the sequence converged, evaluate the total state energy E_{HF}.

3. When all the guesses from the pool have been explored, pick the lowest energy solution as the best approximation of ground state.

In principle, this algorithm, together with the Eqs. 4.1–4.2, should be sufficient to fully solve the problem. However, in principle the energy landscape can be complex and have multiple local minima, manifesting as different unique solutions to the self-consistency equations. We found that there are many possibilities for improving convergence for difficult types of guess states, ensuring that the true ground state is identified, as well as simply speeding up the convergence process.

4.2 Strategies for improving computation

4.2.1 Pulay mixing

Although the self-consistent algorithm (4.1) suggests to always re-start the algorithm on step $n+1$ with the updated guess $\mathbf{w}^{(n)}$ being the solution $\mathbf{v}^{(n-1)}$ from the previous step, in fact one can do much better. The simplest generalization is to use, as the guess for the next step $\mathbf{w}^{(n)}$, an interpolation between the guess $\mathbf{w}^{(n-1)}$ and the solution $\mathbf{v}^{(n-1)}$ obtained with this guess,

$$\mathbf{w}^{(n)} = \mathbf{v}^{(n-1)}\alpha + \mathbf{w}^{(n-1)}(1-\alpha). \tag{4.4}$$

The literature on nonlinear iterative equation solution techniques suggests the optimal choice of α that ensures fastest convergence is highly problem specific [76]. Our experience appears to be that $\alpha = 0.3$ produces the smoothest and most reliable iterations. The key advantage of this "cautious convergence" technique that only admixes part of the newly-found solution into the guess is being able to avoid the iteration getting stuck in a loop, or helplessly hopping on either edge of a flat minimum.

However, this approach works best in conjunction with another idea called Pulay mixing, or direct inversion in the iterative subspace (DIIS). The idea behind DIIS, originally developed for high-dimensional[11] Hartree-Fock quantum chemistry calculations by Pulay [77], is the following: suppose a sequence of N solutions $\mathbf{v}^{(1)}, \mathbf{v}^{(2)}, ...\mathbf{v}^{(N)}$ to the nonlinear system has been generated. Together, they span a linear subspace $V_N = \text{span}\{\mathbf{v}^{(1)}, \mathbf{w}^{(2)}, ...\mathbf{w}^{(N)}\}$ within the higher-dimensional (possibly nonlinear) solution manifold V. It is possible to pick the "best possible" vector $\mathbf{w}^{(N+1)}$ within this linear subspace, by minimizing the total error E.

To construct this best possible vector, consider a linear combination of the vectors spanning the solution subspace with some *a priori* unknown coefficients c_m

$$\mathbf{w}^{(N+1)} = \sum_{m=1}^{N} c_m \mathbf{v}^{(m)}. \tag{4.5}$$

It turns out that a good way to pick the coefficients c_m is so as to minimize the residuum vector $\Delta\mathbf{w}^{(N+1)}$, defined as

$$\Delta\mathbf{w}^{(N+1)} = \sum_{m=1}^{N} c_m(\mathbf{v}^{(m)} - \mathbf{w}^{(m)}), \tag{4.6}$$

subject to the constraint that the coefficients sum to one (i.e. the linear combination in 4.5 is actually a convex combination, picking a vector from inside the space V_N)

$$\sum_{m=1}^{N} c_m = 1. \tag{4.7}$$

Define the total error E as the magnitude squared of the residuum vector, $E = ||\sum_m^N c_m(\mathbf{v}^{(m)} - \mathbf{w}^{(m)})||^2$, and minimize it, together with the Lagrange

[11] in terms of the number of order parameters involved.

multiplier factor $\lambda(1-\sum_m^N c_m)$ (which ensures the condition 4.7 holds) with respect to the coefficients c_m. Differentiating with respect to c_j gives a series of equations

$$\frac{\partial}{\partial c_j}\Big(||\sum_m^N c_m(\mathbf{v}^{(m)}-\mathbf{w}^{(m)})||^2+\lambda(1-\sum_m^N c_m)\Big)=\frac{\partial}{\partial c_j}\Big(\sum_m^N c_m^2(\mathbf{v}^{(m)}-$$
$$-\mathbf{w}^{(m)})^2+2\sum_{m<n}^N c_m c_n(\mathbf{v}^{(n)}-\mathbf{w}^{(n)})\cdot(\mathbf{v}^{(m)}-\mathbf{w}^{(m)})+\lambda(1-\sum_m^N c_m)\Big)=$$
$$=2c_j(\mathbf{v}^{(j)}-\mathbf{w}^{(j)})^2+2\sum_{m\neq j} c_m(\mathbf{v}^{(j)}-\mathbf{w}^{(j)})\cdot(\mathbf{v}^{(m)}-\mathbf{w}^{(m)})-\lambda=$$
$$=\sum_m c_m(\mathbf{v}^{(j)}-\mathbf{w}^{(j)})\cdot(\mathbf{v}^{(m)}-\mathbf{w}^{(m)})-\lambda. \tag{4.8}$$

In the last step a re-scaling of the (arbitrary) Lagrange multiplier λ allowed us to get rid of the factor of 2. Adopting the notation $B_{jm}=(\mathbf{v}^{(j)}-\mathbf{w}^{(j)})\cdot(\mathbf{v}^{(m)}-\mathbf{w}^{(m)})$, the system of equations, together with the constraint 4.7 may be written

$$\begin{pmatrix} B_{11} & B_{12} & .. & B_{1N} & -1 \\ B_{21} & B_{22} & .. & B_{2N} & -1 \\ . & ... & .. & ... & .. \\ B_{N1} & B_{N2} & .. & B_{NN} & -1 \\ -1 & -1 & .. & -1 & 0 \end{pmatrix}\begin{pmatrix} c_1 \\ c_2 \\ ... \\ c_N \\ \lambda \end{pmatrix}=\begin{pmatrix} 0 \\ 0 \\ .. \\ 0 \\ -1 \end{pmatrix}. \tag{4.9}$$

So the search for the best possible vector within the subspace V_N amounts to solving an $N+1\times N+1$ system of linear equations (hence the "inversion of the iterative subspace" – for more details, see Ref. [77]). This approach already yields an improvement on the iterative process.

But one can do even better than this. Of course, the Pulay approach can quickly maximize the potential of the vectors within the subspace V_N: but what if the true solution is outside the subspace by more than the allowed residual ϵ_0 to begin with? Then no matter how many times Pulay mixing is carried out, it will not result in improved convergence – instead, it will slow down the search. The fix to this, as shown by Banerjee and co-workers [76], is to intersperse Pulay mixing with regular updates of the form 4.4, with a given periodicity k (typically $k=3$). The algorithm thus alternates between expanding its iterative subspace, and finding the lowest residual vector within it, resulting in optimal convergence for most parameter values. In fact, our calculations show that this approach can even arrest divergences

from round-off error accumulation. Small errors (*e.g.* some order parameters being nonzero while they should be zero for this particular type of state) often cause rapid divergence of the Hartree-Fock iterative trajectory away from a solution. Yet the Pulay approach appears to counteract that tendency, gently guiding the trajectory towards the self-consistent point by resetting the creeping small errors in irrelevant order parameters back to zero.

4.2.2 Convergence in iteration count and momentum sampling

From the standpoint of standard iterative solution theory, there are two key parameters that need to be tested for convergence: the cutoff iteration count n_{maxiter} and the number of points sampled in the Brillouin zone $n_{\text{num-k-pts}}$. It is clear that too fine of a sampling of momentum space can slow down the calculation time as $\mathcal{O}(N^3)$: as for the cutoff iteration count, it needs to be large enough to allow convergence for the interesting solutions, while not so large so as to waste computation time on "dead-end" iterative trajectories that never converge. Long-time convergence studies, studying both the number of identified self-consistent solutions, as well as the behaviour of the per-site ground state energy for those solutions, show that a k-space sampling rate of 25 points per dimension, or $n_{\text{num-k-pts}} = 25^3 \sim 15,000$ points total, along with the cutoff iteration count $n_{\text{max-iter}} = 500$ are optimal for our purposes, taming the residual error $\epsilon^{(n)}$ to less that $\epsilon_0 = 10^{-4}$ and the differences in energy between subsequent iterations to less than 10^{-3}.

4.2.3 Choosing initial guesses

A good update choice strategy for picking the next guess for the iteration, such as Pulay mixing, is paramount to reaching converged solutions. However, equally important is the choice of the *initial guesses* $\mathbf{w}^{(0)}$ for the iterative trajectory: our early calculations quickly showed that a lion's share of the initial guesses chosen at random never lead to interesting converged solutions even if they are known to exist, no matter how high the cutoff n_{matiter} is. Through a combination of physical thinking and grueling calculations with extremely large $n_{\text{max-iter}}$ and fine random sampling of the initial guesses, we identified a multitude of key converged states, which include the ferro/antiferromagnetic solutions ($\uparrow\uparrow\uparrow\uparrow$ and $\uparrow\downarrow\uparrow\downarrow$), the non-interacting zero-spin solution 0000, fully charge-disproportionated 4-site antiferromagnetic solution ($\Uparrow 0 \Downarrow 0$), and the collinear and non-collinear 4-site solutions $\uparrow\uparrow\downarrow\downarrow$,

$\uparrow\rightarrow\downarrow\leftarrow$, along with a few others. For subsequent calculations these high-symmetry solutions are always included as initial guesses: this enhanced both the reliability of converging one of these states, as well as the speed of sweeping the parameter space.

4.2.4 Parallelization

As can be seen from the self-consistent algorithm (4.1), the calculation of an iterative trajectory is not an easily parallelalizable process. The diagonalization of an individual 16×16 block submatrix for each momentum can be done in parallel, but the additional difficulties of structuring the storing and writing of the matrix and its eigenvalues/eigenvectors and the fact that each diagonalization process is very fast on its own makes this option unattractive. On the other hand, there are more high-level parallelization opportunities possible: (a) multiple initial guesses can be made and followed through on for the same set of parameter values $U, J, ...$, and (b) ground states can be found at multiple parameter values at once. In our calculation we opted for option (b) due to ease of implementation and data management and because it resulted in immediate linear speed-up of the calculation (of course, ground states corresponding to different parameter values are independent from each other, hence there is no overhead to the parallelization).

4.2.5 Boot-strapping with neighbouring points

While the calculations at neighbouring points in the parameter space may be independent from each other, they can benefit from using each other's converged solutions as initial guesses for starting new iterative trajectories. On the grounds of adiabaticity (which should apply at least far away from any phase boundaries), we expect small changes in the values of various parameters $U, J, t_1, ...$ to lead to small changes in the nature of the ground state (characterized by its order parameter vector $\mathbf{w}$): as such, an already converged solution from a neighbouring point can result in fast convergence to a similar kind of converged solution at the current point, further improving the reliability of the calculation and reducing computation time.

Armed with the algorithm 4.1, the analytical equations 4.1 – 4.2 and the numerical tricks from this chapter, we are ready to tackle the problem and look at the results.

Chapter 5

Results

> An approximate answer to the right problem is worth a good deal more than an exact answer to an approximate problem.
>
> John Tukey (1962)

Before discussing the results of applying the Hartree-Fock approximation to the nickelates, let us once again reiterate our inspiration for and goals for our research. Our study of the nickelates is largely motivated by the recent observation that the coupling to the lattice distortion has a significant impact on electronic behaviour and might ultimately be responsible for triggering the MIT, with no need for actual charge disproportionation [32]. In light of this, and the peculiar fact that the magnetic transition only coincides with the MIT for sufficiently weak lattice coupling (manifested by the Eu to Lu part of the nickelate series), we wanted to investigate what impact, if any, the lattice coupling can have on the magnetic transition. So we built an effective two-band Hubbard model for the nickelates, in the spirit of the calculation of Lee *et al.* [26], and coupled it to the lattice semiclassically, with three goals in mind:

1. Confirm quantitatively the earlier findings that the lattice coupling forces charge disproportionation;

2. See what magnetic orders are self-consistent, in a mean-field calculation, within our model;

3. Observe whether one of the orders suggested in the literature, or another order that obtains in the calculation, is stabilized by the coupling to the lattice.

5.1 Charge order and the Metal-Insulator Transition

The experimental observation that the temperature of the metal-insulator transition T_{MIT} is higher than the temperature of the magnetic transition T_{N} for the heavier nickelates, along with the strong effect that higher neutron count isotope substitutions of O^{18} have on this temperature [31], suggest the primacy of electron-phonon interactions in the charge ordering process over that of the electron-electron interactions. A recent study [32] clearly demonstrated the possibility of charge disproportionation without overt charge transfer in the nickelates (see Sec. 1.4), being driven mostly by the coupling of ligand holes to the (static) lattice distortions. Here we reproduce this result, showing that even a Holstein-like on-site coupling between the lattice and the electronic degrees of freedom can drive the system through a metal-insulator transition. This is because the on-site coupling mimics the effect of encouraging double occupancy of the shrunk site, as is obtained more naturally from the ligand hole picture.

To first get an idea of what the phase space is like and how charge disproportionation δ depends on the various adjustable parameters, we plot the value of δ for the ground state in the U–J plane. Other parameters are set to the values used in the Lee *et al.* study [26]: $t_1 = 1, t_2 = 0.15, t_4 = 0$ and there is no coupling to the lattice ($\epsilon_b = 0$) for the moment. The data in Fig. 5.1 consists of a 40×40 grid of solutions, where at each point in the grid we carried out the full self-consistent calculation and obtained the ground state. In total, to obtain the figure, we carried out 1,600 calculations, each of which started from a pool of 20-30 initial guesses (or more, depending on its neighbours) and proceeded through anywhere from 5 to 250 iterative steps (where each iterative step involves the diagonalization of roughly 15,000 16×16 subblocks of the Hartree-Fock matrix, as well as the calculation of the density matrix and the order parameters $\mathbf{w}$).

All in all, Fig. 5.1 shows qualitative agreement with earlier studies (such as those of Lee *el al.* [26] or Peters [78]), as well as with basic physical intuition. The small U, small J region exhibits no charge modulation, as it is largely metallic (the hopping dominates the interactions), with a robust weight at the Fermi level (see density of state plots for various representative points in the U–J phase diagram in Fig. 5.2). Upon increasing U no modulation arises either: strong on-site Coulomb repulsion opposes charge density waves, instead favouring on-site localization. Finally, regardless of the magnitude of U, for J large enough it becomes possible to stabilize

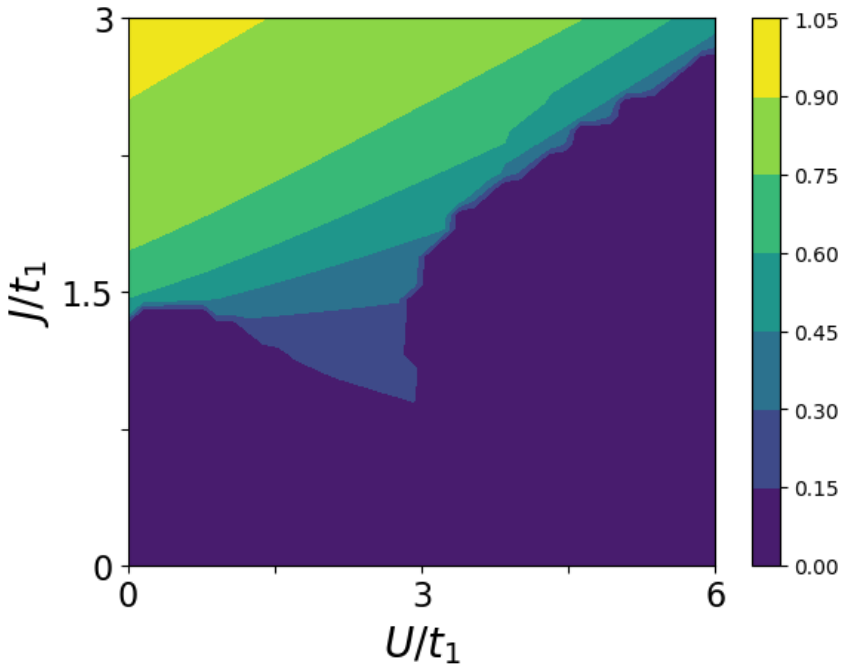

Figure 5.1: Charge modulation δ (the magnitude is reflected in the colour bar) of the ground state in the U–J plane. Other parameters are $t_1 = 1, t_2 = 0.15, t_4 = 0, \epsilon_b = 0$. Resolution is 40×40.

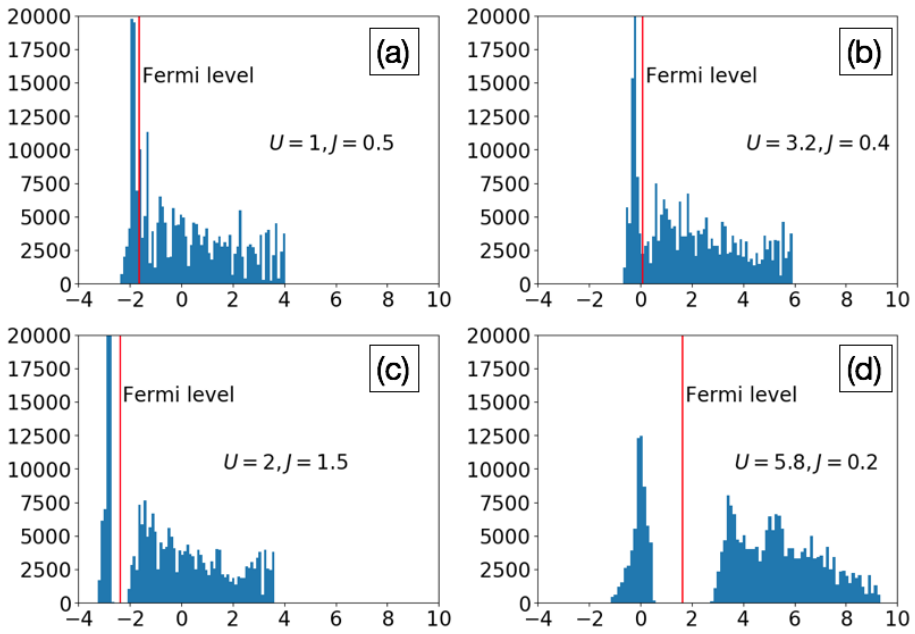

Figure 5.2: Representative density of states diagrams for the various phases in Fig. 5.1: (a) metallic phase, $U = 1.077, J = 0.538$; (b) itinerant magnetic phase (see the magnetic phase analysis below for more details about this phase), $U = 3.231, J = 0.385$; (c) charge modulated phase, with a clear gap at the Fermi level, $U = 2.0, J = 1.538$; (d) Mott insulating phase, $U = 5.846, J = 0.231$. Other parameters as in Fig. 5.1, with the addition of $\alpha = 1$. Notice the increased weight (called the van Hove singularity) at the lower band edge: its presence is due to the nonzero t_2 parameter, which introduces a strong asymmetry to the DOS. More on this below.

charge density wave order thanks to Hund's rule. It minimizes the energy by "poaching" an electron from a neighbouring site, then organizing the two electrons into a triplet state across the two orbitals $|z\rangle, |\bar{z}\rangle$. This is favourable even despite the increased on-site inter-orbital repulsion from U (although it does take a larger J to accomplish this if U is large).

What of the lattice? To investigate the impact from turning on the lattice coupling ϵ_b we turn to Figs. 5.3 and 5.4, where the U–ϵ_b diagrams of charge disproportionation and metal-insulator behaviour are presented for various ratios of J/U, from a modest 0.2 to a more experimentally reasonable 0.5. These diagrams essentially represent line slices of the U–J diagram emanating from the origin in the lower left corner, with the new dimension

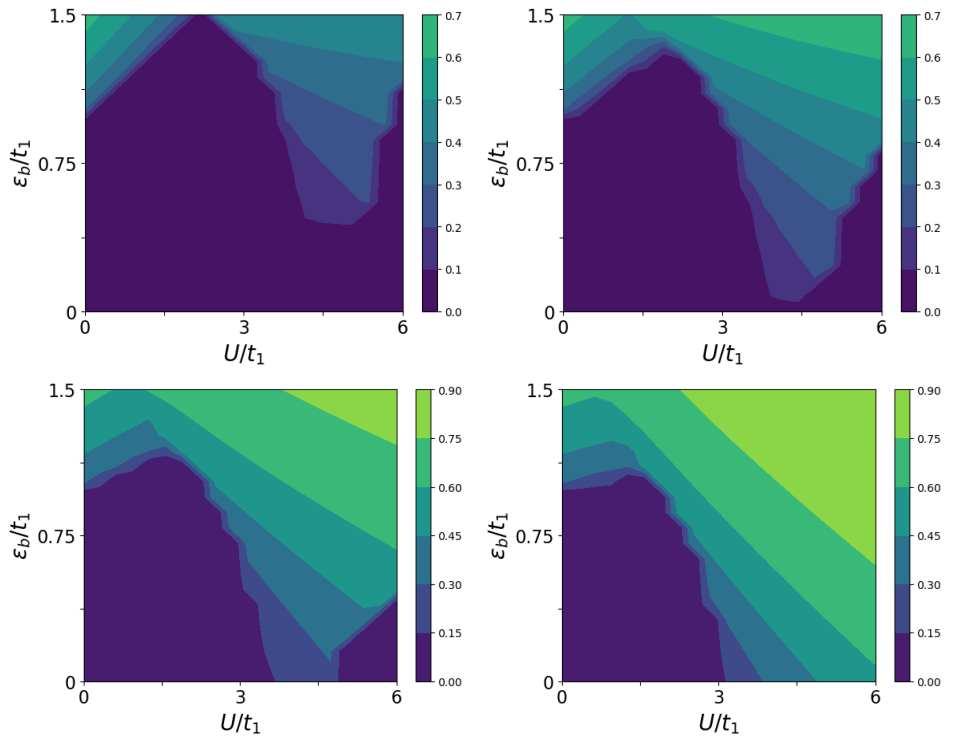

Figure 5.3: Charge modulation δ (see colour scale) in the HF ground-state, as a function of U and ϵ_b, for $J/U = 0.2, 0.3$ (top left and right, respectively) and $0.4, 0.5$, (bottom left and right, respectively). Other parameters are $t_1 = 1, t_2 = 0.15, t_4 = 0.25, \alpha = 1$. Resolution is 20×20.

showing the impact of lattice coupling ϵ_b. Here we let $t_4 = 0.25$: the impact of this on the diagram is not extensive and will be reviewed later. The reason we include it here is to ensure that all of the pieces of our model (including the 4^{th} neighbour hopping) are present during the analysis.

Overall the behaviour again conforms to expectations from earlier work. For small U (and thus an even smaller J) the system is fully metallic (as can be seem from the metal-insulator diagrams), and $\delta = u = 0$ (recall that in our model u is essentially fixed by δ as per the self-consistency equation for u). In the absence of coupling to the lattice, just as was seen in Fig. 5.1, there is already a transition to a finite $\delta \neq 0$ state with increasing J, which occurs sooner for larger slopes J/U. This can be readily explained, as for larger J/U the propensity for two-orbital triplet occupancy (Hund's order) grows faster than the push towards single-site localization (Mott-Hubbard

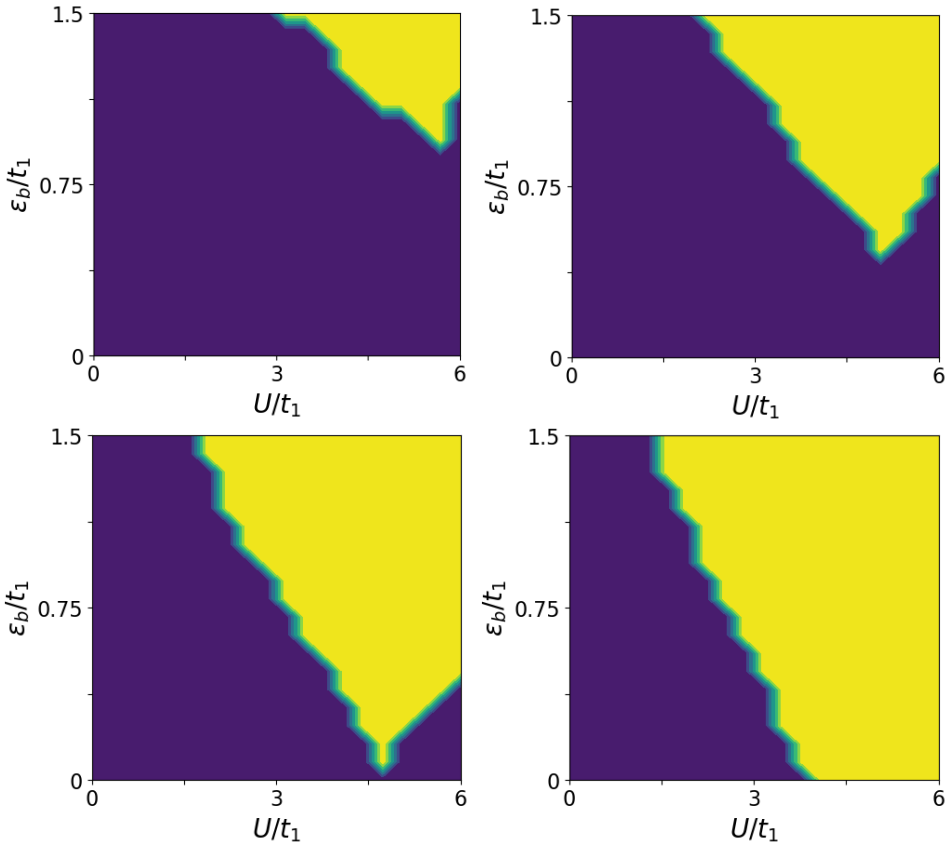

Figure 5.4: The HF ground-state is metallic (deep blue) or insulating (yellow). The results are shown in the U-ϵ_b space, for $J/U = 0.2, 0.3, 0.4$ and 0.5, respectively (panels arranged as in Fig. 5.3). All other parameters are as in Fig. 5.3.

localization). And once the coupling to the lattice is introduced, no matter what U and slope J/U we are considering, at large enough coupling strengths the system will gravitate towards the charge modulated state.

To summarize, we find that our model supports the existence of the MIT, triggered by modulating material parameters (in particular, electron interaction strength U, J). It manifests as a charge density wave with nonzero charge modulation $\delta \neq 0$. The introduction of the lattice further enhances the favourability of the charge density wave order across the parameter space, the onset being more dramatic for larger values of J/U: the resulting lattice distortion $u \neq 0$ is readily obtained from the charge disproportionation δ via the self-consistency condition derived earlier in Eq. 3.5.

5.2 Magnetic order: types and the transition

Having confirmed the existence of the MIT within the model and "soft-benchmarked" it against earlier works by confirming that charge modulation arises for large J, we move on the primary subject of this thesis: the issue of the magnetic order and its interaction with the lattice degrees of freedom. Once again, we begin by analyzing the large-scale picture of phases in the U–J plane. Before we discuss the insights it provides, note that in general at most points in the diagram there are many different types of self-consistent solutions from which to pick the ground state. Below is a list of most of the types of magnetic order states that we identified during our searches:

1. The "no magnetic order", fully metallic solution 0000;
2. The ferromagnetic solution ↑↑↑↑;
3. The antiferromagnetic solution ↑↓↑↓;
4. The fully disproportionated antiferromagnetic solution ⇑ 0 ⇓ 0 order, favoured by some in the literature [25];
5. The non-disproportionated collinear solution ↑↑↓↓, the focus of the work of Lee *et al.* [26];
6. The non-disproportionated non-collinear solution ↑→↓←, suggested by several recent studies [27, 28];
7. A variety of unexpected orbital-order states such as spin ordered ⇑↓⇑↓ with ferroorbital order of type $XxXx$ (an x indicates a preference for the orbital $|x\rangle = (1/2)(|z\rangle + |\bar{z}\rangle)$, with magnitude again reflecting the

size of the preference): we will refer to this state as the disproportionated ferroorbital order;

8. Moreover, we see the states ⇑↑⇑↑ (the aligned ferrimagnetic state), as well as various odd asymmetric ones such as ⇑↓↑↓ (but they are always higher energy states and involve orbital order).

9. There are even more possibilities, which sometimes even manifest as ground states, that are associated with complex combinations of the spin and orbital order: states such as ↑→↓←, $0x0\bar{x}$, or →→←← $xx\bar{x}\bar{x}$. In this thesis we do not spend much time studying such states, partly because they rarely occupy much space in the phase diagram. They manifest mostly when the hopping integrals are adjusted. All such states are marked with "misc" label in the phase diagrams and their study is relegated to future work.

Only a select few of these states actually end up having a robust presence in the magnetic phase diagrams. Consider Figs. 5.5, the magnetic phase diagrams in the U–J plane at the reference parameter values of Lee *et al.*, with the coupling to the lattice $\epsilon_b = 0$ in the first and $\epsilon_b = 0.8$ in the second. The black contours represent the (interpolated) value of δ. There are several items of note here: first of all, the magnetic diagram with no lattice coupling again exhibits qualitative agreement with prior work: a non-magnetic, metallic phase is found for small U/small J; large values of Hubbard U result in the presence of a ferromagnetic state ↑↑↑↑ due to localization of the electrons; and large values of J lead to charge modulation and as a consequence two inequivalent spin sublattices, one of which is almost entirely devoid of magnetic moment and the other is antiferromagnetically ordered, ⇑ 0 ⇓ 0.

One crucial distinction we point out at this stage: Lee *et al.* find a thin ribbon-like region of intermediate-magnet phase ⇑↑⇓↓ between the ⇑ 0 ⇓ 0 large J phase and the ↑↑↓↓ medium-to-large U phase. We do not find such an intermediate phase at all: in fact, in all our calculations we have never been able to successfully converge a magnetic state with (a) nonzero charge disproportionation **and** (b) both magnetic sublattices having nonvanishing magnetic moments. It appears that solutions of this type are simply not self-consistent within our model: in fact, they seem to be among the least stable points in the phase space (see Sec. 5.5 about stability below). What instead obtains at the boundary between the two phases is a typically narrow region where the relative energies of the two states are the same to within the numerical precision: such regions are designated "degenerate" in the phase

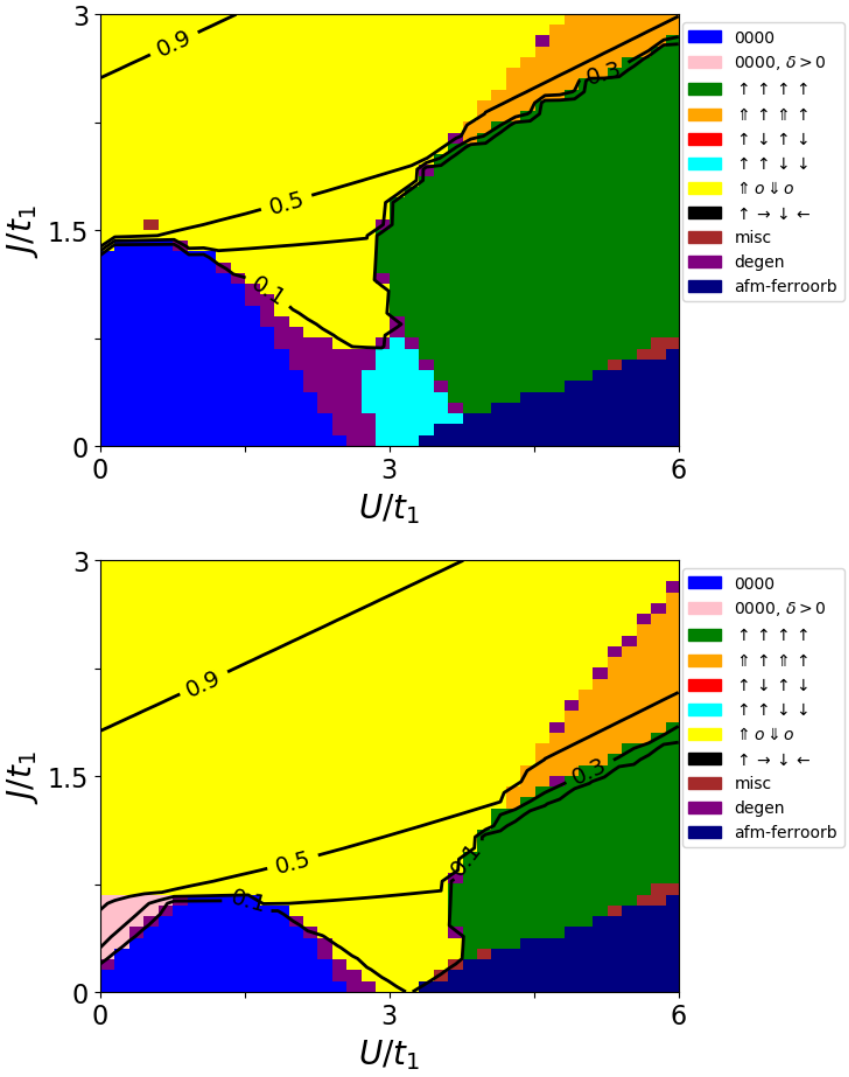

Figure 5.5: Top: U-J phase diagram of magnetic order, in the absence of coupling to the lattice ($\epsilon_b = 0$). Bottom: Same when coupling to the lattice is turned on ($\epsilon_b = 0.8$). Other parameters are $t_1 = 1, t_2 = 0.15, t_4 = 0, \alpha = 1$ for both. The black-line contours indicate the value of charge modulation δ. Resolution is 40×40.

diagram legend. It is possible that the only reason Lee *et al.* saw such a region in the first place was because of their specific technique for carrying out the mean-field approximation by explicitly minimizing the energy as a function of the mean-field parameters (that is, via a parameter search), as opposed to solving the Hartree-Fock equations and looking for self-consistent points. These two techniques, while formally ought to yield the same results, can sometimes involve hidden assumptions and thus not quite produce the same outcomes (as was discussed in Chapter 3).

Aside from the intermediate phase issue, the qualitative agreement is clear (although there are sizable quantitative differences, which we attribute to the somewhat different form of the on-site interaction Hamiltonian $\hat{H}_e$). As the coupling to the lattice is turned up, it is immediately obvious that the charge modulated $\Uparrow 0 \Downarrow 0$ order benefits extraordinarily from it: it expands in reach down to $J = 0$ in some regions, suppressing the equal-sublattice order $\uparrow\uparrow\downarrow\downarrow$ entirely. It also expands across the board, taking over about half of what used to be the metallic phase, and making large gains at the expense of the ferromagnetic phase as well. The charge modulation, however, expands even independently of its associated magnetic order, as is evidenced by the relative growth of the aligned-ferrimagnetic phase $\Uparrow\uparrow\Uparrow\uparrow$.

A curious feature emerges at the leftmost boundary between the metallic and the $\Uparrow 0 \Downarrow 0$ order directly on the $U = 0$ axis: a small phase pocket opens up, with the ground state there exhibiting charge order *without* the usually associated magnetic order $\Uparrow 0 \Downarrow 0$. In effect, the lattice distortion helps decouple the charge and orbital degrees of freedom, which is strongly reminiscent of the behaviour of the heavier rare-earth ions (Sm to Lu) in the traditional nickelate phase diagram. This could be evidence for the dominant role of the lattice coupling during the MIT, and suggests that the strength of the lattice interaction might be responsible for determining whether the MIT and magnetic transitions are concurrent or not. Looking back at the metal-insulator diagrams in Fig. 5.4, we notice that despite acquiring charge density wave character, the ground state for small U is still metallic: despite the strong gapping out of the spectrum and flattening of the bands by the lattice distortion, the Fermi level stays well within the occupied band, so there is no electron localization and magnetic order does not arise.

If we fix charge modulation to the experimentally relevant range $\delta \sim$ 0.3-0.4, we notice that most of the time these contours follow the phase lines between the $\Uparrow 0 \Downarrow 0$ phase and some other phase (metallic for U up to 1.5, ferromagnetic after $U \sim 4$). They, of course, stay on the $\Uparrow 0 \Downarrow 0$ side. However, right in the middle region (the more experimentally

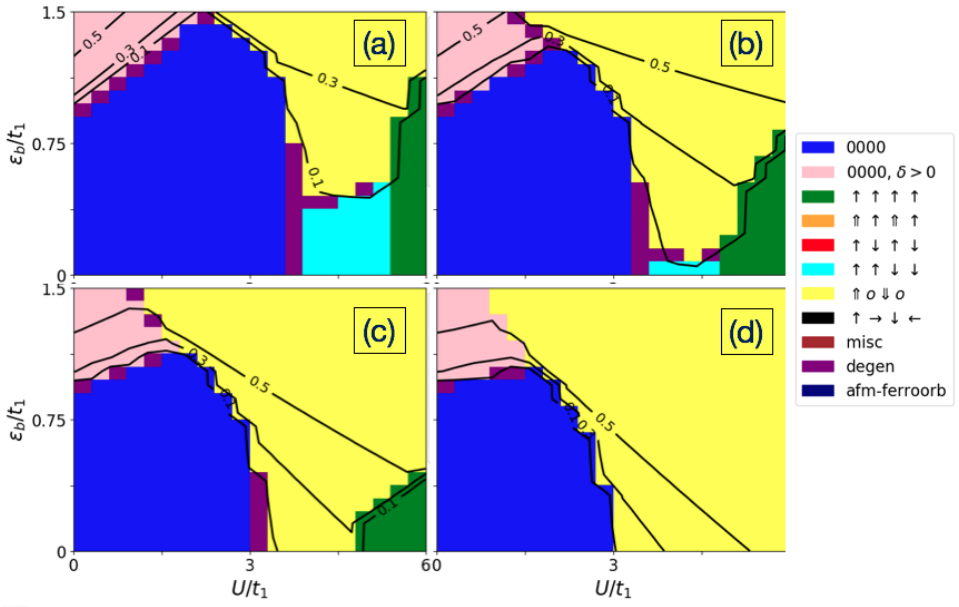

Figure 5.6: Magnetic order in the HF ground state, as a function of U and ϵ_b, for $J/U = 0.2, 0.3$ ((a) and (b), respectively) and $0.4, 0.5$, ((c) and (d), respectively). Other parameters are $t_1 = 1, t_2 = 0.15, t_4 = 0.25, \alpha = 1$.

reasonable values of $U \sim$ 1.5-3) these contours fall squarely into the bulk of the $\Uparrow 0 \Downarrow 0$ phase, suggesting that this indeed could be the dominant 4-site local magnetic alignment for the real system. And this dominance is only enhanced by the coupling to the lattice, as the region of the overall phase diagram occupied by this state grows.

Zooming in once again to specific values for the ratio J/U, we can interrogate the impact of the lattice more closely. Just as we argued from the large-scale diagrams of Fig. 5.5, it is clear from Fig. 5.6 that with the increase of ϵ_b the phase line for the $\Uparrow 0 \Downarrow 0$ order creeps further and further to the left towards smaller U and J values: again the effect is more pronounced for larger ratios J/U. The suppression of the other nontrivial 4-site alignments is also evident with increasing lattice coupling: eventually the only possibilities for the ground state become a charge density wave, with or without magnetic order.

An even more explicit picture of the preference of the lattice for the $\Uparrow 0 \Downarrow 0$ type order can be seen in Fig. 5.7. Here we plot the energies of the various states at a particular set of parameter values relative to the metallic solution 0000, as we sweep ϵ_b: $\Uparrow 0 \Downarrow 0$ emerges a clear winner (and also

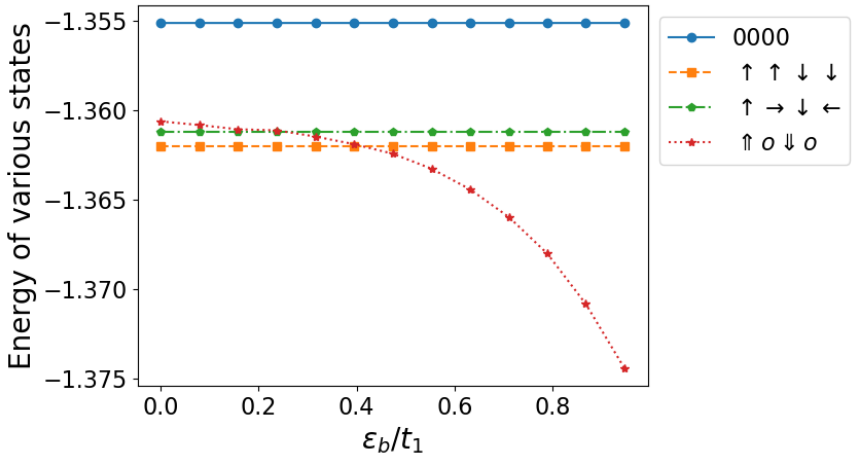

Figure 5.7: Energies of the various converged states (y axis) as a function of ϵ_b (x axis). The parameters are $U = 3.158, J = 0.2U, t_1 = 1, t_2 = 0.15, t_4 = 0.25$. Resolution is 20×20.

the only one responsive to the presence of the lattice). While this plot is made at a specific set of parameter values, this pattern seems to hold across various parameter regimes of U, J, t_i, as is evidenced by the magnetic phase diagrams where $\Uparrow 0 \Downarrow 0$ phase conquers an ever-larger area with increasing ϵ_b. What is curious about these plots at a first glance is that relative to the 0000 state, none of the states' energies are affected by changing ϵ_b, aside from $\Uparrow 0 \quad \Downarrow 0$. But there is a straightforward explanation to this: any state that includes no charge disproportionation also includes no lattice distortion, as $\delta \sim u$ through the lattice self-consistency equation 3.5. Thus changing ϵ_b has no effect neither in the total energy nor in the Hartree-Fock Hamiltonian, as it always enters in the combination $\epsilon_b u$. The real question is: why are the states with partial charge disproportionation, *e.g.* $\Uparrow\uparrow\Downarrow\downarrow$ not convergent within this mean-field model? Such states could potentially compete with $\Uparrow 0 \Downarrow 0$ order for ground state status, as the coupling to the lattice is cranked higher. It is a fact, however, that such states are not only not convergent during the iterations no matter the starting point, but in fact they are among the least stable (this is discussed more in Sec. 5.5).

5.3 Impact of the hopping integrals

One clear impact of adjusting the hopping integrals t_i is to affect the overall bandwidth W, defined in the usual way as the difference between the largest and the smallest Hartree-Fock eigenvalues at zero interaction ($U = J = \epsilon_b = 0$). We know from numerous studies of the single-band Hubbard model that the parameter that results in the onset of Mott insulator phase is the ratio of the interaction strength to the bandwidth, U/t (U/W with W the total bandwidth if more than one hopping pathway is present): thus one could anticipate changes to the phase diagram when any of the hopping rates t_i increase enough so as to change W significantly.

On experimental grounds, however, given the spatial extent of the nickelate orbitals, it is unrealistic to expect the farther-neighbour hopping t_2, t_4 to be larger or even same magnitude as the nearest neighbour t_1. The analysis of Lee *et al.* put the rate t_2 somewhere in the range $\approx$ 0.05-0.15t_1 for best agreement with LDA calculations and Fermi surface measurements [26]: thus we can reasonably restrict $t_2, t_4 < 0.3$. However, the bandwidth changes by at most %10 for this range of values, which should lead to only modest shifts of the phases in the diagram.

Yet we observe much more dramatic effects than could be expected on the basis of bandwidth renormalization. Looking to Fig. 5.8, where a magnetic phase diagram in the U–J plane is produced for varying levels of the second-nearest neighbour hopping ($t_2 = 0, 0.1, 0.25$), we notice a profound change of the phase boundaries. Moreover, this change *favours* ferromagnetism, in spite of the increasing bandwidth, which would be expected to push the insulating boundary to larger U. Looking to Fig. 5.10 with $t_4 = 0, 0.1, 0.25, 0.35$, the opposite effect is observed: a change for the metallic region that is way beyond the meager %10-%15 one could expect based on the U/W Mott picture. Instead, it appears that the shape, rather than the width, of the DOS is to blame: both t_2 and t_4 hopping pathways affect the lop-sidedness of the distribution strongly even when the overall width is barely renormalized, a phenomenon noted in the literature on Hubbard models [79].

Both the t_1 and t_4 hopping pathways appear to produce a symmetric (about the midpoint) DOS: this is not entirely surprising, given that t_4 has exactly the same hopping coefficients, just with the lattice constant being $2a$. The t_2 hopping, on the other hand, is different, producing an asymmetric DOS: even a small positive t_2 value leads to a pile-up of DOS weight towards the lower band edge (see Fig. 5.9). This extra weight, known as a van Hove singularity, increases the DOS at the Fermi level (given that at quarter-filling the Fermi level is in the lower quartile of the distribution). One

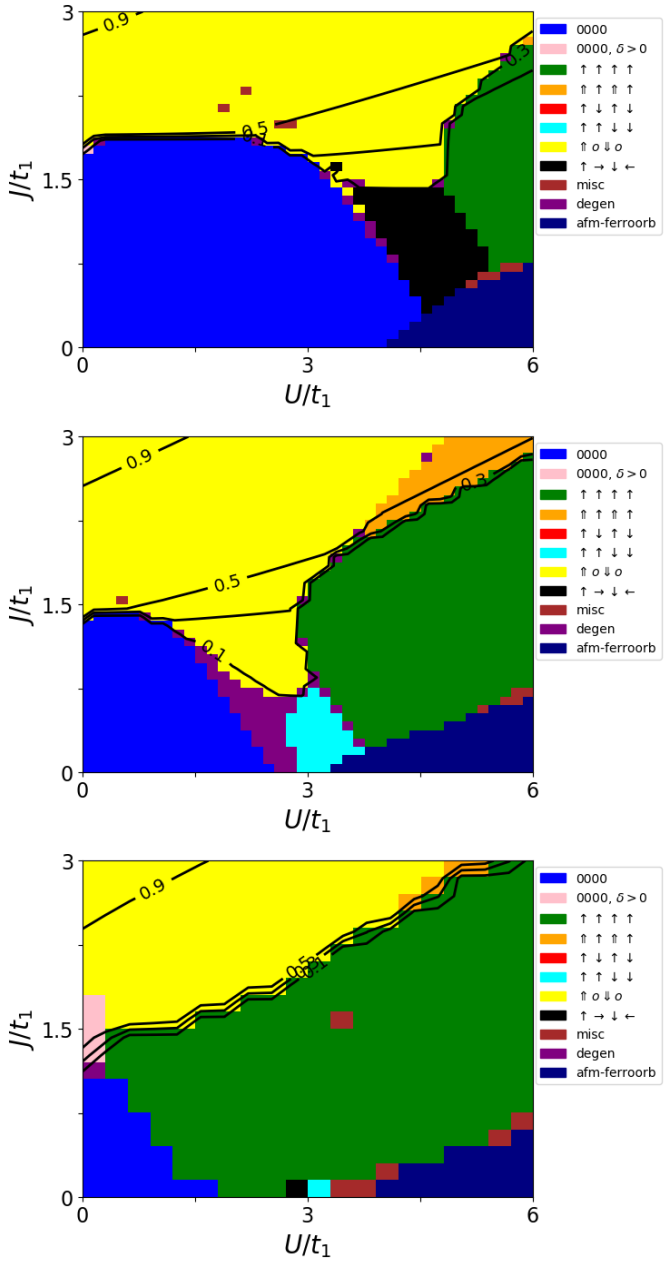

Figure 5.8: Magnetic order in the HF ground state, as a function of U and J, for $t_2 = 0, 0.15, 0.25$ (top to bottom). Other parameters are $t_1 = 1, t_4 = 0, \epsilon_b = 0$.

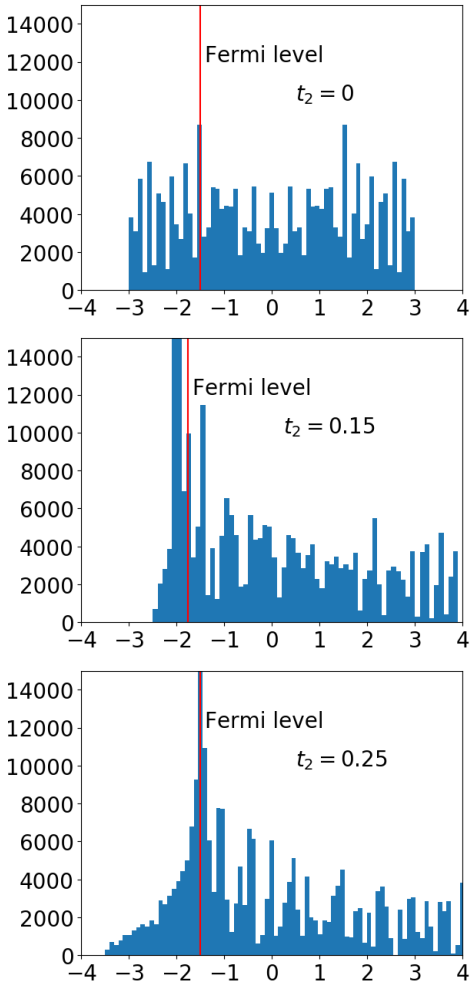

Figure 5.9: The non-interacting ($U = J = 0$) DOS, corresponding to the systems in Fig.5.8. Notice that increasing the bandwidth (even if just modestly by at most %15), paradoxically, leads to more robust ferromagnetism at *lower* U — a consequence of the van Hove singularity at the lower band edge. Also notice how when the next-nearest neighbour frustration is maximally reduced ($t_2 = 0$), the non-collinear 4-site magnetic order dominates the collinear one. Currently it is not clear to us why this would be the case, given how introducing t_2, t_4 seems to affect them equally based on pure lattice frustration arguments.

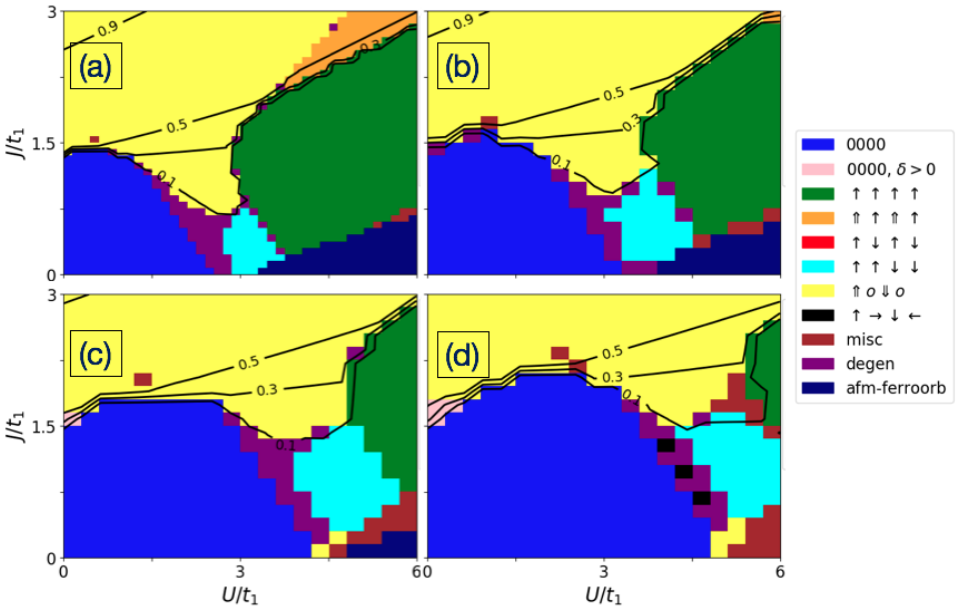

Figure 5.10: Magnetic order in the HF ground state, as a function of U and J, for $t_4 = 0, 0.1$ ((a) and (b), respectively), and $t_4 = 0.25, 0.35$ ((c) and (d)). The bandwidth is $W = 6.4$ in all cases. Other parameters are $t_1 = 1, t_2 = 0.15, \epsilon_b = 0$. The growth of the metallic region is clearly not the effect of a renormalized bandwidth, but rather due to the changes of the shape of the DOS.

well-known pathway to ferromagnetism is the Stoner criterion [80]: derived within the Hubbard model, it says that ferromagnetism can spontaneously arise in an electronic system when the condition $UD(E_F) > 1$ is met ($D(E_F)$ is the density of states at the Fermi level). This condition is derived for a different Hubbard model than the one employed here: however, it appears to be consistent with that we observe. The increase/decrease in the density of states at the Fermi level with the changes of t_2, t_4 is on the order of %30-40, much more commensurate with the observed shifts of the phase boundaries in Figs. 5.8,5.10. In particular, t_2 acts to increase the DOS at the Fermi level: this means U (or some effective measure of the electron-electron interactions) at which ferromagnetism sets in can be significantly lower. Conversely, increasing t_4 has the effect of boosting the DOS above the Fermi level, thus depleting it at the Fermi level and increasing the U required to set off ferromagnetism. This kind of behaviour is consistent with what has been seen before with regards to the next-nearest neighbour hopping [79].

Despite the seemingly strong impact of the hopping rates on the magnetic phase diagram, it appears that it almost does not affect the energy of the 4-site states. Fig. 5.11 shows how the energies of the three main 4-site contenders $\Uparrow 0 \Downarrow 0$, $\uparrow\uparrow\downarrow\downarrow$ and $\uparrow\rightarrow\downarrow\leftarrow$ scale with varying t_2 and t_4. These plots represent the trend that is observed across most of the parameter regimes: that the hopping rates generally do not affect the **energy order** of the various 4-site magnetic states, rather they modulate their energies more or less equally. This can be generally understood from frustration cost arguments: the added frustration introduced by a nonzero t_4 is identical for all the three candidates. For t_2 the effect is slightly more complicated, as increasing it actually brings down the energy for all of the magnetic states: we believe this should be seen in light of the Stoner criterion which benefits all kinds of magnetic order, but prefers ferromagnetism above all else. Unlike t_4, increasing t_2 actually does show a preference for magnetic orders: namely it prefers collinear orders like $\Uparrow 0 \Downarrow 0$ and $\uparrow\uparrow\downarrow\downarrow$ above the non-collinear version $\uparrow\rightarrow\downarrow\leftarrow$ – however, its preference for ferromagnetism reigns above all else. Conversely, the frustration costs from t_4 are strongest in ferromagnets, as can be seen by the steep increase in energy for the ferromagnetic state in Fig. 5.11. Once again, we would like to point out that these effects are all purely a consequence of the shape of the DOS, as the bandwidth is barely renormalized (see Fig. 5.8).

Another small caveat to the notion that the relative standing of the various 4-site candidates is unaffected by the various hopping rates is the emergence of the non-collinear $\uparrow\rightarrow\downarrow\leftarrow$ state as the ground state in what

used to be the $\uparrow\uparrow\downarrow\downarrow$ domain at $t_2 = 0$, visible in the top panel in Fig. 5.8. This phenomenon is still not entirely clear to us and is to be studied further in a later work: however, the fact that it only happens when $t_2 = 0$ and is washed out at all other values of the hopping rates suggests that it is an isolated phenomenon and should not affect the general discussion of the ground state in rare-earth nickelates.

5.4 The anharmonicity parameter α

Throughout this work the value $\alpha = 1$ was mostly used during the calculations: however, it is certainly important to reflect on the impact of this additional parameter in our model. Looking at the form of the lattice energy for the typical value of the distortion $u = 0.5$,

$$E_{\text{latt}} = \epsilon_b(u_i^2 + \alpha u_i^4/2) \sim \epsilon_b(0.25 + 0.03\alpha),$$

we observe that the anharmonic contribution for $\alpha = 1$ is merely %10 of the total value of the lattice energy. Hence its main impact is to renormalize the ground state distortion value u away from the identity $u = \delta$, as per the self-consistency equation 3.5,

$$u_j + a u_j^3 + 1 = \langle n_j \rangle_{\Psi_e},$$

without affecting the physics of the problem. An example calculation for a fixed ratio $J/U = 0.2$ in Fig. 5.12 supports this intuition: there is only a moderate displacement of the phase boundaries with the anharmonicity parameter going from $\alpha = 0$ to $\alpha = 1$, with the main change being the shift of the charge modulation δ contours. And it is mostly the contours for largest δ (i.e. largest u) that are significantly displaced, as could be expected from the energy scale comparisons above. In the interest of controlling the magnitude of the lattice distortion u, we employ $\alpha = 1$ throughout most of the calculation in this thesis.

5.5 Convergence and stability

It should be noted that many of these magnetic orders, excluding perhaps the $\Uparrow 0 \Downarrow 0$ state, are very unstable numerically. Consider the no disproportionation collinear state $\uparrow\uparrow\downarrow\downarrow$. In our model it will have (for example) the following mean-field description,

$$\delta, S_{\text{FM}}, S_{\text{AFM}}, S_{1\text{x}}, S_{2\text{x}} = 0, \quad S_{1\text{z}} = S_{2\text{z}} \neq 0.$$

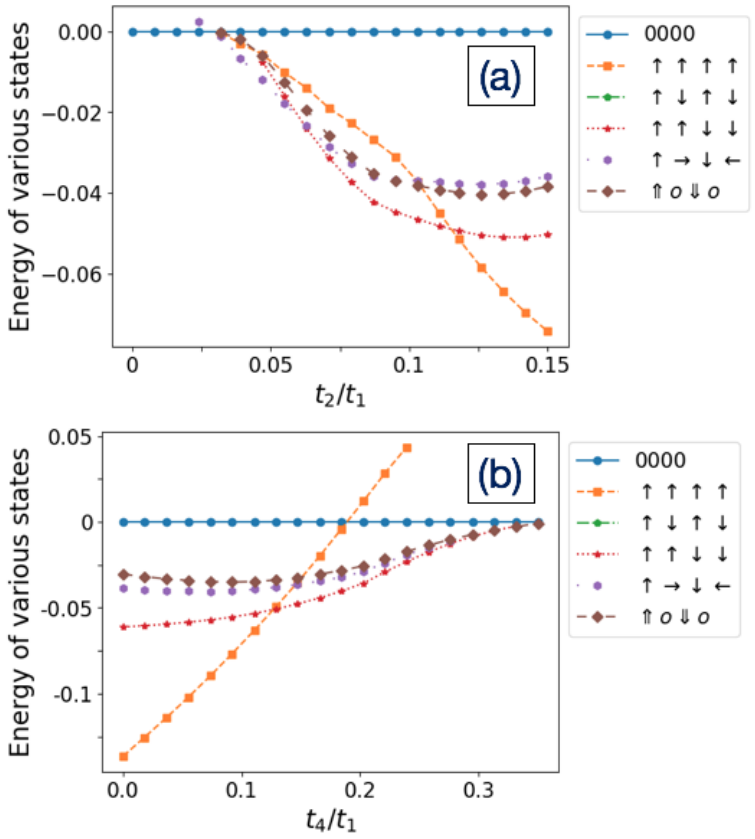

Figure 5.11: Energies of several converged self-consistent HF states as a function of t_4, *relative to* the energy of the metallic state. The different colours correspond to different magnetic orders (see the legend). The parameters are $U = 4, J = 0.316, t_1 = 1, t_4 = 0, \epsilon_b = 0$ for (a) and $U = 5, J = 0.316, t_1 = 1, t_2 = 0.15, \epsilon_b = 0$ for (b). Notice how in (b) the relative energies of the chief magnetic ground state contenders are not affected by the change in the hopping rate t_4 – except for ferromagnetism, which gets strongly frustrated with the additional t_4 hopping and, paradoxically, "unfrustrated" with the introduction of t_2 hopping due to DOS effects (see the text for details). Meanwhile, in (a) with tuning the t_2 rate away from 0 the non-collinear ↑→↓← gets briefly favoured, but then quickly loses out to the collinear ↑↑↓↓, before ferromagnetism begins to reign supreme.

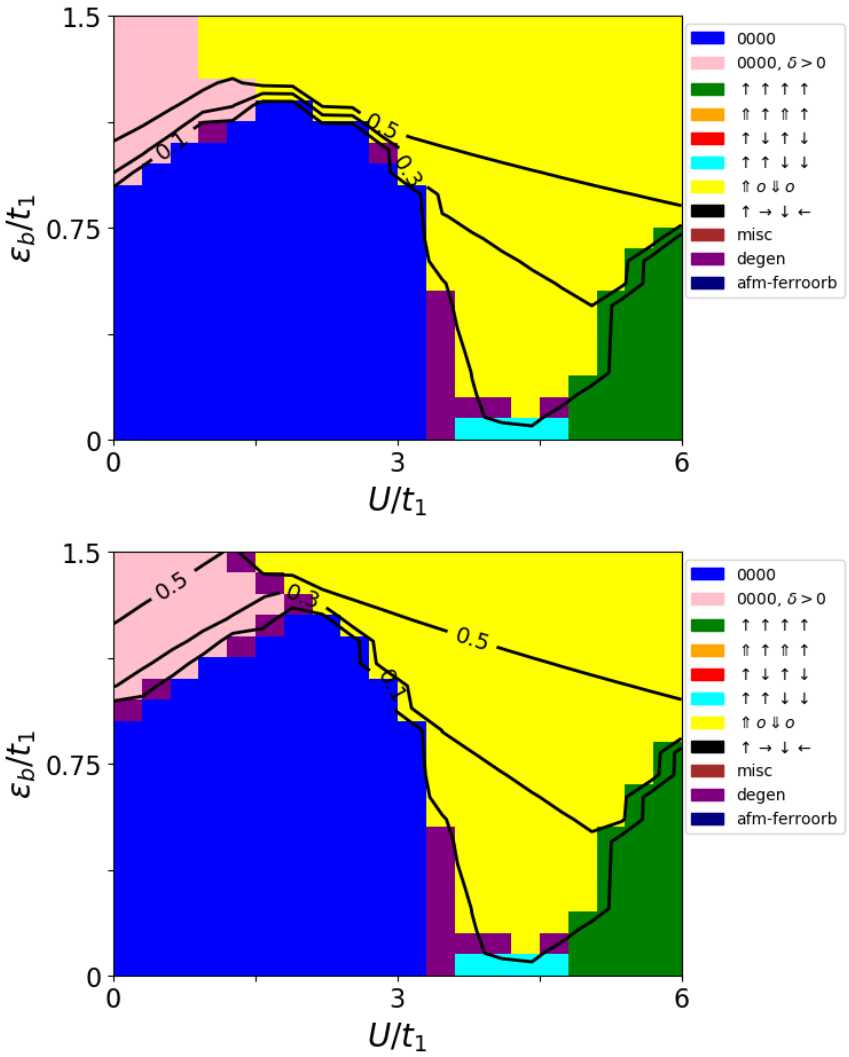

Figure 5.12: Magnetic order in the HF ground state, as a function of U and ϵ_b, for $J/U = 0.2$, and two different values of the anharmonicity α: $\alpha = 0$ (top) and $\alpha = 1$ (bottom). Other parameters are $t_1 = 1, t_2 = 0.15, t_4 = 0.25$.

To make a reasonable guess for its convergence, we might guess $S_{1z} = S_{2z} = 0.5$, and all other parameters zero. Then we usually get the desired state. However, if there is even a slight deviation from either perfect symmetry between the sublattices ($S_{1z} \neq S_{2z}$), or a small non-zero δ, or a different parameter ($O_1, Z_4, S_{FM}, ...$) being nonzero, most likely the iterations would run away from the solution of the desired type. Sometimes there are lines of stability, along which deviations generally do not result in catastrophic runaway, but there never are any sizable convergence basins for most of the states on the list 5.2. In fact, iteration divergence occured (before the introduction of the Pulay mixing method) even if the iterations simply took too long: the accumulated numerical errors after a sufficiently large number of iterations automatically result in some of the other parameters becoming non-zero, which causes runaway effects and the desired solution is not obtained. This can be seen most clearly from cuts in the 15-dimensional parameter space that show iterative trajectories of the Hartree-Fock calculation (such diagrams are called "Poincare sections" in the dynamical systems literature). In Fig. 5.13, we plot the difference $S_{1z} - S_{2x}$ versus the charge disproportionation δ during the iterative process, as the algorithm searches for the solution to the Hartree-Fock equations. Both $\uparrow\rightarrow\downarrow\leftarrow$ and $\Uparrow 0 \Downarrow 0$ are well-defined points in this plane, corresponding to $S_{1z} = S_{2z}$ and one of the S being zero, respectively. The intermediate state $\Uparrow\rightarrow\Downarrow\leftarrow$ would then lie somewhere on the diagonal, between the two. From the iterative trajectories, we can see that any solution not already on the $S_{1z} - S_{2z} = 0$ line (the y-axis) converges to $\Uparrow 0 \Downarrow 0$ instead: and the intermediate type states on the diagonal have some of the fastest decay toward the $\Uparrow 0 \Downarrow 0$ states out there.

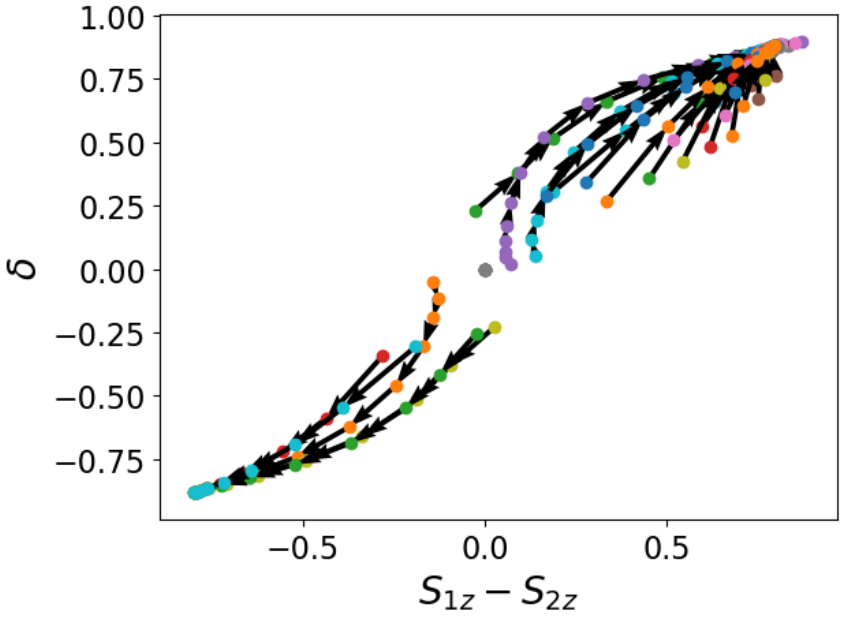

Figure 5.13: A phase portrait of the iterative sequences for various starting parameters in the δ, S_{1z}, S_{2z} parameter subspace. On the x axis we plot the difference between the spin parameters of the sublattices, $S_{1z} - S_{2z}$: hence the perfect symmetry point is at the origin. On the y axis is the disproportionation parameter δ: the stable point $\Uparrow 0 \Downarrow 0$ is thus at the top right and equivalently bottom left. The parameters are $U = 1.5, J = 3, t_1 = 1, t_2 = 0.15, t_4 = 0.55, \epsilon_b = 0$. Despite the relatively dense sampling of the phase space, the $\Uparrow 0 \Downarrow$ attractors dominate the dynamics, with no other states, specifically of the partially disproportionated kind $\Uparrow\uparrow\Downarrow\downarrow$, being convergent.

Chapter 6

Conclusions

> What we call the beginning is often the end. And to make an end is to make a beginning. The end is where we start from.
>
> T. S. Eliot (1942)

Rare-earth nickelates, ever since being synthesized in the early 70s, have presented us with numerous fascinating puzzles that speak to various areas of condensed matter physics. While the questions about its crystal structure and the lattice distortion across the MIT phase boundary are considered largely settled, the conversations surrounding the MIT itself – including its precise mechanism and physical manifestation vis-á-vis the orbital structure in the Ni-O cages – as well as questions about the nature of the magnetic order at low temperatures and its interrelation to charge and lattice degrees of freedom, are still ongoing. In this thesis we focussed our efforts on investigating the relationship between the lattice distortions in the material and the charge/magnetic order found at low temperatures. Our approach was to construct an effective two-band Hubbard model, based on the phenomenology of the material that is known from experiments, that focusses on the nominally degenerate e_g doublet of the Ni outer electron subshell. We included first, second and fourth neighbour hopping, and incorporated the electron-electron interactions in the two-band context in the usual way – by employing the Kanamori Hamiltonian. The lattice was introduced semiclassically, characterized by a single scalar u representing the largely isotropic distortion of the Ni-O octahedral cage: it was coupled to the electrons through a Holstein-like on-site term. The final model ends up having 7 independent adjustable parameters: the electron-electron interaction strengths U, J, the hopping amplitudes t_1, t_2, t_4, the lattice energy scale ϵ_b and anharmonicity α.

Upon constructing the model, we applied the Hartree-Fock approximation and solved the resulting Hartree-Fock equations to obtain the expected ground state of the model at zero temperature. Studying the ground state

in a variety of slices of the high-dimensional parameter space, we were able to confirm that the net effect of the electron-phonon coupling on the electronic behaviour – even in this simple semiclassical model for the lattice – is to encourage the formation of insulating charge order, just as found by earlier investigators [32]. With the increase of the lattice coupling strength ϵ_b, we found that the area of phase diagrams occupied by the phase with charge order increases dramatically, as the order becomes more energetically favourable: in this simple model the charge order is most closely identified with that of a charge density wave type $\mathrm{Ni}^{3+\delta}\mathrm{Ni}^{3-\delta}$, as described in Sec. 1.4.3, although effective parallels can be drawn with the negative-charge transfer picture as well, as discussed briefly during the construction of the model in Ch. 2.

Next we proceeded to interrogate the magnetic behaviour of the nickelates within our model. It turns out there is a great variety of states that are self-consistent within the model: the relevant ones are those that are lowest in total energy. We identified several 4-site self-consistent candidate states that could fit the experimentally observed wavevector $\mathbf{Q}_m = (\frac{2\pi}{a})(\frac{1}{4}, \frac{1}{4}, \frac{1}{4})$: these include $\Uparrow 0 \Downarrow 0$, $\uparrow\uparrow\downarrow\downarrow$, and $\uparrow\rightarrow\downarrow\leftarrow$. Even without the coupling to the lattice, for most hoppings t_i and a wide range of the electron-electron interaction parameters U, J, the $\Uparrow 0 \Downarrow 0$ state emerges as the dominant ground state. The two other candidates only arise at intermediate U and small J and zero lattice coupling ϵ_b, and do not fare well when the lattice coupling is increased, quickly ceding their entire phase space to the $\Uparrow 0 \Downarrow 0$. This sort of behaviour makes sense in light of the fact that the states $\uparrow\uparrow\downarrow\downarrow$, and $\uparrow\rightarrow\downarrow\leftarrow$ cannot couple to the lattice distortion, given that they have perfect sublattice symmetry and no charge disproportionation: and if $\delta = 0$, then the self-consistency condition for the lattice degree of freedom demands the lattice distortion also vanish $u = 0$. So while these two states are unaffected by the presence of the lattice, the state $\Uparrow 0 \Downarrow 0$ can couple to the distortions and lower its energy, thus becoming the favoured ground state.

In principle one could imagine states with only partial charge disproportionation, say of type $\Uparrow\rightarrow\Downarrow\leftarrow$, emerging within the model to compete energetically with the fully disproportionated state $\Uparrow 0 \Downarrow 0$. However, that does not seem to happen within our model: we never find such states among the self-consistent solutions. In fact, if we follow the iterative trajectories during the solution of the Hartree-Fock equations and start with initial guesses close to such a partially disproportionated order, such points appear among the least stable in the phase space, the solution quickly diverging away either to the metallic 0000 state or to the $\Uparrow 0 \Downarrow 0$ one.

During this study, an unexpected new feature emerged in the phase dia-

gram when the lattice coupling ϵ_b was turned on: a novel phase wherein the charge density wave ($\delta \neq 0$) appeared without the accompanying magnetic order $\Uparrow 0 \Downarrow 0$. This de-coupling of the charge and magnetic transitions in the phase diagram appears to be mediated by the electron-phonon coupling: the energy decrease afforded by the charge disproportionation is reinforced by the lattice distortion so far so as to make the additional appearance of the magnetic order (and simultaneously the onset of insulating behaviour) unfavourable. This feature is strongly reminiscent of the well-known phenomenon in the nickelates where the MIT and the magnetic transition occur at different temperatures, $T_{\mathrm{MIT}} > T_{\mathrm{N}}$, for all the nickelates from Eu to Lu, leaving out only the lightest rare-earth ions Pr and Nd, for which $T_{\mathrm{MIT}} = T_{\mathrm{N}}$. The observation that this decoupling can be brought on by the electron-phonon coupling even in this simple model further underscores the importance of the lattice degrees of freedom and could potentially be seen as an explanation of the phenomenon, given that the lattice coupling strength can be expected to increase for the heavier rare-earth ions.

However, plenty of open questions remain. For one, the negative charge transfer picture of the MIT in the nickelates calls for the involvement of the oxygen $2p$ bands in the model: it is unclear to what extent the variation of the hopping and interaction parameters can capture the effects of introducing the oxygen bands. Moreover, the Hartree-Fock approximation does not take into account any correlation effects (aside from Pauli's exclusion principle): while it is generally believed that the effects of correlation in the nickelates are not very important, it would still be useful to check this explicitly, *e.g.* via a dynamical mean-field theory (DMFT) approach.

Aside from the questions about the applicability of the model and the accuracy of the Hartree-Fock approximation, even within our study there are a few ideas that can be pursued further. For instance, a clear understanding of the orbitally ordered state (the antiferromagnetic disproportionated-ferroorbital state) that obtains at intermediate to high values of U in the magnetic order phase diagrams would be very valuable, along with other orbitally ordered states, especially considering that there have been no signs of any orbital order in most experimental studies.

Overall, while we have made significant strides in addressing the question of the impact of the electron-phonon coupling on the charge and magnetic order in the nickelates, further work, using more detailed Hamiltonians and more accurate approximations, is required before the matter is fully put to rest.

Bibliography

[1] J. Varignon, M. N. Grisolia, J. Íñiguez, A. Barthélémy, and M. Bibes, "Complete phase diagram of rare-earth nickelates from first-principles," *npj Quantum Materials*, vol. 2, p. 21, December 2017.

[2] A. Hampel, P. Liu, C. Franchini, and C. Ederer, "Energetics of the coupled electronic–structural transition in the rare-earth nickelates," *npj Quantum Materials*, vol. 4, p. 5, December 2019.

[3] M. L. Medarde, "Structural, magnetic and electronic properties of perovskites (R = rare earth)," *Journal of Physics: Condensed Matter*, vol. 9, pp. 1679–1707, February 1997.

[4] G. Catalan, "Progress in perovskite nickelate research," *Phase Transitions*, vol. 81, pp. 729–749, July 2008.

[5] P. V. Balachandran and J. M. Rondinelli, "Interplay of octahedral rotations and breathing distortions in charge-ordering perovskite oxides," *Physical Review B*, vol. 88, p. 054101, August 2013.

[6] X. Granados, J. Fontcuberta, X. Obradors, and J. B. Torrance, "Metastable metallic state and hysteresis below the metal-insulator transition in $PrNiO_3$," *Physical Review B*, vol. 46, pp. 15683–15688, December 1992.

[7] E. Pavarini, "Crystal-Field Theory, Tight-Binding Method, and Jahn-Teller Effect," in *Correlated Electrons: From Models to Materials* (E. Pavarini, E. Koch, F. Anders, and M. Jarrell, eds.), ch. 6, pp. 147–187, Forschungszentrum Jülich: Forschungszentrum Jülich GmbH Institute for Advanced Simulation, 2012.

[8] G. Sawatzky and R. Green, "The Explicit Role of Anion States in High-Valence Metal Oxides," in *Quantum Materials: Experiments and Theory* (E. Pavarini, E. Koch, J. Van Den Brink, and G. Sawatzky, eds.), vol. 6, ch. 1, pp. 1–36, Forschungszentrum Jülich: Forschungszentrum Jülich GmbH Institute for Advanced Simulation, 2016.

[9] A. Muñoz, J. Alonso, M. Martínez-Lope, and M. Fernández-Díaz, "On the magnetic structure of $DyNiO_3$," *Journal of Solid State Chemistry*, vol. 182, pp. 1982–1989, July 2009.

[10] I. B. Bersuker, *Electronic Structure and Properties of Transition Metal Compounds*. Hoboken, NJ, USA: John Wiley & Sons, Inc., April 2010.

[11] N. A. Spaldin, "Multiferroics: Past, present, and future," *MRS Bulletin*, vol. 42, pp. 385–390, May 2017.

[12] G. Giovannetti, S. Kumar, D. Khomskii, S. Picozzi, and J. van den Brink, "Multiferroicity in Rare-Earth Nickelates $R\mathrm{NiO}_3$," *Physical Review Letters*, vol. 103, p. 156401, October 2009.

[13] J. F. Scott, "Multiferroic memories," *Nature Materials*, vol. 6, pp. 256–257, April 2007.

[14] G. Demazeau, A. Marbeuf, M. Pouchard, and P. Hagenmuller, "Sur une série de composés oxygènes du nickel trivalent derivés de la perovskite," *Journal of Solid State Chemistry*, vol. 3, pp. 582–589, November 1971.

[15] J. G. Bednorz and K. A. Müller, "Possible high T_c superconductivity in the Ba-La-Cu-O system," *Zeitschrift für Physik B Condensed Matter*, vol. 64, pp. 189–193, June 1986.

[16] J. Torrance, P. Lacorre, A. Nazzal, E. Ansaldo, and C. Niedermayer, "Systematic study of insulator-metal transitions in perovskites $R\mathrm{NiO}_3$ (R=Pr,Nd,Sm,Eu) due to closing of charge-transfer gap," *Physical Review B*, vol. 45, pp. 8209–8212, April 1992.

[17] J. B. Torrance, P. Lacorro, C. Asavaroengchai, and R. M. Metzger, "Simple and perovskite oxides of transition-metals: Why some are metallic, while most are insulating," *Journal of Solid State Chemistry*, vol. 90, pp. 168–172, January 1991.

[18] T. Mizokawa, D. I. Khomskii, and G. A. Sawatzky, "Spin and charge ordering in self-doped Mott insulators," *Physical Review B*, vol. 61, pp. 11263–11266, May 2000.

[19] H. Park, A. J. Millis, and C. A. Marianetti, "Site-Selective Mott Transition in Rare-Earth-Element Nickelates," *Physical Review Letters*, vol. 109, p. 156402, October 2012.

[20] B. Lau and A. J. Millis, "Theory of the Magnetic and Metal-Insulator Transitions in $R\mathrm{NiO}_3$ Bulk and Layered Structures," *Physical Review Letters*, vol. 110, p. 126404, March 2013.

[21] D. Puggioni, A. Filippetti, and V. Fiorentini, "Ordering and multiple phase transitions in ultrathin nickelate superlattices," *Physical Review B*, vol. 86, p. 195132, November 2012.

[22] A. D. Caviglia, R. Scherwitzl, P. Popovich, W. Hu, H. Bromberger, R. Singla, M. Mitrano, M. C. Hoffmann, S. Kaiser, P. Zubko, S. Gariglio, J.-M. Triscone, M. Först, and A. Cavalleri, "Ultrafast Strain Engineering in Complex Oxide Heterostructures," *Physical Review Letters*, vol. 108, p. 136801, March 2012.

[23] J. L. García-Muñoz, J. Rodríguez-Carvajal, P. Lacorre, and J. B. Torrance, "Neutron-diffraction study of $R\mathrm{NiO}_3$ (R = La,Pr,Nd,Sm): Electronically induced structural changes across the metal-insulator transition," *Physical Review B*, vol. 46, pp. 4414–4425, August 1992.

[24] H. Guo, Z. W. Li, L. Zhao, Z. Hu, C. F. Chang, C.-Y. Kuo, W. Schmidt, A. Piovano, T. W. Pi, O. Sobolev, D. I. Khomskii, L. H. Tjeng, and A. C. Komarek, "Antiferromagnetic correlations in the metallic strongly correlated transition metal oxide LaNiO_3," *Nature Communications*, vol. 9, p. 43, December 2018.

[25] K. Haule and G. L. Pascut, "Mott Transition and Magnetism in Rare Earth Nickelates and its Fingerprint on the X-ray Scattering," *Scientific Reports*, vol. 7, p. 10375, December 2017.

[26] S. Lee, R. Chen, and L. Balents, "Metal-insulator transition in a two-band model for the perovskite nickelates," *Physical Review B*, vol. 84, 2011.

[27] V. Scagnoli, U. Staub, A. M. Mulders, M. Janousch, G. I. Meijer, G. Hammerl, J. M. Tonnerre, and N. Stojic, "Role of magnetic and orbital ordering at the metal-insulator transition in NdNiO_3," *Physical Review B*, vol. 73, p. 100409, March 2006.

[28] Y. Lu, D. Betto, K. Fürsich, H. Suzuki, H.-H. Kim, G. Cristiani, G. Logvenov, N. B. Brookes, E. Benckiser, M. W. Haverkort, G. Khaliullin, M. Le Tacon, M. Minola, and B. Keimer, "Site-Selective Probe of Magnetic Excitations in Rare-Earth Nickelates Using Resonant Inelastic X-ray Scattering," *Physical Review X*, vol. 8, 2018.

[29] X. Obradors, L. M. Paulius, M. B. Maple, J. B. Torrance, A. I. Nazzal, J. Fontcuberta, and X. Granados, "Pressure dependence of the metal-insulator transition in the charge-transfer oxides $R\mathrm{NiO_3}$ (R = Pr,Nd, $\mathrm{Nd_{0.7}\,La_{0.3}}$)," *Physical Review B*, vol. 47, pp. 12353–12356, May 1993.

[30] M. Hepting, *Ordering Phenomena in Rare-Earth Nickelate Heterostructures*. Springer Theses, Cham: Springer International Publishing, 2017.

[31] M. Medarde, P. Lacorre, K. Conder, F. Fauth, and A. Furrer, "Giant ^{16}O-^{18}O Isotope Effect on the Metal-Insulator Transition of $R\mathrm{NiO_3}$ Perovskites (R = Rare Earth)," *Physical Review Letters*, vol. 80, pp. 2397–2400, March 1998.

[32] S. Johnston, A. Mukherjee, I. Elfimov, M. Berciu, and G. A. Sawatzky, "Charge Disproportionation without Charge Transfer in the Rare-Earth-Element Nickelates as a Possible Mechanism for the Metal-Insulator Transition," *Physical Review Letters*, vol. 112, p. 106404, March 2014.

[33] A. Wold, B. Post, and E. Banks, "Rare Earth Nickel Oxides," *Journal of the American Chemical Society*, vol. 79, pp. 4911–4913, September 1957.

[34] V. M. Goldschmidt, "Die Gesetze der Krystallochemie," *Die Naturwissenschaften*, vol. 14, pp. 477–485, May 1926.

[35] J. A. Alonso, M. J. Martínez-Lope, M. T. Casais, J. L. García-Muñoz, and M. T. Fernández-Díaz, "Room-temperature monoclinic distortion due to charge disproportionation in $R\mathrm{NiO_3}$ perovskites with small rare-earth cations (R = Ho, Y, Er, Tm, Yb and Lu): A neutron diffraction study," *Physical Review B*, vol. 61, pp. 1756–1763, January 2000.

[36] M. Medarde, M. T. Fernández-Díaz, and P. Lacorre, "Long-range charge order in the low-temperature insulating phase of $\mathrm{PrNiO_3}$," *Physical Review B*, vol. 78, p. 212101, December 2008.

[37] J. L. García-Muñoz, M. A. G. Aranda, J. A. Alonso, and M. J. Martínez-Lope, "Structure and charge order in the antiferromagnetic band-insulating phase of $\mathrm{NdNiO_3}$," *Physical Review B*, vol. 79, p. 134432, April 2009.

[38] J. Rodríguez-Carvajal, S. Rosenkranz, M. Medarde, P. Lacorre, M. T. Fernandez-Díaz, F. Fauth, and V. Trounov, "Neutron-diffraction study

of the magnetic and orbital ordering in $SmNiO_3$," *Physical Review B*, vol. 57, pp. 456–464, January 1998.

[39] A. Hampel and C. Ederer, "Interplay between breathing mode distortion and magnetic order in rare-earth nickelates $R\mathrm{NiO}_3$ within DFT+U," *Physical Review B*, vol. 96, p. 165130, October 2017.

[40] J. M. Perez-Mato, D. Orobengoa, and M. I. Aroyo, "Mode crystallography of distorted structures," *Acta Crystallographica Section A Foundations of Crystallography*, vol. 66, pp. 558–590, September 2010.

[41] J.-S. Zhou and J. B. Goodenough, "Chemical bonding and electronic structure of $R\mathrm{NiO}_3$ (R = rare earth)," *Physical Review B*, vol. 69, p. 153105, April 2004.

[42] J. A. Alonso, J. L. García-Muñoz, M. T. Fernández-Díaz, M. A. G. Aranda, M. J. Martínez-Lope, and M. T. Casais, "Charge Disproportionation in $R\mathrm{NiO}_3$ Perovskites: Simultaneous Metal-Insulator and Structural Transition in $YNiO_3$," *Physical Review Letters*, vol. 82, pp. 3871–3874, May 1999.

[43] U. Staub, G. I. Meijer, F. Fauth, R. Allenspach, J. G. Bednorz, J. Karpinski, S. M. Kazakov, L. Paolasini, and F. D'Acapito, "Direct Observation of Charge Order in an Epitaxial $NdNiO_3$ Film," *Physical Review Letters*, vol. 88, p. 126402, March 2002.

[44] C. Johan, *Introduction to ligand field theory*. New York: McGraw-Hill, 1962.

[45] J. Zaanen, G. A. Sawatzky, and J. W. Allen, "Band gaps and electronic structure of transition-metal compounds," *Physical Review Letters*, vol. 55, pp. 418–421, July 1985.

[46] N. F. Mott, "The Basis of the Electron Theory of Metals, with Special Reference to the Transition Metals," *Proceedings of the Physical Society. Section A*, vol. 62, pp. 416–422, July 1949.

[47] J. Hubbard, "Electron correlations in narrow energy bands," *Proceedings of the Royal Society of London. Series A. Mathematical and Physical Sciences*, vol. 276, pp. 238–257, November 1963.

[48] I. I. Mazin, D. I. Khomskii, R. Lengsdorf, J. A. Alonso, W. G. Marshall, R. M. Ibberson, A. Podlesnyak, M. J. Martínez-Lope, and M. M. Abd-

Elmeguid, "Charge Ordering as Alternative to Jahn-Teller Distortion," *Physical Review Letters*, vol. 98, p. 176406, April 2007.

[49] J. L. García-Muñoz, J. Rodríguez-Carvajal, and P. Lacorre, "Neutron-diffraction study of the magnetic ordering in the insulating regime of the perovskites RNiO$_3$ (R = Pr and Nd)," *Physical Review B*, vol. 50, pp. 978–992, July 1994.

[50] J. A. Alonso, M. J. Martínez-Lope, I. A. Presniakov, A. V. Sobolev, V. S. Rusakov, A. M. Gapochka, G. Demazeau, and M. T. Fernández-Díaz, "Charge disproportionation in RNiO$_3$ (R = Tm, Yb) perovskites observed in situ by neutron diffraction and ^{57}Fe probe Mössbauer spectroscopy," *Physical Review B*, vol. 87, p. 184111, 2013.

[51] A. Subedi, O. E. Peil, and A. Georges, "Low-energy description of the metal-insulator transition in the rare-earth nickelates," *Physical Review B*, vol. 91, p. 075128, February 2015.

[52] D. J. Gawryluk, J. Rodríguez-Carvajal, P. Lacorre, M. T. Fernández-Díaz, and M. Medarde, "Distortion mode anomalies in bulk PrNiO$_3$," *arXiv e-prints*, p. arXiv:1809.10914, Sep 2018.

[53] J.-G. Cheng, J.-S. Zhou, J. B. Goodenough, J. A. Alonso, and M. J. Martinez-Lope, "Pressure dependence of metal-insulator transition in perovskites RNiO$_3$ (R = Eu, Y, Lu)," *Physical Review B*, vol. 82, p. 085107, August 2010.

[54] N. Wagner, D. Puggioni, and J. M. Rondinelli, "Learning from Correlations Based on Local Structure: Rare-Earth Nickelates Revisited," *Journal of Chemical Information and Modeling*, vol. 58, pp. 2491–2501, December 2018.

[55] M. Medarde, C. Dallera, M. Grioni, B. Delley, F. Vernay, J. Mesot, M. Sikora, J. A. Alonso, and M. J. Martínez-Lope, "Charge disproportionation in RNiO$_3$ perovskites (R = rare earth)," *Physical Review B*, vol. 80, p. 245105, December 2009.

[56] Y. Bodenthin, U. Staub, C. Piamonteze, M. García-Fernández, M. J. Martínez-Lope, and J. A. Alonso, "Magnetic and electronic properties of RNiO$_3$ (R = Pr, Nd, Eu, Ho and Y) perovskites studied by resonant soft x-ray magnetic powder diffraction," *Journal of Physics: Condensed Matter*, vol. 23, p. 036002, January 2011.

[57] J. García, J. Blasco, M. G. Proietti, and M. Benfatto, "Analysis of the x-ray-absorption near-edge-structure spectra of $La_{1-x}Nd_xNiO_3$ and $LaNi_{1-x}Fe_xO_3$ at the nickel K edge," *Physical Review B*, vol. 52, pp. 15823–15828, December 1995.

[58] X. Q. Xu, J. L. Peng, Z. Y. Li, H. L. Ju, and R. L. Greene, "Resisitivity, thermopower, and susceptibility of RNiO$_3$ (R = La,Pr)," *Physical Review B*, vol. 48, pp. 1112–1118, July 1993.

[59] J. L. García-Muñoz, J. Rodríguez-Carvajal, and P. Lacorre, "Sudden Appearance of an Unusual Spin Density Wave At the Metal-Insulator Transition in the Perovskites RNiO$_3$ (R = Pr, Nd)," *Europhysics Letters (EPL)*, vol. 20, pp. 241–247, October 1992.

[60] C. Castellani, C. R. Natoli, and J. Ranninger, "Magnetic structure of V_2O_3," *Physical Review B*, vol. 18, pp. 4945–4966, November 1978.

[61] M. T. Fernández-Díaz, J. A. Alonso, M. J. Martínez-Lope, M. T. Casais, and J. L. García-Muñoz, "Magnetic structure of the HoNiO$_3$ perovskite," *Physical Review B*, vol. 64, p. 144417, September 2001.

[62] M. Cyrot and C. Lyon-Caen, "Orbital superlattice in the degenerate Hubbard model," *Journal de Physique*, vol. 36, no. 3, pp. 253–266, 1975.

[63] K. Foyevtsova and G. A. Sawatzky, "A Band Theory Perspective on Molecular Orbitals in Complex Oxides," *Journal of Modern Physics*, vol. 10, no. 08, pp. 953–965, 2019.

[64] J. Kanamori, "Electron Correlation and Ferromagnetism of Transition Metals," *Progress of Theoretical Physics*, vol. 30, pp. 275–289, 09 1963.

[65] A. M. Oleś, "Antiferromagnetism and correlation of electrons in transition metals," *Physical Review B*, vol. 28, pp. 327–339, July 1983.

[66] A. B. Georgescu and S. Ismail-Beigi, "Generalized slave-particle method for extended Hubbard models," *Physical Review B*, vol. 92, p. 235117, December 2015.

[67] J. B. Goodenough, *Magnetism and the Chemical Bond*. John Wiley & Sons Inc., 1963.

[68] H. Hellmann, "Einführung in die Quantenchemie," in *Hans Hellmann: Einführung in die Quantenchemie*, pp. 19–376, Berlin, Heidelberg: Springer Berlin Heidelberg, 2015.

[69] R. P. Feynman, "Forces in Molecules," *Physical Review*, vol. 56, pp. 340–343, August 1939.

[70] D. J. Griffiths, *Introduction to Quantum Mechanics*. Toronto: Pearson Prentice Hall, 2nd ed., 2005.

[71] F. Jensen, *Introduction to Computational Chemistry*. Mississauga: John Wiley & Sons Inc., 2nd ed., 2007.

[72] J.-P. Blaizot and G. Ripka, *Quantum Theory of Finite Systems*. London: MIT Press, 1st ed., 1986.

[73] M. E. Peskin and D. V. Schroeder, *An Introduction to Quantum Field Theory*. Boca Raton, FL: CRC Press, 1995.

[74] A. A. Abrikosov, L. P. Gorkov, and I. E. Dzyaloshinski, *Methods of Quantum Field Theory in Statistical Physics*. Dover, 1975.

[75] M. P. Marder, *Condensed Matter Physics*. Hoboken, NJ, USA: John Wiley & Sons, Inc., October 2010.

[76] A. S. Banerjee, P. Suryanarayana, and J. E. Pask, "Periodic Pulay method for robust and efficient convergence acceleration of self-consistent field iterations," *Chemical Physics Letters*, vol. 647, pp. 31–35, March 2016.

[77] P. Pulay, "Convergence acceleration of iterative sequences. the case of scf iteration," *Chemical Physics Letters*, vol. 73, pp. 393–398, July 1980.

[78] R. Peters, *Magnetic Phases in the Hubbard Model*. PhD thesis, der Georg-August-Universitat Gottingen, 2009.

[79] R. Peters and T. Pruschke, "Half-filled Hubbard model on a Bethe lattice with next-nearest-neighbor hopping," *Physical Review B*, vol. 79, no. 4, pp. 1–7, 2009.

[80] E. C. Stoner, "LXXX. Atomic moments in ferromagnetic metals and alloys with non-ferromagnetic elements," *The London, Edinburgh, and Dublin Philosophical Magazine and Journal of Science*, vol. 15, pp. 1018–1034, May 1933.

Appendix A

Calculating the hopping coefficients $t_{ab}(\mathbf{k})$

In this appendix we start with the basic expressions for the hopping within the tight-binding model that we are constructing for the nickelates, and we calculate the hopping matrix elements to put them eventually into a simple form in Fourier space.

A.1 1st and 4th neighbour hopping

For 1st order hopping, there will not be any mixed orbital hopping between different directions, as discussed in the text, so we have

$$\hat{T}_1 = -t_1 \sum_{i\sigma} \Big[d^\dagger_{iz\sigma}(d_{i-z,z\sigma} + d_{i+z,z\sigma}) + d^\dagger_{ix\sigma}(d_{i-x,x\sigma} + d_{i+x,x\sigma}) + \\ + d^\dagger_{iy\sigma}(d_{i-y,y\sigma} + d_{i+y,y\sigma}) \Big]. \tag{A.1}$$

The first step it to put everything in terms of the $|z\rangle$ and $|\bar{z}\rangle$ states, using the expressions

$$\begin{aligned} d^\dagger_{ix\sigma} &= -\frac{1}{2} d^\dagger_{iz\sigma} + \frac{\sqrt{3}}{2} d^\dagger_{i\bar{z}\sigma} \\ d^\dagger_{iy\sigma} &= -\frac{1}{2} d^\dagger_{iz\sigma} - \frac{\sqrt{3}}{2} d^\dagger_{i\bar{z}\sigma}. \end{aligned} \tag{A.2}$$

Let us massage the terms separately. The y hopping gives

$$d^\dagger_{iy\sigma}(d_{i-y,y\sigma} + d_{i+y,y\sigma}) = \left(\frac{1}{2} d^\dagger_{iz\sigma} + \frac{\sqrt{3}}{2} d^\dagger_{i\bar{z}\sigma} \right) \times \\ \times \left(\frac{1}{2} d_{i-y,z\sigma} + \frac{\sqrt{3}}{2} d_{i-y,\bar{z}\sigma} + \frac{1}{2} d_{i+y,z\sigma} + \frac{\sqrt{3}}{2} d_{i+y,\bar{z}\sigma} \right)$$

while the x terms are

$$d^\dagger_{ix\sigma}(d_{i-x,x\sigma}+d_{i+x,x\sigma}) = \left(\frac{1}{2}d^\dagger_{iz\sigma} - \frac{\sqrt{3}}{2}d^\dagger_{i\bar{z}\sigma}\right)\times \\ \times\left(\frac{1}{2}d_{i-x,z\sigma} - \frac{\sqrt{3}}{2}d_{i-x,\bar{z}\sigma} + \frac{1}{2}d_{i+x,z\sigma} - \frac{\sqrt{3}}{2}d_{i+x,\bar{z}\sigma}\right)$$

Now all the operators are expressed in terms of the same orbitals, but hopping still occurs along different directions. Fourier transforming into momentum space should fix this. Notice that what orbital the operator has will have no influence on this transformation: the only thing that matters is the site index. Letting $\tau = x, y, z$ denote the displacement index for a site (and simultaneously a physical unit displacement vector $a\hat{x}, a\hat{y}, a\hat{z}$), we see that a standard term will transform in momentum space as

$$\sum_{i\sigma} d^\dagger_{ia\sigma}d_{i+\tau,b\sigma} = \frac{1}{N}\sum_{i\mathbf{k}\mathbf{q}\sigma} e^{-i\mathbf{k}\cdot\mathbf{R}_i}d^\dagger_{\mathbf{k}a\sigma}e^{i\mathbf{q}\cdot\mathbf{R}_{i+\tau}}d_{\mathbf{q}b\sigma} = \\ = \frac{1}{N}\sum_{i\mathbf{k}\mathbf{q}\sigma} e^{-i(\mathbf{k}-\mathbf{q})\cdot\mathbf{R}_i}d^\dagger_{\mathbf{k}a\sigma}e^{i\mathbf{q}\cdot\tau}d_{\mathbf{q}b\sigma} = \sum_{\mathbf{k}\sigma} e^{i\mathbf{k}\cdot\tau}d^\dagger_{\mathbf{k}a\sigma}d_{\mathbf{k}b\sigma}$$

Since the Hamiltonian is Hermitian, the hermitian conjugate of this term will also be present, which is of course hopping in the opposite direction — in our Hamiltonian it is represented by the hopping from the other side onto the same site i (plus orbital swap), as can be seen by shifting the index $i \to i + \tau$

$$\sum_{i\sigma} d^\dagger_{ib\sigma}d_{i-\tau,a\sigma} = \sum_{i\sigma} d^\dagger_{i+\tau,b\sigma}d_{ia\sigma} \xrightarrow{\text{same as above}} \sum_{\mathbf{k}\sigma} e^{-i\mathbf{k}\cdot\tau}d^\dagger_{\mathbf{k}a\sigma}d_{\mathbf{k}b\sigma}.$$

Together, of course, these terms produce the usual band structure

$$\sum_{i\sigma}(d^\dagger_{ia\sigma}d_{i+\tau,b\sigma} + \text{ h.c.}) = 2\sum_{\mathbf{k}\sigma}\cos(\mathbf{k}\cdot\tau)d^\dagger_{\mathbf{k}a\sigma}d_{\mathbf{k}b\sigma}.$$

To utilize these insights, let us group the appropriate terms from the x, y, z directions into nice groups based on orbitals. First, these are all the zz

terms from $\hat{T}_1$:

$$zz \text{ terms hopping along } z = \sum_{i\sigma} d^\dagger_{iz\sigma}(d_{i-z,z\sigma} + d_{i+z,z\sigma}) = \sum_{i\sigma} d^\dagger_{iz\sigma} d_{i-z,z\sigma} + \\ + \underbrace{\sum_{i\sigma} d^\dagger_{iz\sigma} d_{i+z,z\sigma}}_{\text{re-sum to h.c. form}} = \sum_{i\sigma} d^\dagger_{iz\sigma} d_{i-z,z\sigma} + \sum_{i\sigma} d^\dagger_{i-z,z\sigma} d_{iz\sigma} = \\ = \sum_{i\sigma} (d^\dagger_{iz\sigma} d_{i-z,z\sigma} + \text{ h.c. }) \xrightarrow{\text{applying the prescription}} \\ 2\sum_{\mathbf{k}\sigma} \cos\left(\mathbf{k} \cdot \underbrace{\tau}_{=a\hat{z}}\right) d^\dagger_{\mathbf{k}z\sigma} d_{\mathbf{k}z\sigma} = 2\sum_{\mathbf{k}\sigma} \cos(k_z a) d^\dagger_{\mathbf{k}z\sigma} d_{\mathbf{k}z\sigma}.$$

Now we collect zz terms hopping along x. We have

$$zz \text{ terms hopping along } x = \frac{1}{4}\sum_{i\sigma} (d^\dagger_{iz\sigma} d_{i-x,z\sigma} + d^\dagger_{iz\sigma} d_{i+x,z\sigma}) \\ \xrightarrow[\text{re-sum as before}]{\text{apply prescription}} \frac{1}{2}\sum_{\mathbf{k}\sigma} \cos(k_x a) d^\dagger_{\mathbf{k}z\sigma} d_{\mathbf{k}z\sigma}.$$

Now for zz terms hopping along y. We have exactly the same outcome as above

$$zz \text{ terms hopping along } y = \frac{1}{4}\sum_{i\sigma} (d^\dagger_{iz\sigma} d_{i-y,z\sigma} + d^\dagger_{iz\sigma} d_{i+y,z\sigma}) \to \\ \frac{1}{2}\sum_{\mathbf{k}\sigma} \cos(k_y a) d^\dagger_{\mathbf{k}z\sigma} d_{\mathbf{k}z\sigma}.$$

Now let us do the $\bar{z}\bar{z}$ terms. There are none with z hopping (for z these are the in-plane orbitals), so we go to x:

$$\bar{z}\bar{z} \text{ terms hopping along } x = \frac{3}{4}\sum_{i\sigma} (d^\dagger_{i\bar{z}\sigma} d_{i+x,\bar{z}\sigma} + d^\dagger_{i\bar{z}\sigma} d_{i+x,\bar{z}\sigma}) \to \\ \frac{3}{2}\sum_{\mathbf{k}\sigma} \cos(k_x a) d^\dagger_{\mathbf{k}\bar{z}\sigma} d_{\mathbf{k}\bar{z}\sigma}.$$

Exactly the same for y

$$\bar{z}\bar{z} \text{ terms hopping along } y = \frac{3}{4}\sum_{i\sigma} (d^\dagger_{i\bar{z}\sigma} d_{i+y,\bar{z}\sigma} + d^\dagger_{i\bar{z}\sigma} d_{i+y,\bar{z}\sigma}) \to \\ \frac{3}{2}\sum_{\mathbf{k}\sigma} \cos(k_y a) d^\dagger_{\mathbf{k}\bar{z}\sigma} d_{\mathbf{k}\bar{z}\sigma}.$$

Now for the cross terms. Again, there are no cross terms with z hopping, so we go directly to x. There will be four such terms, in conjugate pairs

$$z\bar{z} \text{ terms hopping along } x = -\frac{\sqrt{3}}{4}\sum_{i\sigma}\Big(\underbrace{(d^\dagger_{iz\sigma}d_{i-x,\bar{z}\sigma} + d^\dagger_{i\bar{z}\sigma}d_{i+x,z\sigma})}_{\text{h.c.'s}} + \\ + \underbrace{(d^\dagger_{i\bar{z}\sigma}d_{i-x,z\sigma} + d^\dagger_{iz\sigma}d_{i+x,\bar{z}\sigma})}_{\text{h.c.'s}}\Big) \xrightarrow[\text{same resummation}]{\text{apply prescription}} \\ -\frac{\sqrt{3}}{2}\sum_{\mathbf{k}\sigma}\cos(k_x a)\left(d^\dagger_{\mathbf{k}z\sigma}d_{\mathbf{k}\bar{z}\sigma} + d^\dagger_{\mathbf{k}\bar{z}\sigma}d_{\mathbf{k}z\sigma}\right).$$

Since the terms in the expansion of y are exactly the same save for the displacement vector $\hat{y}$ and that there are no minus signs, we get exactly the same outcome, with a + sign

$$z\bar{z} \text{ terms hopping along } y = \frac{\sqrt{3}}{4}\sum_{i\sigma}\Big((d^\dagger_{iz\sigma}d_{i-y,\bar{z}\sigma} + d^\dagger_{i\bar{z}\sigma}d_{i+y,z\sigma}) + \\ + (d^\dagger_{i\bar{z}\sigma}d_{i-y,z\sigma} + d^\dagger_{iz\sigma}d_{i+y,\bar{z}\sigma})\Big) \rightarrow \\ \frac{\sqrt{3}}{2}\sum_{\mathbf{k}\sigma}\cos(k_y a)\left(d^\dagger_{\mathbf{k}z\sigma}d_{\mathbf{k}\bar{z}\sigma} + d^\dagger_{\mathbf{k}\bar{z}\sigma}d_{\mathbf{k}z\sigma}\right).$$

And that's it! We have put our $\hat{T}_1$ Hamiltonian into momentum space, all in terms of z and $\bar{z}$ orbitals. We write

$$\hat{T}_1 = -t_1\sum_{\mathbf{k}\sigma}\Big[t^1_{zz}(\mathbf{k})d^\dagger_{\mathbf{k}z\sigma}d_{\mathbf{k}z\sigma} + t^1_{\bar{z}\bar{z}}(\mathbf{k})d^\dagger_{\mathbf{k}z\sigma}d_{\mathbf{k}z\sigma} + \\ + t^1_{z\bar{z}}(\mathbf{k})(d^\dagger_{\mathbf{k}z\sigma}d_{\mathbf{k}\bar{z}\sigma} + d^\dagger_{\mathbf{k}\bar{z}\sigma}d_{\mathbf{k}z\sigma})\Big], \qquad \text{(A.3)}$$

with

$$t^1_{zz}(\mathbf{k}) = 2\cos(k_z a) + \frac{1}{2}[\cos(k_x a) + \cos(k_y a)], \\ t^1_{\bar{z}\bar{z}}(\mathbf{k}) = \frac{3}{2}[\cos(k_x a) + \cos(k_y a)], \qquad \text{(A.4)} \\ t^1_{z\bar{z}}(\mathbf{k}) = -\frac{\sqrt{3}}{2}[\cos(k_x a) - \cos(k_y a)].$$

As mentioned in the text, we can immediately write down the corresponding result for the 4^{th} neighbour hopping by merely doubling the hop-

ping distance $a \to 2a$. Explicitly, we have

$$\hat{T}_4 = -t_4 \sum_{\mathbf{k}\sigma} \Big[t^4_{zz}(\mathbf{k}) d^\dagger_{\mathbf{k}z\sigma} d_{\mathbf{k}z\sigma} + t^4_{\bar{z}\bar{z}}(\mathbf{k}) d^\dagger_{\mathbf{k}z\sigma} d_{\mathbf{k}z\sigma} + \\ + t^4_{z\bar{z}}(\mathbf{k}) (d^\dagger_{\mathbf{k}z\sigma} d_{\mathbf{k}\bar{z}\sigma} + d^\dagger_{\mathbf{k}\bar{z}\sigma} d_{\mathbf{k}z\sigma}) \Big], \tag{A.5}$$

with

$$\begin{aligned} t^4_{zz}(\mathbf{k}) &= 2\cos(2k_z a) + \frac{1}{2}[\cos(2k_x a) + \cos(2k_y a)], \\ t^4_{\bar{z}\bar{z}}(\mathbf{k}) &= \frac{3}{2}[\cos(2k_x a) + \cos(2k_y a)], \\ t^4_{z\bar{z}}(\mathbf{k}) &= -\frac{\sqrt{3}}{2}[\cos(2k_x a) - \cos(2k_y a)]. \end{aligned} \tag{A.6}$$

A.2 2^{nd} neighbour hopping

Start with

$$\hat{T}_2 = -t_2 \sum_{iab\sigma, \hat{\tau} \neq \hat{\mu}} d^\dagger_{i+\hat{\tau}+\hat{\mu}, a\sigma} d_{ib\sigma}. \tag{A.7}$$

As discussed in the text, we can take $b = \tau$ and $a = \mu$, and then take the Fourier transform just as before, obtaining

$$\sum_{iab\sigma, \hat{\tau} \neq \hat{\mu}} d^\dagger_{i+\hat{\tau}+\hat{\mu}, a\sigma} d_{ib\sigma} = \sum_{i\sigma, a \neq b} d^\dagger_{i+\hat{b}+\hat{a}, a\sigma} d_{ib\sigma} = \sum_{\mathbf{k}\sigma, a \neq b} e^{i\mathbf{k}\cdot(\hat{b}+\hat{a})} d^\dagger_{\mathbf{k}a\sigma} d_{\mathbf{k}b\sigma}.$$

There are multiple possible summands arising from the above, but they will come in conjugate pairs. There are a total of 24 terms ($6 \cdot 6 = 36$ overall, but cannot have a and b be equal. There are 6 identical terms, but we sum over both a and b, so in fact we leave out 12 terms, so $36 - 12 = 24$), which are conjugate pairs based on the overall sign, like $+x + y$ and $-x - y$, or $+x - y$ and $-x + y$. Grouping them into conjugate pairs produces the following

(note the standard cos dispersion)

$$\sum_{\mathbf{k}\sigma,a\neq b} e^{i\mathbf{k}\cdot(\hat{b}+\hat{a})} d^\dagger_{\mathbf{k}a\sigma} d_{\mathbf{k}b\sigma} = \sum_{\mathbf{k}\sigma} 2\cos(k_x a + k_y a)\left[d^\dagger_{\mathbf{k}x\sigma} d_{\mathbf{k}y\sigma} + d^\dagger_{\mathbf{k}y\sigma} d_{\mathbf{k}x\sigma}\right] +$$
$$+ 2\cos(k_y a + k_z a)\left[d^\dagger_{\mathbf{k}y\sigma} d_{\mathbf{k}z\sigma} + d^\dagger_{\mathbf{k}z\sigma} d_{\mathbf{k}y\sigma}\right] +$$
$$+ 2\cos(k_z a + k_x a)\left[d^\dagger_{\mathbf{k}z\sigma} d_{\mathbf{k}x\sigma} + d^\dagger_{\mathbf{k}x\sigma} d_{\mathbf{k}z\sigma}\right] +$$
$$+ 2\cos(k_x a - k_y a)\left[d^\dagger_{\mathbf{k}x\sigma} d_{\mathbf{k}y\sigma} + d^\dagger_{\mathbf{k}y\sigma} d_{\mathbf{k}x\sigma}\right] +$$
$$+ 2\cos(k_y a - k_z a)\left[d^\dagger_{\mathbf{k}y\sigma} d_{\mathbf{k}z\sigma} + d^\dagger_{\mathbf{k}z\sigma} d_{\mathbf{k}y\sigma}\right] +$$
$$+ 2\cos(k_z a - k_x a)\left[d^\dagger_{\mathbf{k}z\sigma} d_{\mathbf{k}x\sigma} + d^\dagger_{\mathbf{k}x\sigma} d_{\mathbf{k}z\sigma}\right].$$

Using the trigonometric identity $\cos(x+y)+\cos(x-y) = 2\cos(x)\cos(y)$, we can reduce this even further to obtain

$$\sum_{\mathbf{k}\sigma,a\neq b} e^{i\mathbf{k}\cdot(\hat{b}+\hat{a})} d^\dagger_{\mathbf{k}a\sigma} d_{\mathbf{k}b\sigma} = \sum_{\mathbf{k}\sigma} \Big(4\cos(k_x a)\cos(k_y a)\times$$
$$\times \left[d^\dagger_{\mathbf{k}x\sigma} d_{\mathbf{k}y\sigma} + d^\dagger_{\mathbf{k}y\sigma} d_{\mathbf{k}x\sigma}\right] + 4\cos(k_y a)\cos(k_z a)\left[d^\dagger_{\mathbf{k}y\sigma} d_{\mathbf{k}z\sigma} + d^\dagger_{\mathbf{k}z\sigma} d_{\mathbf{k}y\sigma}\right] +$$
$$+ 4\cos(k_z a)\cos(k_x a)\left[d^\dagger_{\mathbf{k}z\sigma} d_{\mathbf{k}x\sigma} + d^\dagger_{\mathbf{k}x\sigma} d_{\mathbf{k}z\sigma}\right]\Big).$$

To make further progress, we need to express everything in terms of our preferred orbital basis $|z\rangle$ and $|\bar{z}\rangle$. Notice that, simply inverting the matrix in favour of $|x\rangle, |y\rangle$ from before, we find

$$\begin{bmatrix}|x\rangle\\|y\rangle\end{bmatrix} = \underbrace{\begin{bmatrix}-\frac{1}{2} & \frac{\sqrt{3}}{2}\\ -\frac{1}{2} & -\frac{\sqrt{3}}{2}\end{bmatrix}}_{=U}\begin{bmatrix}|z\rangle\\|\bar{z}\rangle\end{bmatrix} \rightarrow \begin{bmatrix}|z\rangle\\|\bar{z}\rangle\end{bmatrix} = \begin{bmatrix}-1 & -1\\ \frac{1}{\sqrt{3}} & -\frac{1}{\sqrt{3}}\end{bmatrix}\begin{bmatrix}|x\rangle\\|y\rangle\end{bmatrix}. \tag{A.8}$$

We can represent the three terms in our Hamiltonian in the following way (using the shorthand $d_x \equiv d_{\mathbf{k}x\sigma}$ and so on)

$$\left[d^\dagger_{\mathbf{k}x\sigma} d_{\mathbf{k}y\sigma} + d^\dagger_{\mathbf{k}y\sigma} d_{\mathbf{k}x\sigma}\right] \rightarrow \begin{bmatrix}d^\dagger_x, d^\dagger_y\end{bmatrix}\begin{bmatrix}d_y\\d_x\end{bmatrix} \tag{A.9}$$

Symbolically changing basis, we have

$$\begin{bmatrix}d^\dagger_x, d^\dagger_y\end{bmatrix}\begin{bmatrix}d_y\\d_x\end{bmatrix} = \begin{bmatrix}d^\dagger_z, d^\dagger_{\bar{z}}\end{bmatrix}(U^{-1})^t U^s \begin{bmatrix}d_{\bar{z}}\\d_z\end{bmatrix} =$$
$$= \begin{bmatrix}d^\dagger_z, d^\dagger_{\bar{z}}\end{bmatrix}\begin{bmatrix}-\frac{1}{2} & -\frac{1}{2}\\ \frac{\sqrt{3}}{2} & -\frac{\sqrt{3}}{2}\end{bmatrix}\begin{bmatrix}-\frac{\sqrt{3}}{2} & -\frac{1}{2}\\ \frac{\sqrt{3}}{2} & -\frac{1}{2}\end{bmatrix}\begin{bmatrix}d_{\bar{z}}\\d_z\end{bmatrix} = \begin{bmatrix}d^\dagger_z, d^\dagger_{\bar{z}}\end{bmatrix}\begin{bmatrix}0 & 1\\ -\frac{3}{2} & 0\end{bmatrix}\begin{bmatrix}d_{\bar{z}}\\d_z\end{bmatrix},$$

where the notation U^s means we swapped the two rows. Instead of plugging in expressions for each term, we can just perform this matrix product. The other terms looks similar, except the matrix will have one simple row for the terms that already include z:

$$\begin{bmatrix} d_y^\dagger, d_z^\dagger \end{bmatrix} \begin{bmatrix} d_z \\ d_y \end{bmatrix} = \begin{bmatrix} d_{\bar{z}}^\dagger, d_z^\dagger \end{bmatrix} \begin{bmatrix} -\frac{\sqrt{3}}{2} & 0 \\ -\frac{1}{2} & 1 \end{bmatrix} \begin{bmatrix} 1 & 0 \\ -\frac{1}{2} & -\frac{\sqrt{3}}{2} \end{bmatrix} \begin{bmatrix} d_z \\ d_{\bar{z}} \end{bmatrix} =$$
$$= \begin{bmatrix} d_{\bar{z}}^\dagger, d_z^\dagger \end{bmatrix} \begin{bmatrix} -\frac{\sqrt{3}}{2} & 0 \\ -1 & -\frac{\sqrt{3}}{2} \end{bmatrix} \begin{bmatrix} d_z \\ d_{\bar{z}} \end{bmatrix} = \begin{bmatrix} d_z^\dagger, d_{\bar{z}}^\dagger \end{bmatrix} \begin{bmatrix} -\frac{\sqrt{3}}{2} & -1 \\ 0 & -\frac{\sqrt{3}}{2} \end{bmatrix} \begin{bmatrix} d_{\bar{z}} \\ d_z \end{bmatrix}$$

just to straighten it out in accordance with the rest of the terms. Finally, for the last term we find (Adopt the shorthand $c_x \equiv \cos x$)

$$\begin{bmatrix} d_z^\dagger, d_x^\dagger \end{bmatrix} \begin{bmatrix} d_x \\ d_z \end{bmatrix} = \begin{bmatrix} d_z^\dagger, d_{\bar{z}}^\dagger \end{bmatrix} \begin{bmatrix} 1 & -\frac{1}{2} \\ 0 & \frac{\sqrt{3}}{2} \end{bmatrix} \begin{bmatrix} \frac{\sqrt{3}}{2} & -\frac{1}{2} \\ 0 & 1 \end{bmatrix} \begin{bmatrix} d_{\bar{z}} \\ d_z \end{bmatrix} =$$
$$= \begin{bmatrix} d_z^\dagger, d_{\bar{z}}^\dagger \end{bmatrix} \begin{bmatrix} \frac{\sqrt{3}}{2} & -1 \\ 0 & \frac{\sqrt{3}}{2} \end{bmatrix} \begin{bmatrix} d_{\bar{z}} \\ d_z \end{bmatrix}.$$

Adding them all together, we find

$$\cos(k_x a)\cos(k_y a)\left[d^\dagger_{\mathbf{k}x\sigma} d_{\mathbf{k}y\sigma} + d^\dagger_{\mathbf{k}y\sigma} d_{\mathbf{k}x\sigma}\right] + \cos(k_y a)\cos(k_z a)\times$$
$$\times \left[d^\dagger_{\mathbf{k}y\sigma} d_{\mathbf{k}z\sigma} + d^\dagger_{\mathbf{k}z\sigma} d_{\mathbf{k}y\sigma}\right] + \cos(k_z a)\cos(k_x a)\left[d^\dagger_{\mathbf{k}z\sigma} d_{\mathbf{k}x\sigma} + d^\dagger_{\mathbf{k}x\sigma} d_{\mathbf{k}z\sigma}\right] =$$
$$= \cos(k_x a)\cos(k_y a)\begin{bmatrix} d_z^\dagger, d_{\bar{z}}^\dagger \end{bmatrix} \begin{bmatrix} 0 & 1 \\ -\frac{3}{2} & 0 \end{bmatrix} \begin{bmatrix} d_{\bar{z}} \\ d_z \end{bmatrix} +$$
$$+ \cos(k_y a)\cos(k_z a)\begin{bmatrix} d_z^\dagger, d_{\bar{z}}^\dagger \end{bmatrix} \begin{bmatrix} -\frac{\sqrt{3}}{2} & -1 \\ 0 & -\frac{\sqrt{3}}{2} \end{bmatrix} \begin{bmatrix} d_{\bar{z}} \\ d_z \end{bmatrix} +$$
$$+ \cos(k_z a)\cos(k_x a)\begin{bmatrix} d_z^\dagger, d_{\bar{z}}^\dagger \end{bmatrix} \begin{bmatrix} \frac{\sqrt{3}}{2} & -1 \\ 0 & \frac{\sqrt{3}}{2} \end{bmatrix} \begin{bmatrix} d_{\bar{z}} \\ d_z \end{bmatrix} =$$
$$= \begin{bmatrix} d_z^\dagger, d_{\bar{z}}^\dagger \end{bmatrix} \begin{bmatrix} \frac{\sqrt{3}}{2} c_z(c_x - c_y) & c_x c_y - c_z(c_y + c_x) \\ -\frac{3}{2} c_x c_y & \frac{\sqrt{3}}{2} c_z(c_x - c_y) \end{bmatrix} \begin{bmatrix} d_{\bar{z}} \\ d_z \end{bmatrix} =$$
$$= \left[c_x c_y - c_z(c_y + c_x)\right] d_z^\dagger d_z + \left[-\frac{3}{2} c_x c_y\right] d_{\bar{z}}^\dagger d_{\bar{z}} +$$
$$+ \left[\frac{\sqrt{3}}{2} c_z(c_x - c_y)\right](d_z^\dagger d_{\bar{z}} + d_{\bar{z}}^\dagger d_z).$$

Done! Putting this all together, the form of the Hamiltonian is

$$\hat{T}_2 = -2t_2 \sum_{\mathbf{k}\sigma} \Big[t^2_{zz}(\mathbf{k}) d^\dagger_{\mathbf{k}z\sigma} d_{\mathbf{k}z\sigma} + t^2_{\bar{z}\bar{z}}(\mathbf{k}) d^\dagger_{\mathbf{k}\bar{z}\sigma} d_{\mathbf{k}\bar{z}\sigma} + \\ + t^2_{z\bar{z}}(\mathbf{k}) (d^\dagger_{\mathbf{k}z\sigma} d_{\mathbf{k}\bar{z}\sigma} + d^\dagger_{\mathbf{k}\bar{z}\sigma} d_{\mathbf{k}z\sigma}) \Big], \quad \text{(A.10)}$$

with

$$\begin{aligned} t^2_{zz}(\mathbf{k}) &= 2\cos(k_x a)\cos(k_y a) - 2\cos(k_z a)(\cos(k_y a) + \cos(k_x a)), \\ t^2_{z\bar{z}}(\mathbf{k}) &= \sqrt{3}\cos(k_z a)(\cos(k_x a) - \cos(k_y a)), \\ t^2_{\bar{z}\bar{z}}(\mathbf{k}) &= -3\cos(k_x a)\cos(k_y a). \end{aligned} \quad \text{(A.11)}$$

A.3 Full hopping operator

Altogether, then, the hopping operator has the form

$$\hat{T} = \sum_{\mathbf{k}\sigma} \Big[t_{zz}(\mathbf{k}) d^\dagger_{\mathbf{k}z\sigma} d_{\mathbf{k}z\sigma} + t_{\bar{z}\bar{z}}(\mathbf{k}) d^\dagger_{\mathbf{k}\bar{z}\sigma} d_{\mathbf{k}\bar{z}\sigma} + \\ + t_{z\bar{z}}(\mathbf{k}) (d^\dagger_{\mathbf{k}z\sigma} d_{\mathbf{k}\bar{z}\sigma} + d^\dagger_{\mathbf{k}\bar{z}\sigma} d_{\mathbf{k}z\sigma}) \Big], \quad \text{(A.12)}$$

with the definitions

$$\begin{aligned} t_{zz}(\mathbf{k}) =& -2t_1 \left(\cos(k_z a) + \frac{1}{4}[\cos(k_x a) + \cos(k_y a)] \right) - \\ & - 2t_4 \left(\cos(2k_z a) + \frac{1}{4}[\cos(2k_x a) + \cos(2k_y a)] \right) - \\ & - 2t_2 \left[\cos(k_x a)\cos(k_y a) - 2\cos(k_z a)(\cos(k_y a) + \cos(k_x a)) \right], \\ t_{\bar{z}\bar{z}}(\mathbf{k}) =& -\frac{3t_1}{2}[\cos(k_x a) + \cos(k_y a)] - \frac{3t_4}{2}[\cos(2k_x a) + \cos(2k_y a)] + \\ & + 6t_2 \cos(k_x a)\cos(k_y a), \\ t_{z\bar{z}}(\mathbf{k}) =& \frac{\sqrt{3}t_1}{2}[\cos(k_x a) - \cos(k_y a)] + \frac{\sqrt{3}t_4}{2}[\cos(2k_x a) - \cos(2k_y a)] - \\ & - 2\sqrt{3}t_2 \cos(k_z a)(\cos(k_x a) - \cos(k_y a)). \end{aligned} \quad \text{(A.13)}$$

Appendix B

Minimizing lattice contributions: solving the cubic equation

In the text we were faced with the need to solve the cubic equation

$$u^3 + \frac{1}{a}u - \frac{\delta}{a} = 0 \tag{B.1}$$

which arose during lattice energy minimization in the Hartree-Fock process. It turns out that it admits a closed form solution: write

$$u^3 = (s-t)^3, \quad \frac{1}{a} = 3st, \quad \frac{\delta}{a} = s^3 - t^3$$

Combining the latter two equations into one fo t, we find

$$t^6 + t^3\left(\frac{\delta}{a}\right) - \left(\frac{1}{3a}\right)^3 = 0$$

which is easily solved as a quadratic

$$t^3 = \frac{1}{2}\left(-\frac{\delta}{a} \pm \sqrt{\left(\frac{\delta}{a}\right)^2 + \frac{4}{27a^3}}\right)$$

$$s^3 = t^3 + \frac{\delta}{a} = \frac{1}{2}\left(\frac{\delta}{a} \pm \sqrt{\left(\frac{\delta}{a}\right)^2 + \frac{4}{27a^3}}\right)$$

from which we can recover the expression for u

$$u = \delta\frac{3}{2\beta^{1/3}}\left[\left(1 + \sqrt{1+\frac{1}{\beta}}\right)^{1/3} + \left(1 - \sqrt{1+\frac{1}{\beta}}\right)^{1/3}\right] \tag{B.2}$$

where we set $\beta = \frac{27}{4}a\delta^2$. So we see that the charge disproportionation factor δ couples to the lattice distortions.

Appendix C

Calculation of $\langle \hat{H}_e \rangle$

In this appendix we express the electron-electron interaction contribution to the Hartree-Fock energy, $\langle \hat{H}_e \rangle$, which we found in the text to be

$$\begin{aligned}
\langle \hat{H}_e \rangle_{\Psi_e} = U \sum_{ia} \Big[\langle d^\dagger_{ia\uparrow} d_{ia\uparrow} \rangle \langle d^\dagger_{ia\downarrow} d_{ia\downarrow} \rangle - \langle d^\dagger_{ia\uparrow} d_{ia\downarrow} \rangle \langle d^\dagger_{ia\downarrow} d_{ia\uparrow} \rangle \Big] + \\
+ U' \sum_{i\sigma} \Big[\langle d^\dagger_{iz\sigma} d_{iz\sigma} \rangle \langle d^\dagger_{i\bar{z}\bar{\sigma}} d_{i\bar{z}\bar{\sigma}} \rangle - \langle d^\dagger_{iz\sigma} d_{i\bar{z}\bar{\sigma}} \rangle \langle d^\dagger_{i\bar{z}\bar{\sigma}} d_{iz\sigma} \rangle \Big] + \\
+ (U' - J) \sum_{i\sigma} \Big[\langle d^\dagger_{iz\sigma} d_{iz\sigma} \rangle \langle d^\dagger_{i\bar{z}\sigma} d_{i\bar{z}\sigma} \rangle - \langle d^\dagger_{iz\sigma} d_{i\bar{z}\sigma} \rangle \langle d^\dagger_{i\bar{z}\sigma} d_{iz\sigma} \rangle \Big] - \\
- J \sum_{i\sigma} \Big[\langle d^\dagger_{iz\sigma} d_{iz\bar{\sigma}} \rangle \langle d^\dagger_{i\bar{z}\bar{\sigma}} d_{i\bar{z}\sigma} \rangle - \langle d^\dagger_{iz\sigma} d_{i\bar{z}\sigma} \rangle \langle d^\dagger_{i\bar{z}\bar{\sigma}} d_{iz\bar{\sigma}} \rangle \Big] + \\
+ \gamma J \sum_{ia} \Big[\langle d^\dagger_{ia\uparrow} d_{i\bar{a}\uparrow} \rangle \langle d^\dagger_{ia\downarrow} d_{i\bar{a}\downarrow} \rangle - \langle d^\dagger_{ia\uparrow} d_{i\bar{a}\downarrow} \rangle \langle d^\dagger_{ia\downarrow} d_{i\bar{a}\uparrow} \rangle \Big], \quad \text{(C.1)}
\end{aligned}$$

in terms of the newly-defined order parameters $\delta, S_{\mathrm{FM}}, ...$, which are set by

$$\begin{aligned}
\langle d^\dagger_{ia\sigma} d^\dagger_{ia\sigma} \rangle =& \frac{1}{4} \left[1 + \delta e^{i\mathbf{Q}_c \cdot \mathbf{R}_i} \right] + \frac{\sigma}{2} \Big[S_{\mathrm{FM}} + S_{\mathrm{AFM}} e^{i\mathbf{Q}_c \cdot \mathbf{R}_i} + \\
& + S_{1\mathrm{z}} \cos(\mathbf{Q}_m \cdot \mathbf{R}_i) + S_{2\mathrm{z}} \sin(\mathbf{Q}_m \cdot \mathbf{R}_i) \Big], \\
\langle d^\dagger_{ia\sigma} d^\dagger_{ia\bar{\sigma}} \rangle =& \frac{1}{2} \left[S_{1\mathrm{x}} \cos(\mathbf{Q}_m \cdot \mathbf{R}_i) + S_{2\mathrm{x}} \sin(\mathbf{Q}_m \cdot \mathbf{R}_i) \right], \\
\langle d^\dagger_{ia\sigma} d^\dagger_{i\bar{a}\sigma} \rangle =& O_1 + O_2 e^{i\mathbf{Q}_c \cdot \mathbf{R}_i} + \sigma \Big[Z_1 + Z_2 e^{i\mathbf{Q}_c \cdot \mathbf{R}_i} + \\
& + Z_3 \cos(\mathbf{Q}_m \cdot \mathbf{R}_i) + Z_4 \sin(\mathbf{Q}_m \cdot \mathbf{R}_i) \Big], \\
\langle d^\dagger_{ia\sigma} d^\dagger_{i\bar{a}\bar{\sigma}} \rangle =& X_1 \cos(\mathbf{Q}_m \cdot \mathbf{R}_i) + X_2 \sin(\mathbf{Q}_m \cdot \mathbf{R}_i). \quad \text{(C.2)}
\end{aligned}$$

We calculate the contributions term by term. The important trick to remember is that $\sum_i e^{i\mathbf{s}\cdot\mathbf{R}_i}(...) = 0$ unless $\mathbf{s} \cdot \mathbf{R}_i = 0 \mod 2\pi$. Otherwise the exponential keeps alternating sign and the sum essentially cancels itself out. An exact derivation of this fact, as well as many important examples of its application are given in the appendices of Marder's textbook on condensed

matter physics [75]. Below, whenever we encounter sums over terms that have non-vanishing exponentials we will immediately drop them from the expression. And whenever there is a cosine or a sine, expressing it in terms of the exponentials will allow us to apply that same rule. Let us derive those rules: for a product of cosines

$$\sum_i \cos^2(\mathbf{Q}_m \cdot \mathbf{R}_i) = \sum_i \frac{1}{4}(e^{i(\mathbf{Q}_m \cdot \mathbf{R}_i)} + e^{-i(\mathbf{Q}_m \cdot \mathbf{R}_i)})^2 = \\ = \sum_i \frac{1}{4}(e^{i\mathbf{Q}_c \cdot \mathbf{R}_i} + 2 + e^{-i\mathbf{Q}_c \cdot \mathbf{R}_i}) = \frac{1}{4} 2N = \frac{N}{2}. \tag{C.3}$$

For sines this is identical, except there is a minus sign which is fixed by the presence of the i in the denominator that gets squared to -1

$$\sum_i \sin^2(\mathbf{Q}_m \cdot \mathbf{R}_i) = \sum_i \frac{1}{-4}(e^{i(\mathbf{Q}_m \cdot \mathbf{R}_i)} - e^{-i(\mathbf{Q}_m \cdot \mathbf{R}_i)})^2 = \frac{N}{2}. \tag{C.4}$$

Finally, for a product of sines and cosines we find

$$\sum_i \cos(\mathbf{Q}_m \cdot \mathbf{R}_i) \sin(\mathbf{Q}_m \cdot \mathbf{R}_i) = \sum_i \frac{1}{4}(e^{i(\mathbf{Q}_m \cdot \mathbf{R}_i)} + e^{-i(\mathbf{Q}_m \cdot \mathbf{R}_i)}) \times \\ \times (e^{i(\mathbf{Q}_m \cdot \mathbf{R}_i)} - e^{-i(\mathbf{Q}_m \cdot \mathbf{R}_i)}) = \sum_i \frac{1}{4}(e^{i\mathbf{Q}_c \cdot \mathbf{R}_i} + 0 - e^{-i\mathbf{Q}_c \cdot \mathbf{R}_i}) = 0. \tag{C.5}$$

The first term gives

$$U \sum_{ia} \Big[\langle d^\dagger_{ia\uparrow} d_{ia\uparrow} \rangle \langle d^\dagger_{ia\downarrow} d_{ia\downarrow} \rangle - \langle d^\dagger_{ia\uparrow} d_{ia\downarrow} \rangle \langle d^\dagger_{ia\downarrow} d_{ia\uparrow} \rangle \Big] = \\ = U \sum_{ia} \Big[\frac{1}{16}(1 + \delta e^{i\mathbf{Q}_c \cdot \mathbf{R}_i})^2 - \frac{\sigma^2}{4} \Big[S_{\mathrm{FM}} + S_{\mathrm{AFM}} e^{i\mathbf{Q}_c \cdot \mathbf{R}_i} + S_{1\mathrm{z}} \cos(\mathbf{Q}_m \cdot \mathbf{R}_i) + \\ + S_{2\mathrm{z}} \sin(\mathbf{Q}_m \cdot \mathbf{R}_i) \Big]^2 - \frac{1}{4}(S_{1\mathrm{x}} \cos(\mathbf{Q}_m \cdot \mathbf{R}_i) + S_{2\mathrm{x}} \sin(\mathbf{Q}_m \cdot \mathbf{R}_i))^2 \Big] = \\ = U \sum_i \Big[\frac{1}{8}(1 + \delta^2) - \frac{1}{4} \Big[S^2_{\mathrm{FM}} + S^2_{\mathrm{AFM}} + \frac{1}{2} S^2_{1\mathrm{z}} + \frac{1}{2} S^2_{2\mathrm{z}} \Big] - \\ - \frac{1}{4} \left(\frac{1}{2} S^2_{1\mathrm{x}} + \frac{1}{2} S^2_{2\mathrm{x}} \right) \Big] = \\ = 2UN \left[\frac{1}{16}(1 + \delta^2) - \frac{1}{4} \left(S^2_{\mathrm{FM}} + S^2_{\mathrm{AFM}} + \frac{S^2_{1\mathrm{z}} + S^2_{2\mathrm{z}} + S^2_{1\mathrm{x}} + S^2_{2\mathrm{x}}}{2} \right) \right]. \tag{C.6}$$

The second term gives, by analogy (it is almost exactly the same as the first, same for X instead of $S_{1,2\mathrm{x}}$ in the last term)

$$
\begin{aligned}
&U' \sum_{i\sigma} \Big[\langle d^\dagger_{iz\sigma} d_{iz\sigma} \rangle \langle d^\dagger_{i\bar{z}\bar{\sigma}} d_{i\bar{z}\bar{\sigma}} \rangle - \langle d^\dagger_{iz\sigma} d_{i\bar{z}\bar{\sigma}} \rangle \langle d^\dagger_{i\bar{z}\bar{\sigma}} d_{iz\sigma} \rangle \Big] = \\
&= U' \sum_{i\sigma} \Big[\frac{1}{16} (1 + \delta e^{i\mathbf{Q}_c \cdot \mathbf{R}_i})^2 - \frac{\sigma^2}{4} \Big[S_{\mathrm{FM}} + S_{\mathrm{AFM}} e^{i\mathbf{Q}_c \cdot \mathbf{R}_i} + S_{1\mathrm{z}} \cos(\mathbf{Q}_m \cdot \mathbf{R}_i) + \\
&\quad + S_{2\mathrm{z}} \sin(\mathbf{Q}_m \cdot \mathbf{R}_i) \Big]^2 - \frac{1}{4} (X_1 \cos(\mathbf{Q}_m \cdot \mathbf{R}_i) + X_2 \sin(\mathbf{Q}_m \cdot \mathbf{R}_i))^2 \Big] = \\
&= 2U'N \left[\frac{1}{16} (1 + \delta^2) - \frac{1}{4} \left(S^2_{\mathrm{FM}} + S^2_{\mathrm{AFM}} + \frac{S^2_{1\mathrm{z}} + S^2_{2\mathrm{z}}}{2} \right) - \frac{1}{2} (X_1^2 + X_2^2) \right].
\end{aligned}
\tag{C.7}
$$

The third term gives

$$
\begin{aligned}
&(U' - J) \sum_{i\sigma} \Big[\langle d^\dagger_{iz\sigma} d_{iz\sigma} \rangle \langle d^\dagger_{i\bar{z}\sigma} d_{i\bar{z}\sigma} \rangle - \langle d^\dagger_{iz\sigma} d_{i\bar{z}\sigma} \rangle \langle d^\dagger_{i\bar{z}\sigma} d_{iz\sigma} \rangle \Big] = \\
&= (U' - J) \sum_{i\sigma} \Big\{ \frac{1}{4} (1 + \delta e^{i\mathbf{Q}_c \cdot \mathbf{R}_i}) + \frac{\sigma}{2} \Big[S_{\mathrm{FM}} + S_{\mathrm{AFM}} e^{i\mathbf{Q}_c \cdot \mathbf{R}_i} + S_{1\mathrm{z}} \cos(\mathbf{Q}_m \cdot \mathbf{R}_i) + \\
&\quad + S_{2\mathrm{z}} \sin(\mathbf{Q}_m \cdot \mathbf{R}_i) \Big] \Big\}^2 + \Big\{ O_1 + O_2 e^{i\mathbf{Q}_c \cdot \mathbf{R}_i} + \sigma \Big[Z_1 + Z_2 e^{i\mathbf{Q}_c \cdot \mathbf{R}_i} + \\
&\quad + Z_3 \cos(\mathbf{Q}_m \cdot \mathbf{R}_i) + Z_4 \sin(\mathbf{Q}_m \cdot \mathbf{R}_i) \Big] \Big\}^2 = (U' - J) \sum_{i\sigma} \Big\{ \frac{1}{16} (1 + \delta^2) + \\
&+ \frac{1}{4} \Big[S^2_{\mathrm{FM}} + S^2_{\mathrm{AFM}} + \frac{S^2_{1\mathrm{z}} + S^2_{2\mathrm{z}}}{2} \Big] + \frac{\sigma}{4} \Big[S_{\mathrm{FM}} + S_{\mathrm{AFM}} \delta \Big] \Big\} + \Big\{ O_1^2 + O_2^2 + Z_1^2 + \\
&\quad + Z_2^2 + \frac{Z_3^2 + Z_4^2}{2} + \sigma \Big(O_1 Z_1 + O_2 Z_2 \Big) \Big\} = 2(U' - J) N \Big[\frac{1}{16} (1 + \delta^2) + \\
&+ \frac{1}{4} \Big[S^2_{\mathrm{FM}} + S^2_{\mathrm{AFM}} + \frac{S^2_{1\mathrm{z}} + S^2_{2\mathrm{z}}}{2} \Big] + O_1^2 + O_2^2 + Z_1^2 + Z_2^2 + \frac{Z_3^2 + Z_4^2}{2} \Big].
\end{aligned}
\tag{C.8}
$$

where towards the end the σ-dependent terms dropped out because of the sum over the spins.

The fourth term gives

$$
\begin{aligned}
&- J \sum_{i\sigma} \Big[\langle d^\dagger_{iz\sigma} d_{iz\bar{\sigma}} \rangle \langle d^\dagger_{i\bar{z}\bar{\sigma}} d_{i\bar{z}\sigma} \rangle - \langle d^\dagger_{iz\sigma} d_{i\bar{z}\sigma} \rangle \langle d^\dagger_{i\bar{z}\bar{\sigma}} d_{iz\bar{\sigma}} \rangle \Big] = \\
&= -J \sum_{i\sigma} \Big[\frac{1}{4} (S_{1\mathrm{x}} \cos(\mathbf{Q}_m \cdot \mathbf{R}_i) + S_{2\mathrm{x}} \sin(\mathbf{Q}_m \cdot \mathbf{R}_i))^2 - (O_1 + O_2 e^{i\mathbf{Q}_c \cdot \mathbf{R}_i})^2 + \\
&\quad + \Big(Z_1 + Z_2 e^{i\mathbf{Q}_c \cdot \mathbf{R}_i} + Z_3 \cos(i\mathbf{Q}_c \cdot \mathbf{R}_i) + Z_4 \sin(i\mathbf{Q}_c \cdot \mathbf{R}_i) \Big)^2 \Big] = \\
&\quad = -2JN \left[\frac{S_{1\mathrm{x}}^2 + S_{2\mathrm{x}}^2}{8} - (O_1^2 + O_2^2) + \left(Z_1^2 + Z_2^2 + \frac{Z_3^2 + Z_4^2}{2} \right) \right]. \quad \text{(C.9)}
\end{aligned}
$$

And, finally, the fifth term

$$
\begin{aligned}
&\gamma J \sum_{ia} \Big[\langle d^\dagger_{ia\uparrow} d_{i\bar{a}\uparrow} \rangle \langle d^\dagger_{ia\downarrow} d_{i\bar{a}\downarrow} \rangle - \langle d^\dagger_{ia\uparrow} d_{i\bar{a}\downarrow} \rangle \langle d^\dagger_{ia\downarrow} d_{i\bar{a}\uparrow} \rangle \Big] = \\
&= \gamma J \sum_{ia} \Big[(O_1 + O_2 e^{i\mathbf{Q}_c \cdot \mathbf{R}_i})^2 - \Big(Z_1 + Z_2 e^{i\mathbf{Q}_c \cdot \mathbf{R}_i} + Z_3 \cos(i\mathbf{Q}_c \cdot \mathbf{R}_i) + \\
&\quad + Z_4 \sin(i\mathbf{Q}_c \cdot \mathbf{R}_i) \Big)^2 - (X_1 \cos(\mathbf{Q}_m \cdot \mathbf{R}_i) + X_2 \sin(\mathbf{Q}_m \cdot \mathbf{R}_i))^2 \Big] = \\
&\quad = 2\gamma JN \left[O_1^2 + O_2^2 - \left(Z_1^2 + Z_2^2 + \frac{Z_3^2 + Z_4^2 + X_1^2 + X_2^2}{2} \right) \right]. \quad \text{(C.10)}
\end{aligned}
$$

Combining all of these together, we find

$$
\begin{aligned}
\frac{\langle \hat{H}_e \rangle}{N} =& \frac{3U - 5J}{8}(1 + \delta^2) - \frac{U + J}{2} \left(S_{\mathrm{FM}}^2 + S_{\mathrm{AFM}}^2 + \frac{\mathbf{S}_1^2 + \mathbf{S}_2^2}{2} \right) - \\
&- 2(U' - (2 + \gamma)J)(O_1^2 + O_2^2) - 2(U' + \gamma J) \Big(Z_1^2 + Z_2^2 + \\
&+ \frac{Z_3^2 + Z_4^2}{2} \Big) - (U' + \gamma J)(X_1^2 + X_2^2). \quad \text{(C.11)}
\end{aligned}
$$

In this thesis we make the assumption of spherical symmetry for the two-band Hubbard terms: this assumption means that $U' = U - 2J$. With this in mind, we obtain the final form

$$
\begin{aligned}
\frac{\langle \hat{H}_e \rangle}{N} =& \frac{3U - 5J}{8}(1 + \delta^2) - \frac{U + J}{2} \left(S_{\mathrm{FM}}^2 + S_{\mathrm{AFM}}^2 + \frac{\mathbf{S}_1^2 + \mathbf{S}_2^2}{2} \right) - \\
&- 2(U - (4 + \gamma)J)(O_1^2 + O_2^2) - 2(U + (\gamma - 2)J) \Big(Z_1^2 + Z_2^2 + \\
&+ \frac{Z_3^2 + Z_4^2}{2} \Big) - (U + (\gamma - 2)J)(X_1^2 + X_2^2). \quad \text{(C.12)}
\end{aligned}
$$

Appendix D

Fourier Transforming $\hat{H}_{\mathbf{HF}}$

The task of this appendix is to make use of the Bloch symmetry of the Hartree-Fock Hamiltonian

$$\begin{aligned}\hat{H}_{\mathrm{HF}} = \sum_{ijab\sigma} t_{ij}^{ab} d_{ia\sigma}^{\dagger} d_{jb\sigma} + \Big\{ \frac{3U-5J}{4} + \left[\frac{3U-5J}{4}\delta - 2\epsilon_b u \right] e^{i\mathbf{Q}_c\cdot\mathbf{R}_i} - \\ - \frac{\sigma}{2}(U+J)\Big[S_{\mathrm{FM}} + S_{\mathrm{AFM}} e^{i\mathbf{Q}_c\cdot\mathbf{R}_i} + S_{1\mathrm{z}} \cos\mathbf{Q}_m\cdot\mathbf{R}_i + S_{2\mathrm{z}} \sin\mathbf{Q}_m\cdot\mathbf{R}_i \Big] \Big\} d_{ia\sigma}^{\dagger} d_{ia\sigma} - \\ - \frac{U+J}{2} \left[S_{1\mathrm{x}} \cos\mathbf{Q}_m\cdot\mathbf{R}_i + S_{2\mathrm{x}} \sin\mathbf{Q}_m\cdot\mathbf{R}_i \right] d_{ia\sigma}^{\dagger} d_{ia\bar{\sigma}} - \\ - (U + J(\gamma-2)) \Big[X_1 \cos\mathbf{Q}_m\cdot\mathbf{R}_i + X_2 \sin\mathbf{Q}_m\cdot\mathbf{R}_i \Big] d_{ia\sigma}^{\dagger} d_{i\bar{a}\bar{\sigma}} + \\ + \Big\{ \big(J(4+\gamma) - U\big) \Big[O_1 + O_2 e^{i\mathbf{Q}_c\cdot\mathbf{R}_i} \Big] - \sigma \Big[U + J(\gamma-2) \Big] \times \\ \times \Big[Z_1 + Z_2 e^{i\mathbf{Q}_c\cdot\mathbf{R}_i} + Z_3 \cos\mathbf{Q}_m\cdot\mathbf{R}_i + Z_4 \sin\mathbf{Q}_m\cdot\mathbf{R}_i \Big] \Big\} d_{ia\sigma}^{\dagger} d_{i\bar{a}\sigma}. \quad \text{(D.1)}\end{aligned}$$

and Fourier transform it into $\mathbf{k}$-space according to the rule

$$d_{\mathbf{k}a\sigma}^{\dagger} = \sum_i \frac{e^{i\mathbf{k}\mathbf{R}_i}}{\sqrt{N}} d_{ia\sigma}^{\dagger}. \quad \text{(D.2)}$$

The Fourier transform of the hopping operator was already carried out in Appendix A, resulting in

$$\hat{T} = \sum_{\mathbf{k}ab\sigma} t_{ab}(\mathbf{k}) d_{\mathbf{k}a\sigma}^{\dagger} d_{\mathbf{k}b\sigma},$$

with the coefficients $t_{ab}(\mathbf{k})$ tabulated in Appendix A. In order to deal with the rest, we need a quick rule of thumb. Fourier transforming a term of the form $\sum_i e^{i\mathbf{s}\cdot\mathbf{R}_i} d_{ia\sigma}^{\dagger} d_{ib\tau}$ simply offsets the momentum label of one of the d operators by the vector $\mathbf{s}$

$$\sum_i e^{i\mathbf{s}\cdot\mathbf{R}_i} d_{ia\sigma}^{\dagger} d_{ib\tau} \xrightarrow[\text{with } D.2]{\text{Fourier transform}} \sum_{\mathbf{k}} d_{\mathbf{k}+\mathbf{s},a\sigma}^{\dagger} d_{\mathbf{k}b\tau}. \quad \text{(D.3)}$$

Armed with this rule, we tackle the Hamiltonian term by term. The first term gives

$$\Big\{\frac{3U-5J}{4}+\Big[\frac{3U-5J}{4}\delta-2\epsilon_b u\Big]\,e^{i\mathbf{Q}_c\cdot\mathbf{R}_i}-\frac{\sigma}{2}(U+J)\Big[S_{\mathrm{FM}}+S_{\mathrm{AFM}}e^{i\mathbf{Q}_c\cdot\mathbf{R}_i}+ \\ +S_{1\mathrm{z}}\cos\mathbf{Q}_m\cdot\mathbf{R}_i+S_{2\mathrm{z}}\sin\mathbf{Q}_m\cdot\mathbf{R}_i\Big]\Big\}d^\dagger_{ia\sigma}d_{ia\sigma}= \\ =\Big[\frac{3U-5J}{4}-\frac{\sigma}{2}(U+J)S_{\mathrm{FM}}\Big]d^\dagger_{\mathbf{k}a\sigma}d_{\mathbf{k}a\sigma}+\Big[\frac{3U-5J}{4}\delta-2\epsilon_b u- \\ -\frac{\sigma}{2}(U+J)S_{\mathrm{AFM}}\Big]d^\dagger_{\mathbf{k}+\mathbf{Q}_c,a\sigma}d_{\mathbf{k}a\sigma}-\frac{\sigma}{4}(U+J)\Big[(S_{1\mathrm{z}}-iS_{2\mathrm{z}})d^\dagger_{\mathbf{k}+\mathbf{Q}_m,a\sigma}d_{\mathbf{k}a\sigma}+ \\ +(S_{1\mathrm{z}}+iS_{2\mathrm{z}})d^\dagger_{\mathbf{k}-\mathbf{Q}_m,a\sigma}d_{\mathbf{k}a\sigma}\Big].$$

The second term gives

$$-\frac{U+J}{2}\left[S_{1\mathrm{x}}\cos\mathbf{Q}_m\cdot\mathbf{R}_i+S_{2\mathrm{x}}\sin\mathbf{Q}_m\cdot\mathbf{R}_i\right]d^\dagger_{ia\sigma}d_{ia\bar{\sigma}}= \\ =-\frac{1}{4}(U+J)\Big[(S_{1\mathrm{x}}-iS_{2\mathrm{x}})d^\dagger_{\mathbf{k}+\mathbf{Q}_m,a\sigma}d_{\mathbf{k}a\bar{\sigma}}+(S_{1\mathrm{x}}+iS_{2\mathrm{x}})d^\dagger_{\mathbf{k}-\mathbf{Q}_m,a\sigma}d_{\mathbf{k}a\bar{\sigma}}\Big].$$

The third term gives

$$(U+J(\gamma-2))\Big[X_1\cos\mathbf{Q}_m\cdot\mathbf{R}_i+X_2\sin\mathbf{Q}_m\cdot\mathbf{R}_i\Big]d^\dagger_{ia\sigma}d_{i\bar{a}\bar{\sigma}}= \\ =\frac{1}{2}(U+J(\gamma-2))\Big[(X_1-iX_2)d^\dagger_{\mathbf{k}+\mathbf{Q}_m,a\sigma}d_{\mathbf{k}\bar{a}\bar{\sigma}}+(X_1+iX_2)d^\dagger_{\mathbf{k}-\mathbf{Q}_m,a\sigma}d_{\mathbf{k}\bar{a}\bar{\sigma}}\Big].$$

Finally, the last term gives

$$\Big\{(J(4+\gamma)-U)\Big[O_1+O_2e^{i\mathbf{Q}_c\cdot\mathbf{R}_i}\Big]-\sigma\Big[U+J(\gamma-2)\Big]\Big[Z_1+Z_2e^{i\mathbf{Q}_c\cdot\mathbf{R}_i}+ \\ +Z_3\cos\mathbf{Q}_m\cdot\mathbf{R}_i+Z_4\sin\mathbf{Q}_m\cdot\mathbf{R}_i\Big]\Big\}d^\dagger_{ia\sigma}d_{i\bar{a}\bar{\sigma}}= \\ =\Big[(J(4+\gamma)-U)O_1-\sigma(U+J(\gamma-2))Z_1\Big]d^\dagger_{\mathbf{k},a\sigma}d_{\mathbf{k}\bar{a}\sigma}+\Big[(J(4+\gamma)-U)O_2- \\ -\sigma(U+J(\gamma-2))Z_2\Big]d^\dagger_{\mathbf{k}+\mathbf{Q}_c,a\sigma}d_{\mathbf{k}\bar{a}\sigma}-\sigma(U+J(\gamma-2))\Big[(Z_3-iZ_4)d^\dagger_{\mathbf{k}+\mathbf{Q}_m,a\sigma}d_{\mathbf{k}\bar{a}\sigma}+ \\ +(Z_3+iZ_4)d^\dagger_{\mathbf{k}-\mathbf{Q}_m,a\sigma}d_{\mathbf{k}\bar{a}\sigma}\Big].$$

Define some abbreviated interaction strengths

$$\bar{U}=\frac{3U-5J}{4},\quad U_0=\frac{U+J}{2},\quad U_1=\frac{U+J(\gamma-2)}{2},\quad U_2=J(4+\gamma)-U. \tag{D.4}$$

Also define

$$\Sigma_z = S_{1\mathrm{z}} + iS_{2\mathrm{z}}, \quad \Sigma_x = S_{1\mathrm{x}} + iS_{2\mathrm{x}}, \quad \chi = X_1 + iX_2, \quad \zeta = Z_3 + iZ_4. \tag{D.5}$$

Using these, we can write down the expressions for the various 4×4 subblocks of the 16×16 matrices $h(\mathbf{k})$ that we diagonalize at every $\mathbf{k}$. Recall that the matrices $h(\mathbf{k})$ are written

$$\hat{H}_{\mathrm{HF}} = \sum_{\mathbf{k}} \psi^\dagger_{\mathbf{k}} h(\mathbf{k}) \psi_{\mathbf{k}},$$

where

$$\psi^\dagger_{\mathbf{k}} = (\psi^\dagger_{\mathbf{k}z\uparrow}, \psi^\dagger_{\mathbf{k}\bar{z}\uparrow}, \psi^\dagger_{\mathbf{k}z\downarrow}, \psi^\dagger_{\mathbf{k}\bar{z}\downarrow})$$

and

$$\psi^\dagger_{\mathbf{k}a\sigma} = (d^\dagger_{\mathbf{k}a\sigma}, d^\dagger_{\mathbf{k}+\mathbf{Q}_m,a\sigma}, d^\dagger_{\mathbf{k}+\mathbf{Q}_c,a\sigma}, d^\dagger_{\mathbf{k}-\mathbf{Q}_m,a\sigma}).$$

The matrices for the same orbital, same spin subblock have the form

$$\hat{h}_{a\sigma,a\sigma} = \begin{pmatrix} \bar{U}-\sigma U_0 S_{\mathrm{FM}}+ \\ +t_{aa}(\mathbf{k}) & -\frac{\sigma U_0}{2}\Sigma_z & \bar{U}\delta-2\epsilon_b u- \\ & & -\sigma U_0 S_{\mathrm{AFM}} & -\frac{\sigma U_0}{2}\Sigma_z^* \\ -\frac{\sigma U_0}{2}\Sigma_z^* & \bar{U}-\sigma U_0 S_{\mathrm{FM}}+ \\ & +t_{aa}(\mathbf{k}+\mathbf{Q}_m) & -\frac{\sigma U_0}{2}\Sigma_z & \bar{U}\delta-2\epsilon_b u- \\ & & & -\sigma U_0 S_{\mathrm{AFM}} \\ \bar{U}\delta-2\epsilon_b u- \\ -\sigma U_0 S_{\mathrm{AFM}} & -\frac{\sigma U_0}{2}\Sigma_z^* & \bar{U}-\sigma U_0 S_{\mathrm{FM}}+ \\ & & +t_{aa}(\mathbf{k}+\mathbf{Q}_c) & -\frac{\sigma U_0}{2}\Sigma_z \\ -\frac{\sigma U_0}{2}\Sigma_z & \bar{U}\delta-2\epsilon_b u- \\ & -\sigma U_0 S_{\mathrm{AFM}} & -\frac{\sigma U_0}{2}\Sigma_z^* & \bar{U}-\sigma U_0 S_{\mathrm{FM}}+ \\ & & & t_{aa}(\mathbf{k}-\mathbf{Q}_m) \end{pmatrix}. \tag{D.6}$$

The matrices for the same orbital, opposite spin subblocks are

$$\hat{h}_{a\sigma,a\bar{\sigma}} = \begin{pmatrix} & -\frac{U_0}{2}\Sigma_x & & -\frac{U_0}{2}\Sigma_x^* \\ -\frac{U_0}{2}\Sigma_x^* & & -\frac{U_0}{2}\Sigma_x & \\ & -\frac{U_0}{2}\Sigma_x^* & & -\frac{U_0}{2}\Sigma_x \\ -\frac{U_0}{2}\Sigma_x & & -\frac{U_0}{2}\Sigma_x^* & \end{pmatrix}. \tag{D.7}$$

The matrices for the opposite orbital, opposite spin are

$$\hat{h}_{a\sigma,\bar{a}\bar{\sigma}} = \begin{pmatrix} & -U_1\chi & & -U_1\chi^* \\ -U_1\chi^* & & -U_1\chi & \\ & -U_1\chi^* & & -U_1\chi \\ -U_1\chi & & -U_1\chi^* & \end{pmatrix}. \tag{D.8}$$

Finally, the opposite orbital, same spin matrices have the form

$$\hat{h}_{a\sigma,\bar{a}\sigma} = \begin{pmatrix} \substack{U_2O_1-2\sigma U_1Z_1+\\+t_{a\bar{a}}(\mathbf{k})} & -\sigma U_1\zeta & \substack{U_2O_2-\\-2\sigma U_1Z_2} & -\sigma U_1\zeta^* \\ -\sigma U_1\zeta^* & \substack{U_2O_1-2\sigma U_1Z_1+\\+t_{a\bar{a}}(\mathbf{k}+\mathbf{Q}_m)} & -\sigma U_1\zeta & \substack{U_2O_2-\\-2\sigma U_1Z_2} \\ \substack{U_2O_2-\\-2\sigma U_1Z_2} & -\sigma U_1\zeta^* & \substack{U_2O_1-2\sigma U_1Z_1+\\+t_{a\bar{a}}(\mathbf{k}+\mathbf{Q}_c)} & -\sigma U_1\zeta \\ -\sigma U_1\zeta & \substack{U_2O_2-\\-2\sigma U_1Z_2} & -\sigma U_1\zeta^* & \substack{U_2O_1-2\sigma U_1Z_1+\\+t_{a\bar{a}}(\mathbf{k}-\mathbf{Q}_m)} \end{pmatrix}. \tag{D.9}$$

Appendix E

Re-calculating the Hartree-Fock order parameters

In this appendix we demonstrate how to close the self-consistency loop when solving the Hartree-Fock equations, by recalculating the order parameters $\delta, S_{\mathrm{FM}}, ...$ for which the initial values were simply guessed. The order parameters are defined by the expressions

$$\begin{aligned}
\langle d^\dagger_{ia\sigma} d^\dagger_{ia\sigma}\rangle =& \frac{1}{4}\left[1+\delta e^{i\mathbf{Q}_c\cdot\mathbf{R}_i}\right] + \frac{\sigma}{2}\Big[S_{\mathrm{FM}} + S_{\mathrm{AFM}} e^{i\mathbf{Q}_c\cdot\mathbf{R}_i} + \\
&+ S_{1\mathrm{z}}\cos(\mathbf{Q}_m\cdot\mathbf{R}_i) + S_{2\mathrm{z}}\sin(\mathbf{Q}_m\cdot\mathbf{R}_i)\Big], \\
\langle d^\dagger_{ia\sigma} d^\dagger_{i\bar{a}\bar{\sigma}}\rangle =& \frac{1}{2}\left[S_{1\mathrm{x}}\cos(\mathbf{Q}_m\cdot\mathbf{R}_i) + S_{2\mathrm{x}}\sin(\mathbf{Q}_m\cdot\mathbf{R}_i)\right], \\
\langle d^\dagger_{ia\sigma} d^\dagger_{i\bar{a}\sigma}\rangle =& O_1 + O_2 e^{i\mathbf{Q}_c\cdot\mathbf{R}_i} + \sigma\Big[Z_1 + Z_2 e^{i\mathbf{Q}_c\cdot\mathbf{R}_i} + \\
&+ Z_3\cos(\mathbf{Q}_m\cdot\mathbf{R}_i) + Z_4\sin(\mathbf{Q}_m\cdot\mathbf{R}_i)\Big], \\
\langle d^\dagger_{ia\sigma} d^\dagger_{i\bar{a}\bar{\sigma}}\rangle =& X_1\cos(\mathbf{Q}_m\cdot\mathbf{R}_i) + X_2\sin(\mathbf{Q}_m\cdot\mathbf{R}_i).
\end{aligned} \tag{E.1}$$

When we diagonalize the Hamiltonian $\hat{H}_{\mathrm{HF}}$ from Appendix D, we are left with the 16-tuple momentum space eigenvectors arranged like

$$\psi^\dagger_{\mathbf{k}} = (\psi^\dagger_{\mathbf{k}z\uparrow}, \psi^\dagger_{\mathbf{k}\bar{z}\uparrow}, \psi^\dagger_{\mathbf{k}z\downarrow}, \psi^\dagger_{\mathbf{k}\bar{z}\downarrow})$$

with

$$\psi^\dagger_{\mathbf{k}a\sigma} = (d^\dagger_{\mathbf{k}a\sigma}, d^\dagger_{\mathbf{k}+\mathbf{Q}_m,a\sigma}, d^\dagger_{\mathbf{k}+\mathbf{Q}_c,a\sigma}, d^\dagger_{\mathbf{k}-\mathbf{Q}_m,a\sigma}).$$

As is discussed in the main text in Chapter 3, the density matrix,

$$\rho(\zeta b\tau, \eta a\sigma) = \sum_{\mathbf{k}} \langle\Psi_e|\, d^\dagger_{\mathbf{k}+\eta\mathbf{Q}_m,a\sigma} d_{\mathbf{k}+\zeta\mathbf{Q}_m,b\tau}\,|\Psi_e\rangle\,, \tag{E.2}$$

is essentially the quantity we need to calculate, and it turns out that it can be obtained from the occupied eigenvectors $|\mathbf{k}, n\rangle$ (n runs from 1 to 16, as there are 16 eigenvectors for each 16×16 subblock) by

$$\rho(\zeta b\tau, \eta a\sigma) = \sum_{\mathbf{k}}{}' |\mathbf{k}, n\rangle \langle \mathbf{k}, n| , \tag{E.3}$$

where the prime on the sum indicates that the summation is over only the occupied eigenvectors (which are determined by ranking all the eigenvectors in accordance with their corresponding eigenvalues, then taking the lower quarter). Thus the crucial task is to connect the real-space matrix elements in E.1 with the momentum space density matrix $\rho(\zeta b\tau, \eta a\sigma)$. To do this, we use Fourier's trick: this is the same trick we used when Fourier transforming the Hamiltonian in Appendix D. The trick is that any sum of the form $\sum_i e^{i\mathbf{s}\cdot\mathbf{R}_i}(...)$ is zero unless $\mathbf{s} \cdot \mathbf{R}_i = 0 \bmod 2\pi$: essentially the sign of the summands keeps alternating and they effectively average out. We can use this to invert the expressions in Eqs: E.1 for the various order parameters $\delta, O_1, ...$ by multiplying by the inverse of the exponential factor of the parameter we want so as to cancel it out: the rest of the terms in that expression will then sum to zero because of Fourier's trick and we can isolate the one we are interested in. This was already demonstrated in the text for S_{FM} and for δ: we quote the expressions here for completeness

$$\delta = \frac{1}{N}\sum_{\mathbf{k}a\sigma}\langle d^\dagger_{\mathbf{k}+\mathbf{Q}_c,a\sigma} d_{\mathbf{k}a\sigma}\rangle = \sum_{a\sigma}\Big[\rho(0a\sigma, 2a\sigma) + \rho(1a\sigma, -1a\sigma) + \\ + \rho(2a\sigma, 0a\sigma) + \rho(-1a\sigma, 1a\sigma)\Big]. \tag{E.4}$$

$$S_{\mathrm{FM}} = \frac{1}{2N}\sum_{\mathbf{k}a\sigma}\sigma\langle d^\dagger_{\mathbf{k}a\sigma} d_{\mathbf{k}a\sigma}\rangle = \frac{1}{2N}\sum_{\eta a\sigma}\sigma\rho(\eta a\sigma, \eta a\sigma). \tag{E.5}$$

We obtain the rest of the by analogy. The expressions for many are essentially immediate

$$S_{\mathrm{AFM}} = \frac{1}{2N}\sum_{\mathbf{k}a\sigma}\sigma\langle d^\dagger_{\mathbf{k}+\mathbf{Q}_c,a\sigma} d_{\mathbf{k}a\sigma}\rangle = \\ = \sum_{a\sigma}\sigma\Big[\rho(0a\sigma, 2a\sigma) + \rho(1a\sigma, -1a\sigma) + \rho(2a\sigma, 0a\sigma) + \rho(-1a\sigma, 1a\sigma)\Big], \tag{E.6}$$

$$O_1 = \frac{1}{4N}\sum_{\mathbf{k}a\sigma}\langle d^\dagger_{\mathbf{k}a\sigma} d_{\mathbf{k}a\sigma}\rangle = \frac{1}{4N}\sum_{\eta a\sigma}\rho(\eta a\sigma, \eta\bar{a}\sigma), \tag{E.7}$$

$$Z_1 = \frac{1}{4N}\sum_{\mathbf{k}a\sigma}\sigma\langle d^\dagger_{\mathbf{k}a\sigma} d_{\mathbf{k}a\sigma}\rangle = \frac{1}{4N}\sum_{\eta a\sigma}\sigma\rho(\eta a\sigma, \eta\bar{a}\sigma), \tag{E.8}$$

$$\begin{aligned} O_2 &= \frac{1}{4N}\sum_{\mathbf{k}a\sigma}\sigma\langle d^\dagger_{\mathbf{k}+\mathbf{Q}_c,a\sigma} d_{\mathbf{k}a\sigma}\rangle = \\ &= \sum_{a\sigma}\sigma\Big[\rho(0a\sigma, 2a\sigma) + \rho(1a\sigma, -1a\sigma) + \rho(2a\sigma, 0a\sigma) + \rho(-1a\sigma, 1a\sigma)\Big]. \end{aligned} \tag{E.9}$$

The other parameters require just a little more finesse. Looking to the second line in eqs. E.1, re-express the trigonometric functions in terms of the exponentials

$$\langle d^\dagger_{ia\sigma} d^\dagger_{ia\bar{\sigma}}\rangle = \frac{1}{4}\left[(S_{1\mathrm{x}} - iS_{2\mathrm{x}})\, e^{i\mathbf{Q}_m\cdot\mathbf{R}_i} + (S_{1\mathrm{x}} + iS_{2\mathrm{x}})\, e^{-i\mathbf{Q}_m\cdot\mathbf{R}_i}\right]. \tag{E.10}$$

Multiplying by the two exponentials and carrying out the sum produces the expressions

$$\sum_{ia\sigma} e^{-i\mathbf{Q}_m\cdot\mathbf{R}_i}\langle d^\dagger_{ia\sigma} d^\dagger_{ia\bar{\sigma}}\rangle = S_{1\mathrm{x}} - iS_{2\mathrm{x}}, \quad \sum_{ia\sigma} e^{i\mathbf{Q}_m\cdot\mathbf{R}_i}\langle d^\dagger_{ia\sigma} d^\dagger_{ia\bar{\sigma}}\rangle = S_{1\mathrm{x}} + iS_{2\mathrm{x}}. \tag{E.11}$$

Adding or subtracting these and carrying out the Fourier transform gives the expressions for $S_{1/2\mathrm{x}}$

$$\begin{aligned} S_{1\mathrm{x}} &= \frac{1}{2N}\sum_{\mathbf{k}a\sigma}\Big[\langle d^\dagger_{\mathbf{k}+\mathbf{Q}_m,a\sigma} d_{\mathbf{k}a\sigma}\rangle + \langle d^\dagger_{\mathbf{k}-\mathbf{Q}_m,a\sigma} d_{\mathbf{k}a\sigma}\rangle\Big] = \\ &= \frac{1}{2N}\sum_{a\sigma}\Big[\Big(\rho(0a\sigma, 1a\bar{\sigma}) + \rho(1a\sigma, 2a\bar{\sigma}) + \rho(2a\sigma, -1a\bar{\sigma}) + \rho(-1a\sigma, 0a\bar{\sigma})\Big) + \\ &+ \Big(\rho(1a\sigma, 0a\bar{\sigma}) + \rho(2a\sigma, 1a\bar{\sigma}) + \rho(-1a\sigma, 2a\bar{\sigma}) + \rho(0a\sigma, -1a\bar{\sigma})\Big)\Big]. \end{aligned} \tag{E.12}$$

$$\begin{aligned} S_{2\mathrm{x}} &= \frac{1}{2iN}\sum_{\mathbf{k}a\sigma}\Big[\langle d^\dagger_{\mathbf{k}+\mathbf{Q}_m,a\sigma} d_{\mathbf{k}a\sigma}\rangle - \langle d^\dagger_{\mathbf{k}-\mathbf{Q}_m,a\sigma} d_{\mathbf{k}a\sigma}\rangle\Big] = \\ &= \frac{1}{2iN}\sum_{a\sigma}\Big[\Big(\rho(0a\sigma, 1a\bar{\sigma}) + \rho(1a\sigma, 2a\bar{\sigma}) + \rho(2a\sigma, -1a\bar{\sigma}) + \rho(-1a\sigma, 0a\bar{\sigma})\Big) - \\ &- \Big(\rho(1a\sigma, 0a\bar{\sigma}) + \rho(2a\sigma, 1a\bar{\sigma}) + \rho(-1a\sigma, 2a\bar{\sigma}) + \rho(0a\sigma, -1a\bar{\sigma})\Big)\Big]. \end{aligned} \tag{E.13}$$

By analogy with these we can immediately write down the rest of the expressions, as the only ones remaining also only depend on the trigonometric functions

$$S_{1z} = \frac{1}{2N}\sum_{\mathbf{k}a\sigma}\sigma\Big[\langle d^\dagger_{\mathbf{k}+\mathbf{Q}_m,a\sigma}d_{\mathbf{k}a\sigma}\rangle + \langle d^\dagger_{\mathbf{k}-\mathbf{Q}_m,a\sigma}d_{\mathbf{k}a\sigma}\rangle\Big] = \tag{E.14}$$

$$= \frac{1}{2N}\sum_{a\sigma}\sigma\Big[\Big(\rho(0a\sigma,1a\sigma)+\rho(1a\sigma,2a\sigma)+\rho(2a\sigma,-1a\sigma)+\rho(-1a\sigma,0a\sigma)\Big)+ \tag{E.15}$$

$$+\Big(\rho(1a\sigma,0a\sigma)+\rho(2a\sigma,1a\sigma)+\rho(-1a\sigma,2a\sigma)+\rho(0a\sigma,-1a\sigma)\Big)\Big]. \tag{E.16}$$

$$S_{2z} = \frac{1}{2iN}\sum_{\mathbf{k}a\sigma}\sigma\Big[\langle d^\dagger_{\mathbf{k}+\mathbf{Q}_m,a\sigma}d_{\mathbf{k}a\sigma}\rangle - \langle d^\dagger_{\mathbf{k}-\mathbf{Q}_m,a\sigma}d_{\mathbf{k}a\sigma}\rangle\Big] =$$

$$= \frac{1}{2iN}\sum_{a\sigma}\sigma\Big[\Big(\rho(0a\sigma,1a\sigma)+\rho(1a\sigma,2a\sigma)+\rho(2a\sigma,-1a\sigma)+\rho(-1a\sigma,0a\sigma)\Big)$$

$$-\Big(\rho(1a\sigma,0a\sigma)+\rho(2a\sigma,1a\sigma)+\rho(-1a\sigma,2a\sigma)+\rho(0a\sigma,-1a\sigma)\Big)\Big]. \tag{E.17}$$

$$Z_3 = \frac{1}{4N}\sum_{\mathbf{k}a\sigma}\sigma\Big[\langle d^\dagger_{\mathbf{k}+\mathbf{Q}_m,a\sigma}d_{\mathbf{k}\bar{a}\sigma}\rangle + \langle d^\dagger_{\mathbf{k}-\mathbf{Q}_m,a\sigma}d_{\mathbf{k}\bar{a}\sigma}\rangle\Big] =$$

$$= \frac{1}{4N}\sum_{a\sigma}\sigma\Big[\Big(\rho(0a\sigma,1\bar{a}\sigma)+\rho(1a\sigma,2\bar{a}\sigma)+\rho(2a\sigma,-1\bar{a}\sigma)+\rho(-1a\sigma,0\bar{a}\sigma)\Big)+$$

$$+\Big(\rho(1a\sigma,0\bar{a}\sigma)+\rho(2a\sigma,1\bar{a}\sigma)+\rho(-1a\sigma,2\bar{a}\sigma)+\rho(0a\sigma,-1\bar{a}\sigma)\Big)\Big]. \tag{E.18}$$

$$Z_4 = \frac{1}{4iN}\sum_{\mathbf{k}a\sigma}\sigma\Big[\langle d^\dagger_{\mathbf{k}+\mathbf{Q}_m,a\sigma}d_{\mathbf{k}\bar{a}\sigma}\rangle - \langle d^\dagger_{\mathbf{k}-\mathbf{Q}_m,a\sigma}d_{\mathbf{k}\bar{a}\sigma}\rangle\Big] =$$

$$= \frac{1}{4iN}\sum_{a\sigma}\sigma\Big[\Big(\rho(0a\sigma,1\bar{a}\sigma)+\rho(1a\sigma,2\bar{a}\sigma)+\rho(2a\sigma,-1\bar{a}\sigma)+\rho(-1a\sigma,0\bar{a}\sigma)\Big)$$

$$-\Big(\rho(1a\sigma,0\bar{a}\sigma)+\rho(2a\sigma,1\bar{a}\sigma)+\rho(-1a\sigma,2\bar{a}\sigma)+\rho(0a\sigma,-1\bar{a}\sigma)\Big)\Big]. \tag{E.19}$$

Finally,

$$X_1 = \frac{1}{4N}\sum_{\mathbf{k}a\sigma}\sigma\Big[\langle d^\dagger_{\mathbf{k}+\mathbf{Q}_m,a\sigma}d_{\mathbf{k}\bar{a}\bar{\sigma}}\rangle + \langle d^\dagger_{\mathbf{k}-\mathbf{Q}_m,a\sigma}d_{\mathbf{k}\bar{a}\bar{\sigma}}\rangle\Big] =$$

$$= \frac{1}{4N}\sum_{a\sigma}\sigma\Big[\Big(\rho(0a\sigma,1\bar{a}\bar{\sigma})+\rho(1a\sigma,2\bar{a}\bar{\sigma})+\rho(2a\sigma,-1\bar{a}\bar{\sigma})+\rho(-1a\sigma,0\bar{a}\bar{\sigma})\Big)+$$

$$+\Big(\rho(1a\sigma,0\bar{a}\bar{\sigma})+\rho(2a\sigma,1\bar{a}\bar{\sigma})+\rho(-1a\sigma,2\bar{a}\bar{\sigma})+\rho(0a\sigma,-1\bar{a}\bar{\sigma})\Big)\Big]. \tag{E.20}$$

$$X_2 = \frac{1}{4iN}\sum_{\mathbf{k}a\sigma}\sigma\Big[\langle d^\dagger_{\mathbf{k}+\mathbf{Q}_m,a\sigma}d_{\mathbf{k}\bar{a}\bar{\sigma}}\rangle - \langle d^\dagger_{\mathbf{k}-\mathbf{Q}_m,a\sigma}d_{\mathbf{k}\bar{a}\bar{\sigma}}\rangle\Big] =$$
$$= \frac{1}{4iN}\sum_{a\sigma}\sigma\Big[\Big(\rho(0a\sigma,1\bar{a}\bar{\sigma}) + \rho(1a\sigma,2\bar{a}\bar{\sigma}) + \rho(2a\sigma,-1\bar{a}\bar{\sigma}) + \rho(-1a\sigma,0\bar{a}\bar{\sigma})\Big)$$
$$- \Big(\rho(1a\sigma,0\bar{a}\bar{\sigma}) + \rho(2a\sigma,1\bar{a}\bar{\sigma}) + \rho(-1a\sigma,2\bar{a}\bar{\sigma}) + \rho(0a\sigma,-1\bar{a}\bar{\sigma})\Big)\Big]. \qquad \text{(E.21)}$$